Rheo-mechanics and Foam Stability of 3D Printable Foamed Concrete with Nanoparticle Incorporation

by

Seung Cho

Dissertation presented for the degree of

Doctor of Philosophy in Engineering

in the Faculty of Engineering

at Stellenbosch University

Supervisor: Prof Gideon P.A.G van Zijl

Co-supervisor: Dr Algurnon S van Rooyen

March 2021

Declaration

By submitting this dissertation electronically, I declare that the entirety of the work contained therein is my own, original work, that I am the sole author thereof (save to the extent explicitly otherwise stated), that reproduction and publication thereof by Stellenbosch University will not infringe any third party rights and that I have not previously in its entirety or in part submitted it for obtaining any qualification.

This dissertation includes 1 original paper published in peer-reviewed journal or book and 3 unpublished publications. The development and writing of the papers (published and unpublished) were the principal responsibility of myself and, for each of the cases where this is not the case, a declaration is included in the dissertation indicating the nature and extent of the contributions of co-authors.

February 2021

Abstract

The imaginative concept of digital construction (DC), through the 3D concrete printing (3DCP) technique, is emerging, driven by the ceaseless efforts of academia and the dynamic collaboration with pioneering start-up companies. The endeavours towards automation in construction are accelerated by the great demand for construction time- and cost-savings in economic and sustainability aspects, as well as acquiring design flexibility.

The most renowned lightweight building material, namely lightweight foamed concrete (LWFC) – consists of a concrete paste that is aerated with a natural protein-based foaming agent, is considered as energy-efficient due to its native prominent thermal and acoustic insulative properties, and reduced embodied energy of a concrete structure due to the reduced solid content and low weight. The evolution of LWFC began 50 years ago, and many applications of LWFC were developed for the building and construction (B&C) industry. From the overarching benefits of 3DCP and LWFC, the harmonisation of those techniques is expected to bring promising outcomes for the B&C industry.

In this research, the mix design development of LWFC for 3D printing application (3DP-LWFC) through rheological modification without compromising foam stability is presented and investigated through various theoretical discussions and experimental programmes.

As a preliminary work, normal weight 3D printable concrete mix design was developed, and rheological and mechanical properties were characterised. As a validation for the printability – a term expressing suitable pumpability, buildability and shape retention – several objects were constructed with the designed material and 3D printing technique.

Rheological modification of LWFC raises concern for foam stability, since foam stability received significant attention in literature on conventional LWFC which is highly flowable, and has low shearing yield stress in the order of tens of Pascals. The effect of fresh stiffness of the base mix on foam stability is initially investigated here, and an optimal slump flow range, 185 mm – 195 mm, acquired by considering both foam stability and buildability. Based on the optimal base mix, three different LWFC mixes were designed for 3D printing application, namely 700, 1000 and 1400 kg/m^3 denoted as TD-7, TD-10 and TD-14. Foam stability tests with the designed samples were conducted under static and dynamic environments. In particular, the identical 3D printer and concrete pump setup were used to investigate the actual foam stability behaviour of 3DP-LWFC. In a static environment, no foam destabilisation was observed for all samples. The post-pumped TD-10 sample showed slight densification after 3 minutes of continuous 3D printing extrusion, whereas TD-14 showed a higher degree of densification immediately. The TD-7 sample showed the most stable behaviour for both pre- and post-pumped samples, i.e. no densification was found. Void structures of three samples were

investigated through X-ray computed tomography scan images, and a directly proportional relation between porosity (19.94% - 52.77% depending on the density of the sample) and foam volume fraction confirmed. The analysis also showed that pumping pressure, in most cases, created confining pressure which led to reduced void sphericity and increased smaller sized pore populations.

Rheological characterisation is presented for the same LWFC density range, from tests performed with a rotary concrete rheometer. Two types of tests, i.e. a controlled shear-rate (CSR) test and a flow curve test, were performed to identify yield stress, thixotropic parameters (R_{thix} and A_{thix}), elastic shear modulus, plastic and kinematic viscosity. A direct proportional relation is found between density and yield stress, thixotropic behaviour and shear modulus. With the rheological characteristics, buildability was investigated for the three densities. As result, 17 printed layers were constructed with TD-14 in continuous high-rate 3DPC before plastic collapse. A potential practical 3DP-LWFC application is demonstrated by constructing modular buoyant façade elements, i.e. with density less than 1000 kg/m^3.

Finally, the effect of nanoparticle inclusion in LWFC for both rheological and mechanical behaviour is studied. The yield stress of nanoparticle infused LWFC is increased by roughly two orders up to 1170 Pa, compared to conventional LWFC. Nanoparticle inclusion also introduced significant improvement in mechanical strength – compressive strength 31.1 MPa, flexural strength 3.8 MPa and elastic modulus 13.8 GPa at 28 days– compared to the conventional LWFC – compressive strength 11.6 MPa, flexural strength 1.4 MPa and elastic modulus 7.1 GPa at 28 days.

This research unlocks structural and innovative application of LWFC, and introduces the engineered material to the B&C industry so that they can bring innovative ideas and new thinking regarding structural and architectural design.

Opsomming

Die verbeeldingryke konsep van digitale konstruksie (DC), ook bekend as 3DCP-tegniek (3D concrete printing), ontluik deur intensiewe navorsing in die akademie in samewerking met baanbreker pioniersmaatskappye. Die pogings tot outomatisering in konstruksie word versnel deur die groot vraag na konstruksietyd- en kostebesparings in ekonomiese en volhoubaarheidsaspekte, sowel as buigsaamheid in ontwerp.

Die mees bekende liggewig boumateriaal, naamlik skuimbeton, word as energie-effektief beskou, weens inherente termiese en akoestiese isolerende eienskappe, en laer ingeslote energie van 'n betonstruktuur as gevolg van die lae gewig. Die ontwikkeling van LWFC het 50 jaar gelede begin, en baie toepassings van LWFC is ontwikkel vir die bou- en konstruksiebedryf (B&C). Van die oorkoepelende voordele van 3DCP en LWFC, word verwag dat die harmonisering van hierdie tegnieke 'n belowende uitkoms vir die B&C-industrie sal lewer.

In hierdie navorsing word die ontwikkeling van die mengontwerp van LWFC vir 3D-drukwerk deur reologiese aanpassing sonder om skuimstabiliteit in te boet, aangebied en ondersoek deur middel van verskillende teoretiese beskouings en eksperimentele programme.

As 'n voorwerk is die ontwerp van die normale 3D-drukbare mengontwerp ontwikkel en is reologiese en meganiese eienskappe gekarakteriseer. Om die 3D-drukbaarheid te bevestig - bestaande uit pompbaarheid, boubaarheid en vormbehoud - is verskeie voorwerpe met die ontwerpte materiaal en 3D-druktegnieke vervaardig.

Reologiese aanpassings van LWFC wek sorg oor skuimstabiliteit, aangesien bestaande literatuur skuimstabiliteit bestudeer vir konvensionele LWFC wat baie vloeiend is, en oor lae vloeispanning in die orde van tien talle Pascal beskik. Die effek van die styfheid van die basismengsel in die vars toestand op skuimstabiliteit word aanvanklik ondersoek, en die optimale spreidingsbereik, 185 mm - 195 mm, is verkry deur beide skuimstabiliteit en boubaarheid in ag te neem. Op grond van die optimale basismengsel is drie verskillende LWFC-menge ontwerp vir 3D-drukwerk, naamlik 700, 1000 en 1400 kg/m^3 of TD-7, TD-10 en TD-14. Skuimstabiliteitstoetse op monsters van die ontwerpte menge is onder 'n statiese en dinamiese toestand uitgevoer. In die besonder is die identiese 3D-drukker en betonpompopstelling gebruik om die ware skuimstabiliteitsgedrag van 3DP-LWFC te ondersoek. In 'n statiese toestand is geen skuimdestabilisering vir enige van die menge waargeneem nie. Die ná-gepompte TD-10-meng vertoon effense verdigting na 3 minute aaneenlopende ekstrusie, terwyl TD-14 onmiddellik 'n mate van verdigting ondergaan. TD-7 het die mees stabiele gedrag getoon beide voordat en nadat dit gepomp is, dit wil sê geen verdigting is gevind nie. Die porie-struktuur van drie monsters is ondersoek deur middel van X-straal tomografiese beelde, en ‘n direk eweredige verband is bevind

tussen porositeit (19,94% - 52,77%, afhangende van die digtheid van die monster) en die skuimvolume fraksie. Die ontleding het ook getoon dat pompdruk in die meeste gevalle inperkingsdruk skep wat lei tot laer bolvormigheid en 'n toename in die aantal kleiner porieë.

Reologiese karakterisering is gedoen vir dieselfde toetsreeks, met ‘n roterende beton-reometer. Twee soorte toetse is uitgevoer, naamlik ‘n beheerde skuiftempotoets (CSR) en ‘n vloeikurwe-toets, om vloeispanning, tiksotropiese parameters (R_{thix} en A_{thix}), elastiese skuifmodulus, sowel as plastiese en kinematiese viskositeit te identifiseer. ‘n Direkte proporsionele verband is gevind tussen digtheid en vloeispanning, tiksotropiese gedrag en skuifmodulus. Met hierdie reologiese eienskappe is boubaarheid van die drie digthede ondersoek. Gevolglik is 17 gedrukte lae met TD-14 behaal. 'n Moontlike praktiese toepassing is gedemonstreer deur die konstruksie van modulêre geuwelelemente met digtheid minder as 1000 kg/m^3.

Laastens is die effek van insluiting van nanopartikels in LWFC op sowel reologiese as meganiese gedrag bestudeer. Die vloeispanning van LWFC word met rofweg twee ordes verhoog deur nanopartikels tot ‘n statiese vloeispanning van 1170 Pa. Insluiting van nanopartikels bring ook beduidende verbetering in meganiese sterkte - druksterkte 31.1 MPa, buigsterkte 3.8 MPa en elastisiteitsmodulus 13.8 GPa op 28 dae - vergeleke met die konvensionele LWFC - druksterkte 11.6 MPa, buigsterkte 1.4 MPa en elastiese modulus 7.1 GPa op 28 dae.

Hierdie navorsing ontsluit strukturele en innoverende toepassing van LWFC en stel die ontwerpte materiaal aan die B&C-industrie bekend sodat hulle innoverende idees en nuwe denke rakende strukturele en argitektoniese ontwerp kan skep.

Acknowledgements

This completion of this research could not have been possible without the participation and supports of so many people whose names may not all be enumerated. Their supports, no matter the means – physical, mental, or financial, are sincerely appreciated and gratefully acknowledged. However, I particularly would like to express deep appreciation and indebtedness to the following:

My supervisor, **Professor Gideon van Zijl**, for his unending and forbearing support, mentorship, and encouragement throughout the entire research journey. His exceptional insights and fundamental knowledge about this concrete science field always inspired me and his ceaseless trust on me has made many breakthroughs. Many laughs and joys that we shared together made tough times enjoyable and it has certainly been *unforgettable journey with him*.

My co-supervisor, **Dr. Algurnon Tata van Rooyen**, for his specialised knowledge about foamed concrete. In the midst of many uncertainties about foamed concrete, he has willingly assisted me with his expertise knowledge and insights.

Dr. Jacques Kruger, a "captain" of 3DCP team, for his creative, logical and critical thinking and advice which has inspired many portions of my research. He has encouraged me many instances and particularly I thank him for being a good friend.

The 3DCP team, **Mr. Marchant van den Heever** and **Mr. Frederick Bester**, for their inspiration and great help on experimental programme design and work. Their practical experiences and discernment significantly help me a lot along experimental works.

The laboratory and workshop staffs of structure and concrete laboratory in Stellenbosch University for their assistance and guidance with experimental work.

My parents, **Ms. Seung-joo** and **Mr. Ho-jin Cho**, for showing your unconditional love and support throughout this research.

My wife and baby, **Ms. Daeun** and **Yui Cho**, for their ineffable love, patience and support with ceaseless encouragement. You two ladies make my life meaningful and enriched unequivocally.

My God for his steadfast and unconditional love and giving me strength throughout my life.

"Give thanks to the LORD, for he is good. His love endures forever." (Ps. 136:1)

Table of Contents

List of Figures

List of Tables

List of Abbreviations and Acronyms

3D	Three-dimensional
3DCP	Three-dimensional concrete printer/printing
3DP	Three-dimensional print(ed)
4IR	Industrial revolution 4.0
ACI	American Concrete Institute
AI	Artificial intelligence
AM	Additive manufacturing
ASTM	American Society for Testing and Materials
B&C	Building and Construction
BS	British Standard
CAD	Computer-aided design
CoV	Coefficient of variation
CSA	Calcium sulfoalmuninate
CSR	Controlled/Constant shear rate
DC	Digital construction
DLVO	Derjaguin-Landau-Verwey-Overbeek
DOF	Degree of freedom
EN	European Norms
FRC	Fibre reinforced concrete
HPC	High-performance concrete
I/O	Input/output
IBS	Interlayer bond strength
ICAR	International Centre for Aggregate Research
IoT	Internet of things
LL	Lubrication layer

LOF	Lack-of-fusion
LWFC	Lightweight foamed concrete
MCU	Microcontroller unit
MTM	Materials testing machine
PC	Portland cement
PLA	Polyactic acid
PP	Polypropylene
PSU	Power supply unit
RH	Relative humidity
SCM	Supplementary cementitious material
SU	Stellenbosch University
SP	Superplasticizer
SSA	Specific surface area
U-LWFC	Ultra-lightweight foamed concrete
VFD	Variable frequency drive
X-CT	X-ray computed tomography

List of Symobls

Roman

a	Fly ash
A_{thix}	Structuration rate
c	Cement mass
D	Rheometer vane diameter
dV	Change in volume
E	Elastic Young's modulus
F_{AR}	Strength correction factor
f_{cu}	Ultimate compressive strength
f_{flex}	Ultimate flexural strength
g	Gravitational acceleration
G	Shear modulus
H	Rheometer vane height
h	film thickness / filament layer height
k	water/cement ratio by weight
k_s	water/solids ratio by weight
l_p	Printing path length per layer
n	Porosity
nS	nano-silica powder
n_t	theoretical porosity
P	Pressure
P_c	Confinement pressure
P_p	Pumping pressure
P_σ	Laplace capillary pressure
r	radius of the rheometer vane

RD	Relative density
R_{thix}	Re-flocculation rate
s	Graded fine silica sand
S	Slump
sf	Silica fume
SiC	Silicon carbide
s_v	filler/cement ratio by weight
s_w	filler/cement ratio by volume
T	Rheometer torque
t	Time
t_{rf}	re-flocculation time
v	linear velocity / printing speed
V_f	Foam volume
w	Water content / Filament layer width
Z	Distance between the wall of the container and the vane radius

Greek

α_{geom}	Built shape-dependent geometric factor
γ	Shear strain
γ_c	Specific weight of cement
$\dot{\gamma}$	Shear strain rate
μ_p	Plastic viscosity
υ	Kinematic viscosity
Π_d	Disjoining pressure
Π_{el}	Electrostatic repulsive pressure
Π_{s-h}	Steric / hydration pressure
Π_{vw}	van der Waals attraction pressure
ρ	Density

ρ_{base}	Base mix density
ρ_{dry}	Oven dried density
ρ_{mature}	Air cured dry density
$\rho_{mature.pump}$	Post-pumped mature density
ρ_t	Target wet density
ρ_w	Density of water
ρ_{wet}	Wet density
$\rho_{wet.pump}$	Post-pumped wet density
τ_{dy}	Dynamic yield stress
$\tau_{dy.0}$	Initial dynamic yield stress
τ_{st}	Static yield stress
$\tau_{st.0}$	Initial static yield stress
ϕ	Diameter
ϕ_{foam}	Foam volume fraction
ω	Angular velocity

Chapter 1

Introduction

1.1 Background – Brief Overview

1.1.1 3D Concrete Printing (3DCP)

The computer was originally developed as an advanced tool to increase human computational efficiency. With continued development over time, the role of the computer in human life evolved to a symbiotic and closely interactive partnership – human-computer symbiosis, initially defined by Licklider (1960). Undoubtedly, more complex interactivity between mankind and computers is anticipated due to the endless desire for technical advancements, like Artificial Intelligence (AI) – implanting human intelligence, consciousness and emotionality to machine – and Internet of Things (IoT) – continuous connection and data exchange between the user and the hardware over the internet. This phenomenon has greatly impacted human cognition, perception, and intelligence, as well as societal culture and philosophy. (Grudin & Carroll, 2017). This symbiosis certainly implements more computer involvement to increase efficiency and quality significantly and it leads to labour intensity reduction.

Compared to other industries, building and construction (B&C) is considered a labour-intensive industry. Low labour productivity, defined as the output generated per person-hour, is reflected for the B&C (Weng *et al.*, 2020). Thus, automation as mitigation has certainly been in demand for B&C industries. Since the advent of semi to fully automated prefabricated element manufacturing for modular construction in the 1990s (Wakisaka *et al.*, 2000), there have been recent pioneering attempts to adopt additive manufacturing (AM) in B&C. Digital construction (DC) with concrete, in particular extrusion-based 3D Concrete Printing (3DCP), has seemingly drawn much attention in academia, the construction industry and even governments (Busta, 2016), given the increasing publication intensity, as well as demonstration and actual 3DPC buildings. Among various AM techniques investigated for construction, such as binder jetting and shotcrete 3D printing, extrusion-based layer deposition 3DCP is the most commonly reported type, which involves formwork free fabrication and freeform construction (Buswell *et al.*, 2020).

Formwork cost, including materials and labour, ranges between 35% and 54% of the overall cost of concrete structures, and consumes 50 – 75% of the overall time in conventional in-situ construction (Paul *et al.*, 2018). When it comes to a complex structure, the formwork must be custom-ordered or manufactured, which leads to a significant cost increase and lowered chance of re-use (de Soto *et al.*, 2018). No or limited re-use of formwork also implies significant environmental impact. Moreover, the

safety of the worker is not guaranteed since construction sites tend to be harsh environments even though there is strict control through standards and governmental bodies (Camacho *et al.*, 2018). In this light, formwork free 3DCP is deemed to reduce construction cost and time significantly, as well as providing a safer work environment as on-site labours are less.

Another principal benefit of 3DCP is the architectural design flexibility without causing an excessive cost. Unlike traditional construction, the complex geometry of structures can be easily tailored from computer-aided design (CAD) software and the object can be actualised by the concrete 3D printer. Since limitations in the 3DCP technique, e.g. overhang printing, can be complemented by cast-in-situ techniques, the synergy of 3DCP and cast-in-situ construction is expected to increase construction versatility.

Examples of dominantly used 3D printer classes are shown in Fig. 1.1. Gantry types typically are 3 axis translational systems with an additional degree of freedom (DOF) allowing nozzle axial rotation. However, nozzle head technology is available for gantry-type printers, offering up to 6 DOF to approach the more flexible motion and geometrical complexity offered by robotic arms type 3D printers.

(a)  (b) 

Fig. 1.1 3D concrete printer types (a) gantry (Wolfs *et al.*, 2018) and (b) robotic arms (Marchment *et al.*, 2020)

Irrespective of the 3D printer class, pumping and extrusion of concrete are the essential processes, hence *pumpability* and *buildability* lie at the core of 3DPC investigations. Concrete pumping is to transport the fresh material from the hopper to the nozzle. Positive-displacement piston pumps or progressive cavity pumps are typically used in 3DCP, with the latter the most common to date (Mechtcherine *et al.*, 2020). Pumpability is referred to as the ease of pumping the material through the pipe without causing material property change like pressurised bleeding (Tay *et al.*, 2019). The internal pressure of the material builds up due to the pumping pressure, and it causes shear-induced particle migration (SIPM), which forms a lubrication layer (LL) on the pipe wall. Depending on the thickness of the layer and the rheological property of the LL, in particular its plastic viscosity, the internal pressure of the material varies (Choi *et al.*, 2013). Since the rheology of the LL is inherited from the parental material, the rheological characterisation is crucial for pumpability characterisation.

The transported material is extruded through the nozzle onto the print bed along the pre-programmed print path. The pseudo-solid and elastoplastic cementitious material must retain the extruded shape

without plastic yielding under self-weight, defined as *shape retention*, since there is no formwork support. The subsequent layer is deposited onto the previously printed layer after the so-called pass time, defined as the time gap between printing successive layers. In the continuous layer deposition, the bottommost filament bears the total accumulative weight of the printed structure, but it must not exhibit local or global deformation by plastic yielding or structural failure, i.e. buckling. The material capacity to remain stable under the gravity loading of successive layers is defined as buildability. In general, the quality of the final 3D printed object, or *printability*, is ascribed to both pumpability and buildability.

For this particular application, the cementitious material must have low dynamic shear yield stress when agitated (de-flocculation process), for good pumpability, high static yield stress, and rapid early strength development, or re-building after extrusion (re-flocculation process), for sound shape retention and buildability. Those processes involve a complex physicochemical process at the microscopic level (Kruger *et al.*, 2019). Hence, the shear yield stress of the material and the shear history dependant rheological property, thixotropy, are key parameters for the design of 3D printable concrete material.

Once the structure is successfully printed, the hardened state mechanical performance becomes important for the structural purpose over the service life of the structure. Since a 3D printed object is not monolithic, the multidirectional orthotropic strength and stiffness moduli must be identified when characterising mechanical performance. Interlayer bond strength (IBS) is the paramount parameter dominating orthotropy, ductility and shear strength. At the layer deposition, the previous and successive layers are in contact to form interfacial adhesion. IBS is highly influenced by the pass time. In general, the interlayer region is weaker than the printed filament due to the smaller contact area, entrainment of air between layers, lack of surface water for a strong bond, and for large pass time the potential of a cold joint, coined as lack-of-fusion (LOF) (Kruger *et al.*, 2021). LOF formation creates weak interlayer planes which may be dominant failure planes and limit structural resistance despite high intra-layer material strength.

1.1.2 Lightweight Foamed Concrete (LWFC)

LWFC is a highly porous cementitious material made of mortar mix and precursor foam produced by a natural protein-based foam agent. Although the definition of LWFC density varies, the range 400 – 1600 kg/m^3 is generally accepted (van Rooyen, 2020), while the density of ultra-lightweight foamed concrete (U-LWFC) is below 400 kg/m^3 (Jones *et al.*, 2017). Several foamed concrete productions are available, e.g. chemical foaming, and natural or synthetic protein-based aqueous precursor foam insertions, but the latter foamed concrete production is the most common method (Feneuil *et al.*, 2019).

Due to the high void fraction of LWFC, it is thermally and acoustically insulative. For example, 980 kg/m^3 density LWFC has been reported to have a thermal conductivity of 0.24 W/mK, while 2100 kg/m^3 density normal concrete has a thermal conductivity of 1.68 W/mK (Markin *et al.*, 2019). The reduced weight of LWFC has a lower burden on the structure, and is beneficial aspect to seismic regions

due to low inertial loading. Also, the reasonable strength to weight ratio, or specific strength, of LWFC holds potential for structural application. The 28-day compressive strength of 1400 kg/m^3 density LWFC can be expected to be up to 20 MPa (Nambiar *et al.*, 2006). The elastic modulus of 8.0 GPa for 1500 kg/m^3 density LWFC (Jones *et al.*, 2005), however, indicates a lower stiffness to mass ratio for LWFC than normal-weight concrete, yet is comparable to other construction material like load-bearing masonry, for which 5 – 8 MPa compressive strength and 1800 kg/m^3 are typical (de Villiers 2019).

Furthermore, various researchers reported that Portland cement is largely replaced by supplementary cementitious material (SCM) in LWFC production for various purposes, such as long-term strength and durability improvement (Kearsley *et al.*, 2005). This allows reducing CO_2 emission from concrete containing Portland cement by employing sustainable building material ingredients.

The self-levelling nature, i.e. high workability, of conventional LWFC is considered to be an advantageous trait for traditional cast-in-situ construction. LWFC has a low shear yield strength, typically in the range of tens of Pascals (Ahmed *et al.*, 2009). However, this shear yield capacity is too low for 3DCP application and rheological modification is inevitable.

Foam stability is a crucial criterion for quality control purpose during the transition between fresh state and hardened state where the most active morphological change occurs (Feneuil *et al.*, 2019). Foam is generated from the diluted surface-active component, i.e. surfactant, solution through mechanical agitation and airflow. The surfactant lowers surface tension and encapsulates air with a viscous thin film in the form of a sphere that requires the least energy to sustain the shape, known as a bubble. Since all bubbles are thermodynamically unstable (Pugh, 1996), foam destabilises by itself and the surrounding environment through three mechanisms (See the graphic in Fig. 1.2): (1) *drainage* – film breakage by liquid flows through the thin films due to gravity, (2) *ripening* – two surrounding bubble merges or diffuses gas due to differential Laplace pressure, and (3) *coalescence* – film rupture due to physical and physicochemical process of the system, such as surface tension reduction promotes coalescence (Fameau *et al.*, 2014).

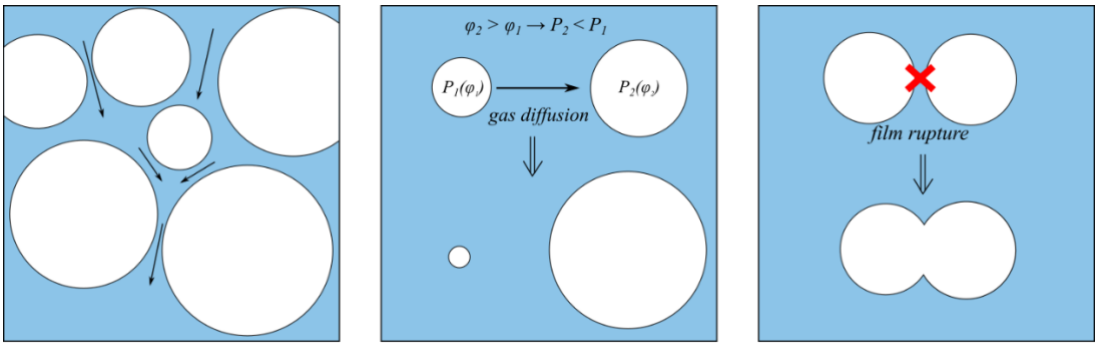

Fig. 1.2 Schematisation of foam destabilisation mechanisms

Foam stability in the two-phase system of air and liquid is primarily influenced by bubble morphology, which is affected by surfactant concentration and type, and the foam production process. Once the aqueous foam is incorporated and mixed thoroughly in the solid cement paste or mortar to form foamed concrete, the system becomes more complex by the interaction between bubbles and solid particles (Basařová *et al.*, 2019). Rheological, physical and physicochemical properties of solid paste control foam stability in LWFC. Densification is the prominent proof of unwanted foam instability, of which comprehensive details are presented in Chapter 3.

1.2 Problem Statement

The marriage of DC and LWFC potentially introduces various attractions in sustainability, economic, and societal aspects from each distinctive advantage discussed in Section 1.1. Reports on DC of LWFC are emerging in the literature, for instance, Markin et al. (2019) and Falliano et al. (2020) investigating 3DCP of LWFC. These studies are novel, and more in-depth research is required to adapt the material to the seemingly contrasting characteristics of high plastic yield stress and bubble stability.

The beneficial characteristic of conventional LWFC, its highly flowable, self-compacting and self-levelling nature, in conventional construction practices, turns into the most critical issue for digital fabrication application. As an essential benefit of 3D printing is formwork free construction, the 3D printable material must have sufficient shape retention and buildability, or stability under a load of upper layers. The low static and dynamic shear yield stress and less distinctive thixotropic behaviour of LWFC are suitable for casting application, but not for 3DPC. Hence, rheological improvement for 3D is required for sound shape retention and buildability.

Since 3DCP involves pumping and deposition actions, and subsequent bearing of self-weight and that of upper layers, excessive stress is introduced to the incorporated bubbles compared to the cast-in-situ application. These complex procedures may raise a concern on the foam stability of LWFC. Moreover, the higher confining stress to the individual bubble is concerned due to higher shear yield stress from rheology modification. Thus, foam stability must be improved and validated foremost with appropriate procedures.

Mechanical and microstructural characterisations of 3DP-LWFC are not readily available in the literature. Unlike the monolithic concrete structure, 3D printed concrete element has different orthotropic mechanical capacities depending on the testing direction. Thus, multi-directional mechanical performance must be studied. Moreover, it is postulated that the microstructural morphology may alter through pumping action. It is worthwhile to investigate the microstructure or pore structure of 3DP-LWFC.

Nanoparticle inclusion is considered to promote rheological, mechanical and microstructural performances through its high surface area to volume nature (Paul *et al.*, 2018). To counteract the

significantly low shear static yield capacity of LWFC, a nanoparticle was considered as an additive constituent. Calcium sulfoaluminate (CSA), containing high ye'elimite (C_4A_3S) content in sulfoaluminate belite and ferrialuminate clinkers (Mose *et al.*, 2016), attains early strength rapidly due to the excessive and rapid ettringite formation. It is postulated to escalate thixotropic behaviour of LWFC, so will printability, because of the rapid early strength evolvement. Jones et al. (2017) reported the partial replacement of Portland cement with CSA cement significantly improved foam stability in U-LWFC. This is further complementary merit for CSA usage in LWFC. Hence, compatibility and appropriate dosage identification of nanoparticle and CSA cement must be conducted.

1.3 Aim and Objectives

The main aim of the research is to **develop a 3D printable lightweight foam concrete (3DP-LWFC)**. The principal objectives to achieve the aim of this research are described as follows:

1. Material selection and mix design

Select and procure locally sourced dry and wet constituents appropriately, except for nanoparticle. Nanomaterials have been procured from the USA and Hong Kong, enabling nanoparticle incorporated LWFC to be developed in particular for the 3D printing process.

3DP-LWFC mix design is preliminarily rationed from conventional LWFC proposed by van Rooyen (2020) and subsequently adapted to attain appropriate shape retention and buildability for sound printability. The effect of nanoparticle and CSA cement inclusions, proposed by the author as remedies, are studied and appropriate dosages identified.

2. Foam stability assessment

Study the behaviour of foam in the solid paste and assess foam stability of 3DP-LWFC with a highly stiff cementitious material modified for DC. Study the theory to identify the main forces acting in bubble destabilisation mechanisms, and propose remedies. Subsequently, validate bubble stability in the modified LWFC with appropriate physical laboratory experimental methods. Actual pumping and extrusion through the nozzle involved in 3DP-LWFC must be included to verify foam stability.

3. Rheological characterisation assessment

A comprehensive study on rheological characterisation must be conducted, as it is the paramount factor for controlling pumpability and buildability. Quantification of the rheological parameters – static and dynamic shear yield stresses over time, re-flocculation rate (R_{thix}), structuration rate (A_{thix}), shear stiffness moduli, plastic and kinematic viscosity – must be performed in the laboratory environment.

4. Mechanical and microstructural characterisation assessment

Assess the mechanical behaviour of 3DP-LWFC in the hardened state through standardised and non-standardised laboratory-scale test methods. All directional orthotropic compressive strengths, elastic

moduli, flexural strength, and interlayer bond strength are considerable mechanical properties to be characterised.

In aspects of microstructural assessment, perform the void structure analysis through X-ray Computed Tomography (X-CT), a non-destructive evaluation technique, to generate 3D graphics utilised for void structure characterisation.

1.4 Scope and Limitation

The scope of the research is limited to the novel "self-standing" 3DP-LWFC mixture development with target densities of 700, 1000 and 1400 kg/m^3 through various experimental studies. This implies shape retention and buildability of 3DP-LWFC as the foremost consideration. Hence, mechanical and microstructural characterisations are performed less extensively, but suitably to confirm and classify the hardened product as construction material. Also, economical consideration is not accounted for when selecting material since this is a prototype development.

Foam stability assessment methods are greatly varied according to microscopic and macroscopic aspects. Active microscopic foam stability assessment for foam itself is recommended to identify the stability of the thin film separating air and liquid at the interface, and protein-based precursor foam itself accordingly. However, there is no specific equipment available to measure foam stability microscopically. Hence, the foam is assumed to be produced stably by the production instruction provided by the supplier. Regarding foam stability in the 3DP-LWFC matrix, there is no standardised test method. The most approachable and widely used method is a gravimetric test, i.e. density check by measured mass of a fixed, known volume, and this method is employed throughout the study.

Once material characterisation is completed, the buildability model proposed by Kruger (2019b) is employed for 3D printing prediction and validation with the available concrete pump and 3D printer setup, discussed in Chapter 2

1.5 Dissertation Structure

This dissertation contains newly written chapters, as well as published journal articles and, at the time of publication, journal articles submitted and under review, following the PhD by publication structure of Stellenbosch University.

Chapter 1 provides a general introduction of the dissertation by furnishing brief background, problem statement, aim and objectives, and scope and limitations. This presents the reader with the brief concept of the dissertation.

Chapter 2 is an overarching overview of a complete 3D concrete printing technology system facilitated at Stellenbosch University. This chapter also deals with the material characterisation of high-performance concrete (HPC), 3DCP procedure, failure mechanism, and 3D printed object observation.

Chapter 3 investigates foam stability of 3DP-LWFC, furnishing a comprehensive background study and void structure characterisations. The influence of base mortar mix on foam stability is addressed. Subsequently, density stability before and after the pumping action involved in 3DP-LWFC is assessed.

Chapter 4 provides an extensive rheological characterisation of 3DP-LWFC with a rotary concrete rheometer. This includes thixotropic behaviour and fresh stiffness, i.e. shear modulus, characterisations. Buildability validation of the material is addressed, and the practical implementation of 3DP-LWFC is proposed.

Chapter 5 is a collaborative work on the influence of nanoparticle incorporation in cementitious material for 3DPC, including LWFC. Improvements of the material in aspects of rheological and mechanical characteristics are dealt with in this chapter.

Chapter 6 draws conclusions on the comprehensive research results of this dissertation. Furthermore, recommendations for future research in 3DP-LWFC are proposed.

Author contribution declarations for each journal article, as well as legal approval by the publisher for re-use of publications, can be found in the Addendum.

1.6 Reference

Ahmed, R.M., Takach, N.E., Khan, U.M., Taoutaou, S., James, S., Saasen, A. & Godøy, R. 2009. Rheology of foamed cement. *Cement and Concrete Research*. 39(4):353–361.

Basařová, P. & Zedníková, M. 2019. Effect of surfactants on bubble-particle interactions, in Ashim Kumar Dutta (ed.). *Surfactants and Detergents*. IntechOpen.

Busta, R. 2016. *Gensler Completes the World's First 3D-Printed Office Building* [Online]. Available http://www.architectmagazine.com/technology/genslerdesigns-the-worlds-first-3d-printed-office-building-in-dubai_o [2016, February 25].

Buswell, R.A., da Silva, W.R.L., Bos, F.P., Schipper, H.R., Lowke, D., Hack, N., Kloft, H., Mechtcherine, V., et al. 2020. A process classification framework for defining and describing Digital Fabrication with Concrete. *Cement and Concrete Research*. 134:106068.

Camacho, D.D., Clayton, P., O'Brien, W.J., Seepersad, C., Juenger, M., Ferron, R. & Salamone, S. 2018. Applications of additive manufacturing in the construction industry – A forward-looking review. *Automation in Construction*. 89:110–119.

Choi, M.S., Kim, Y.J. & Kwon, S.H. 2013. Prediction on pipe flow of pumped concrete based on shear-induced particle migration. *Cement and Concrete Research*. 52:216–224.

De Villiers, W.I. 2019. *Computational and Experimental Modelling of Masonry Walling towards Performance-Based Standardisation of Alternative Masonry Units for Low-Income Housing*. Published doctoral dissertation. Stellenbosch University.

Falliano, D., De Domenico, D., Ricciardi, G. & Gugliandolo, E. 2020. 3D-printable lightweight foamed concrete and comparison with classical foamed concrete in terms of fresh state properties and mechanical strength. *Construction and Building Materials*. 254:119271.

Fameau, A. & Salonen, A. 2014. Effect of particles and aggregated structures on the foam stability and aging. *Comptes Rendus Physique*. 15(8–9):748–760.

Feneuil, B., Roussel, N. & Pitois, O. 2019. Optimal cement paste yield stress for the production of stable cement foams. *Cement and Concrete Research*. 120:142–151.

García de Soto, B., Agustí-Juan, I., Hunhevicz, J., Joss, S., Graser, K., Habert, G. & Adey, B.T. 2018. Productivity of digital fabrication in construction: Cost and time analysis of a robotically built wall. *Automation in Construction*. 92:297–311.

Grudin, J. 2017. *From Tool to Partner: The Evolution of Human-Computer Interaction*. Morgan & Claypool Publishers.

Jones, M.R. & McCarthy, A. 2005. Behaviour and assessment of foamed concrete for construction applications. in *Use of Foamed Concrete in Construction* (Conference Proceedings). Thomas Telford Publishing. 61–88.

Jones, M.R., Ozlutas, K. & Zheng, L. 2017. High-volume, ultra-low-density fly ash foamed concrete. *Magazine of Concrete Research*. 69(22):1146–1156.

Kearsley, E. & Mostert, D. 2005. Designing mix composition of foamed concrete with high fly ash contents. in *Use of Foamed Concrete in Construction* (Conference Proceedings). Thomas Telford Publishing. 29–36.

Kruger, J. & van Zijl, G. 2021. A compendious review on lack-of-fusion in digital concrete fabrication. *Additive Manufacturing*. 37:101654.

Kruger, J., Zeranka, S. & van Zijl, G. 2019a. An ab initio approach for thixotropy characterisation of (nanoparticle-infused) 3D printable concrete. *Construction and Building Materials*. 224:372–386.

Kruger, J., Zeranka, S. & van Zijl, G. 2019b. 3D concrete printing: A lower bound analytical model for buildability performance quantification. *Automation in Construction*. 106:102904.

Licklider, J.C.R. 1960. Man-computer symbiosis. *IRE Transactions on Human Factors in Electronics*. HFE-1(1):4–11.

Marchment, T. & Sanjayan, J. 2020. Bond properties of reinforcing bar penetrations in 3D concrete printing. *Automation in Construction*. 120:103394.

Markin, V., Nerella, V.N., Schröfl, C., Guseynova, G. & Mechtcherine, V. 2019. Material design and performance evaluation of foam concrete for digital fabrication. *Materials*. 12(15):2433.

Mechtcherine, V., Bos, F.P., Perrot, A., da Silva, W.R.L., Nerella, V.N., Fataei, S., Wolfs, R.J.M., Sonebi, M., et al. 2020. Extrusion-based additive manufacturing with cement-based materials – Production steps, processes, and their underlying physics: A review. *Cement and Concrete Research*. 132:106037.

Mose, M.P. & Perumal, D. 2016. Latest advances in alternative cementations binders than portland cement. *IOSR Journal of Mechanical and Civil Engineering*. 13:45–53.

Nambiar, E.K.K. & Ramamurthy, K. 2006. Models relating mixture composition to the density and strength of foam concrete using response surface methodology. *Cement and Concrete Composites*. 28(9):752–760.

Paul, S.C., van Zijl, G.P.A.G. & Gibson, I. 2018. A review of 3D concrete printing systems and materials properties : current status and future research prospects. *Rapid Prototyping Journal*. 24(4):784–798.

Paul, S.C., van Rooyen, A.S., van Zijl, G.P.A.G. & Petrik, L.F. 2018. Properties of cement-based composites using nanoparticles: A comprehensive review. *Construction and Building Materials*. 189:1019–1034.

Pugh, R.J. 1996. Foaming , foam films , antifoaming and defoaming. *Advances in Colloid and Interface Science*. 64:67–142.

van Rooyen, A.S. 2020. *Mechanics and durability of surface treated structural foamed concrete*. Published doctoral dissertation. Stellenbosch University.

Tay, Y.W.D., Qian, Y. & Tan, M.J. 2019. Printability region for 3D concrete printing using slump and slump flow test. *Composites Part B: Engineering*. 174:106968.

Wakisaka, T., Furuya, N., Inoue, Y. & Shiokawa, T. 2000. Automated construction system for high-rise reinforced concrete buildings. *Automation in Construction*. 9(3):229–250.

Weng, Y., Li, M., Ruan, S., Wong, T.N., Tan, M.J., Ow Yeong, K.L. & Qian, S. 2020. Comparative economic, environmental and productivity assessment of a concrete bathroom unit fabricated through 3D printing and a precast approach. *Journal of Cleaner Production*. 261:121245.

Wolfs, R.J.M., Bos, F.P. & Salet, T.A.M. 2018. Early age mechanical behaviour of 3D printed concrete: Numerical modelling and experimental testing. *Cement and Concrete Research*. 106:103–116.

Chapter 2

3D printing concrete technology and mechanics

S. Cho, P.J. Kruger, S. Zeranka & G.P.A.G. van Zijl

Division for Structural Engineering and Civil Engineering Informatics, Stellenbosch University, 7600, South Africa

Reproduced and reformatted from an article published in the *Concrete Beton Journal*.

Abstract

Growing interest in additive manufacturing in the construction industry has promoted research in 3D printing of concrete. A gantry-type 3D printer for concrete was designed and manufactured at the Department of Civil Engineering, Stellenbosch University. Characteristics of 3D printable concrete are investigated and reported. In the fresh state, thixotropic behaviour is required in the form of high static shear yield stress, but relatively low dynamic yield shear stress when the material is agitated by pumping and extrusion in the 3D printing process. Once agitation stops, i.e. when a layer has been 3D printed, fast re-building of the static yield stress is required to retain the printed shape despite self-weight and that of upper layers. In the hardened state, the interfaces in the layered structure may be regions of weakness. Results of rheometer tests to characterise thixotropy, mechanical strength and stiffness tests, as well as interfacial bond strength tests in the hardened state, are presented. An evolution of 3D concrete printed elements is presented.

2.1 Introduction

A research programme on 3D printing of concrete (3DPC) is executed by the Centre for Development of Sustainable Infrastructure (CDSI) at Stellenbosch University. An industrial-grade gantry type 3D printer of roughly 1 m cube build volume, was designed and manufactured in 2017-2018. The point of departure was to develop a robust, versatile laboratory printer that enables research on a range of concrete material classes, printing speeds and geometrical complexity. Knowledge and experience in concrete pumping, spraying and extrusion (Paul *et al.*, 2018; van Zijl, 2015; van Zijl *et al.*, 2016) informed the selection of an appropriate concrete pumping pressure range for the standard to high performance (HPC) grades of concrete and fibre reinforced concrete (FRC).

2.2 Development of a 3D Concrete Printer

Three types of 3D concrete printers are typically used, gantry, robotic, and crane systems (see Fig. 2.1). Each type has merits and drawbacks, however, the gantry type was selected since it is relatively simple and inexpensive to build, versatile and the most common type in the research field. Conceptual, mechanical and electrical design commenced in 2017. The industrial-grade, laboratory scale, gantry-type 3D printer with outer dimensions 1.3 x 1.3 x 1.67 m with a build volume of roughly 1 m^3 was constructed within 7 months.

Fig. 2.1 3D concrete printers: (a) Gantry (b) Robotic (c) Crane type (Paul *et al.*, 2018)

A microcontroller unit (MCU), the core of the 3D printer, controls the input/output (I/O) signals and is powered by a 12 V power supply unit (PSU) to accommodate other electronic features like fans and lighting. The software generated G-code according to the 3D model is interpreted by the MCU and communicates with the stepper motors to produce the required nozzle movement.

The gantry printer allows three translational degrees of freedom (DOF), with the option for future expansion to rotational DOF to enable complex geometrical detail with alternative nozzle shape and size. Currently, a 25 mm diameter nozzle is utilised to print a uniform cross-section around bends in the absence of rotational DOF. The movements of the gantry system in the horizontal plane (x and y-direction) and vertical direction are allowed by the mounted linear guide and rail systems. In the horizontal plane, a belt and pulley system driven by selected stepper motors are employed for each axis, while ball screws are the chosen mechanism for vertical movement of the gantry in which back drive can be prevented if there is a loss of power. The 3D printing platform shown in Fig. 2.2 is a stabilized trolley with 12 polyurethane wheels with an ultimate capacity of 700 kg each. The trolley facilitates the removal and transport of the printed object from the gantry frame. The gantry frame is paired with a 3-phase 380V 3kW locally manufactured concrete pump (Rockcrete TSL), originally purchased for research on the sprayed application of fibre concrete, also known as shotcrete, with a maximum aggregate size of 4 mm. A variable frequency drive (VFD) was supplemented for pump motor speed control, which is also manipulated by the MCU. This enables control of the concrete pumping speed, required for instance when bends of small radius are printed and excessive deposition may result in inconsistent filament thickness, or bulging.

The Marlin firmware based MCU is paired with two G-code based software packages in operator PC, namely 'Slic3r' and 'Simplify3D'. Both packages provide various customizing options for different types of printer and material. Particularly, vase mode printing, printing spirally upwards instead of printing each level of layers, is functional in both software. The option saves time and improves the printing quality for certain objects such as circular columns.

The 3D concrete printer enables the research team to produce laboratory scale structural elements (walls, beams, columns etc.) for testing, with the goal to contribute towards fundamental research for the 3DPC industry. The printer complies with structural design criteria of strength and stiffness, in order to accommodate high volume concrete printing and nozzle head speed without excessive vibration.

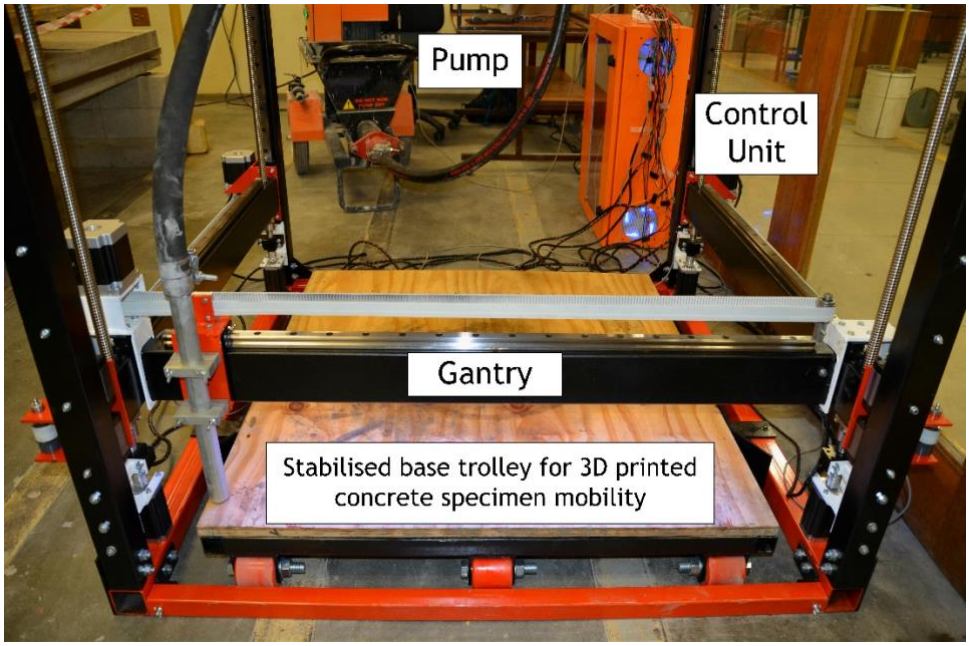

Fig. 2.2 3D concrete printer component layout and final assembly

2.3 Material Characteristics for 3D Printable Concrete

2.3.1 Rheology

3D printing is widely used in various industries, such as the automobile, aviation, biomedical, dental, food, fashion and manufacturing industries. Despite the various and sophisticated additive manufacturing techniques developed, the material deposition and formation are mainly thermal-processed. Hence, heating and cooling techniques are vital features of the printing process. However, the conventional 3D printing deposition and thermal-processed formation, such as metals or plastics, are not essential for concrete, although heating to 60 – 70 ^{o}C can be used for faster setting and strength development. Note that no thermal activation was used in the 3DPC research results reported here. Instead, concrete requires modified rheology through optimised mix design, admixtures and other additions including nano-materials (Kruger *et al.*, 2019a; Kruger *et al.*, 2018) and fibres (van Zijl et al.,

2018) to be suitable for 3D printing in terms of transport (pumpability) and buildability, or extrudability and shape retention under self-weight and subsequently deposited upper layers.

As additive manufacturing is formwork free, the freshly extruded material must have appropriate shape retention, and develop sufficient strength and stiffness rapidly to support subsequent layers. Hence, traditional concrete designed for casting in formwork cannot be directly used. Concrete can be designed to be stiff, or highly viscous, in the form of so-called zero slump / pseudo-solid concrete, by modification of the constituents and their proportions to retain the extruded shape without significant deformation. Shape retention is one of the prime factors influencing the quality of the extruded layer. In contrast, the material is required to have low viscosity at transport during pumping, minimizing the probability of ingredient segregation under high pumping pressure in the range of 1 to 4 MPa (Paul *et al.*, 2018). Segregation may lead to blockage or poor ingredient dispersion and associated inferior mechanical and durability properties of the extruded product. The printing speed, path, size and shape of a printed object also influence the print quality, but the distinct rheological characteristics of the material will notably influence the buildability and pumpability.

Rheology is the branch of physics that studies the deformation and flow phenomena of matter. Material flow initiates when the applied shear stress exceeds the static yield stress of the material. Once the material starts to flow, the measured shear stress reaches a quasi-equilibrium plateau, defined as the dynamic shear stress. A distinct difference between the static and dynamic yield stress of the material is required for 3DPC and is defined as thixotropic behaviour. Thixotropic fluids as dispersions build an intermolecular system of forces at rest, which results in flocculation of particles that increases the viscosity of the fluid, enabling it to support its own weight (Björn *et al.*, 2012). Flow initiates when the intermolecular structures are broken by external energy via agitation, resulting in shear-thinning of the material. This phase is called de-flocculation, which reduces the viscosity of the material. Once the external energy is removed, the thixotropic material starts to re-flocculate and regains pseudo-solid behaviour as the original microstructure is rebuilt and the original viscosity is restored. This 3-phase thixotropic behaviour is depicted in Fig. 2.3 (c). Each phase illustrated in the figure can be closely associated with the following timescales:

- Flocculation: concrete is placed into the hopper of the pump.
- De-flocculation: the material is agitated by feeding the material into the hose by rotational paddle or auger, and pumped through the hose.
- Re-flocculation: the material is extruded and deposited onto the printing bed or a previous layer.

The thixotropic behaviour is determined by several factors including the water content, temperature, chemical admixtures, cement extenders, aggregate grading, and rate of hydration. The restoration rate between the static and dynamic yield stress can be considered as the degree of thixotropy. A higher degree of thixotropy is desired for 3D printing application in concrete. The degree of thixotropy can be

characterised by measurement of the shear stress of the fresh concrete with a rheometer. The measured initial static and dynamic yield stresses are 1860.4 Pa and 1474.4 Pa according to Fig. 2.3 (b). The test result further shows rapid restoration and build-up of the static yield stress within a short period of less than 1 minute. Note that return of the 3D printer nozzle to deposit an upper layer varies according to nozzle speed and the printed structural element's geometry and size. Typical return periods can be several minutes. For a laboratory test 3D print of a 400 mm diameter circular hollow column, the return period is 21 seconds with a 60 mm/s printing head speed. The re-building rate of the material static shear yield stress, is used to design a 3D concrete printing process, in order to prevent instability and collapse of the unsupported printed object, considering the geometry and print settings (Kruger et al., 2019b). Fig. 2.4 presents a time-evolution of static yield shear stress, collecting the peak shear stress values from Fig. 2.3 (b), and more at longer waiting periods up to initial set of the concrete. The graph in Fig. 2.4 serves as a 3DPC design tool for the time-dependent resistance, which must exceed the demand, typically the weight of upper layers as 3D printing progresses. The initial gradient of static yield shear strength evolution is depicted by R_{Thix}, referring to the rapid rebuilding by re-flocculation. The second gradient is depicted A_{Thix}, which refers to a lower rate of strengthening, brought about a structuration process following re-flocculation (Fig. 2.3 c).

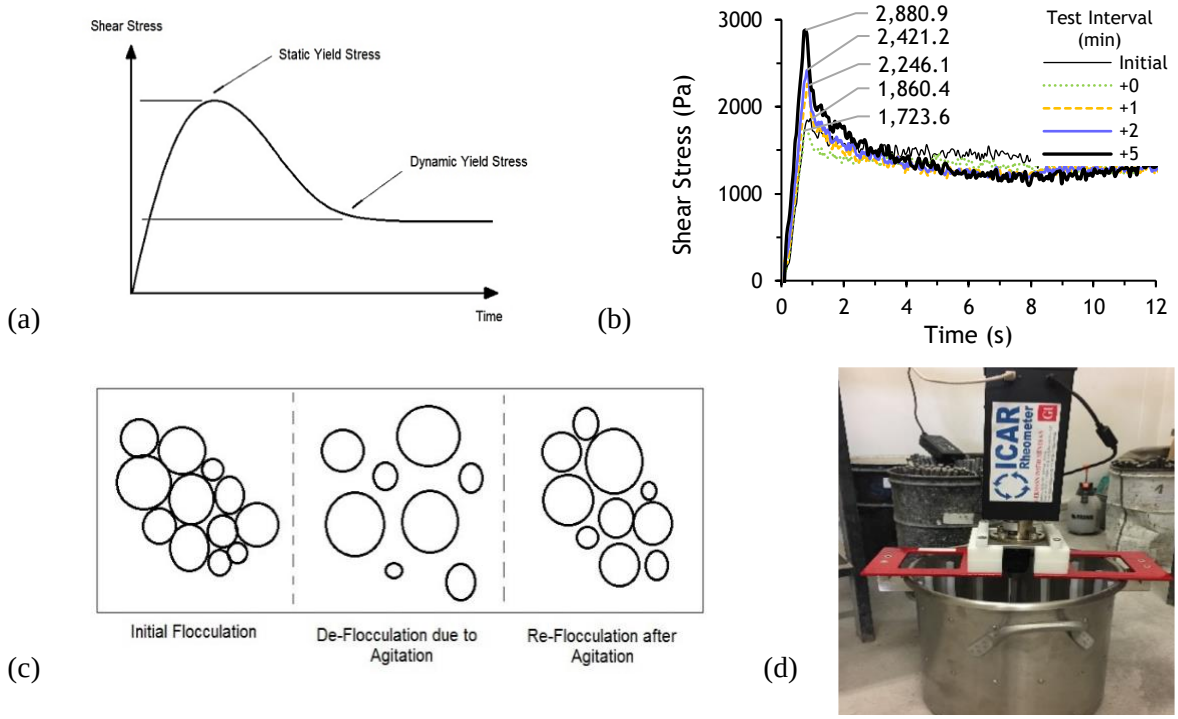

Fig. 2.3 (a) Stress growth rheological test result depicting the clear difference between the static and dynamic shear yield stresses of a thixotropic material; (b) static yield stress re-building test result with different resting periods. The result shows rapid static yield restoration after agitation; (c) break-down and build-up phases of thixotropic materials illustrated by means of particle flocculation; (d) German Instruments ICAR Rheometer direct viscosity measurement setup used in the work reported here.

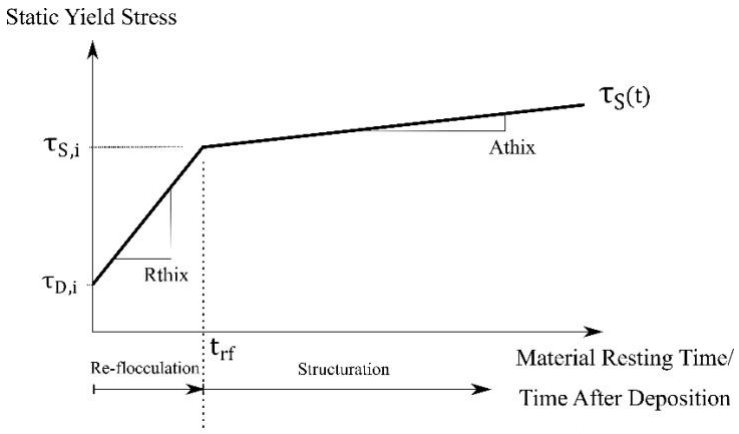

Fig. 2.4 Static yield shear strength as a function of time illustrated by re-flocculation and structuration mechanisms (Kruger *et al.*, 2019b)

The 3D printable mix was designed mainly based on the rheological performance of the material. From the literature (Nerella *et al.*, 2016; Le *et al.*, 2012), the optimal mix design was developed with locally available constituents, including CEM II/A 52.5N cement, Class S fly ash, silica fume (Microfume supplied by Silicon smelters), and natural Malmesbury sand with fineness modulus of 2.12. The final mix design, with water-to-cement ratio of 0.45, is presented in Table 2.1. Note that polypropylene (PP) fibres are included in the mix. The relatively low volume content and stiffness of PP fibres incorporated here controls plastic shrinkage cracking and reduces brittleness of the printed product (van Zijl *et al.*, 2018). In continued research, the authors are investigating incorporation of high strength and high stiffness polymeric fibres to enhance hardened mechanical properties, including flexural strength and toughness.

Table 2.1 Mix design of a 3D printable mortar

Constituent	Mass [kg]
Cement (CEM II 52.5N)	579
Fly Ash	165
Silica Fume	83
Sand	1167
Water	261
PP fibre (6mm)	0.45% by volume of mix
Superplasticizer	1.48% by mass of binder
Viscosity Modifying Agent	0.13% by mass of binder

The Fuller Thompson theory (Fuller, 1907), which aims to achieve maximum packing density, is used as optimal aggregate grading target. The shear rate of cement paste is inversely proportional to granular aggregate packing fraction (Roussel, 2006) in which the shear rate is determined by the state of flocculation. Maximum packing and minimum voids are expected to yield lower shear rates and higher

state of flocculation. A recent study by Weng *et al.* (2018) confirms that the Fuller Thompson theory can serve as a reasonable rheological design approach for 3DPC. A natural sand available in the Western Cape is selected for use in the 3DPC mix reported here. It is possible to achieve a Fuller-Thompson grading curve by sieving and re-mixing, which is generally an expensive process. Given the reasonable agreement with the ideal curve shown in Fig. 2.5, and associated cost of re-grading, the natural sand is accepted. Note that Fig. 2.5 shows the combined grading of the binder and sand particles.

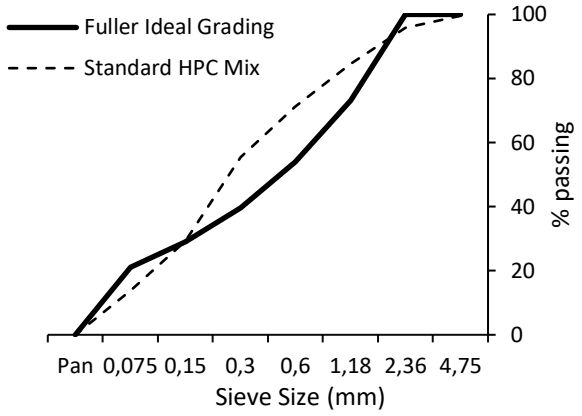

Fig. 2.5 Particle size distribution of the binder and sand combined, compared to Fuller-Thompson's ideal curve

2.3.2 Mechanical properties

Rheology in the fresh state determines 3D print quality, however the mechanical robustness in the hardened state is also crucial. The compressive strength, f_{cu}, determines the particular structural application class and is conventionally used as a quality control parameter of concrete. It is often linked to several other mechanical properties of concrete, such as Young's modulus, E, and flexural capacity, f_{flex}, of concrete by correlation, making it an important material property.

The concrete further gains strength through crystallisation and structuration inside of the concrete mass over time, through the process of hydration. High strength concrete (HPC) is defined by the American Concrete Institute (ACI) as concrete with 28-day compressive strength of at least 55 MPa (Russell, 1999). Table 2.2 summarises the compressive and flexural strengths, as well as Young's modulus of the concrete used here for 3DPC. Note that standard specimen preparation and testing were performed according to EN 196-1 for four-point flexural tests, and ASTM C469-02 for Young's modulus. Flexural specimens of size 40 mm x 40 mm x 160 mm and Young's Modulus specimens of 100 mm diameter and 200 mm height were cast in regular moulds, protected and stripped after 1 day, and water cured at 23±2°C until the age of testing. However, the 3DPC process might alter the material microstructure and thus also the mechanical properties. Also, without the protection of moulds, earlier drying might occur. In addition, the interface between layers may significantly alter mechanical behaviour. To a large extent, strong interfacial bond may counter such changes, by appropriately binding layers to respond as a continuum. To verify the interfacial bond, flexural tests were performed on beam specimens of roughly

40 mm x 40 mm x 160 mm cut from a 3D printed structure, as schematised in Fig. 2.6. Flexural tests were performed in a Zwick Z250 materials testing machine (MTM) with a span length *(l)* of 150 mm, and loaded at third points (*x = 50* mm*)*. All specimens failed at an interface within the uniform bending moment zone (between load points). From the ultimate load, the maximum flexural strength was calculated, considering linear elastic behaviour, i.e. the modulus of rupture was calculated. These flexural strengths are denoted the interfacial (flexural) bond strength (IBS) in Table 2.2, and determined at 28 day age only on three specimens. Note that the 3D printed column was kept in laboratory conditions at 23±2ºC and 65±5% relative humidity until sawing the specimens and subsequent testing.

Table 2.2 Mechanical characteristics of 3D printable mortar (coefficient of variation in brackets)

Age	f_{fl} (MPa)	f_{cu} (MPa)	E (GPa)	IBS (MPa)
1 day	1.7 (0.081)	7.9 (0.026)		
7 days	7.3 (0.050)	55.6 (0.006)	26.6 (0.023)	
28 days	8.4 (0.057)	70.6 (0.103)	30.8 (0.020)	6.8 (0.021)
56 days	8.7 (0.02)	80.0 (0.151)		

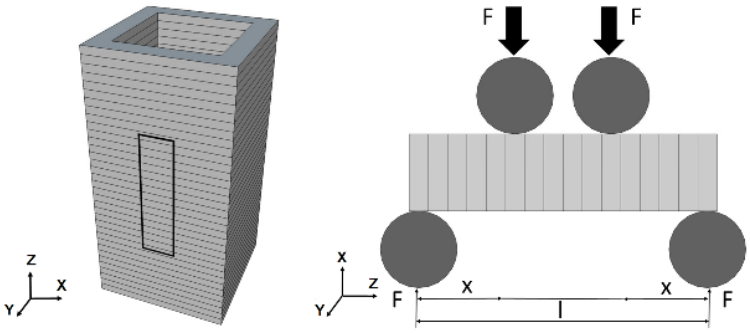

Fig. 2.6 Interlayer bond strength (IBS) (a) specimen cut from a 3DPC column, (b) flexural test setup

The 19% lower interfacial flexural strength (IBS) of 6.8 MPa, compared with the cast specimen flexural strength of 8.4 MPa could be ascribed to both the curing regime and the interfacial bond characteristics. Note that there was a short time lapse of less than one minute between printing successive layers in the 3DPC column. Interfacial bond is the subject of continued research by the authors. To investigate the potential of plastic shrinkage and cracking of 3DPC structures, due to the lack of mould protection, plastic shrinkage tests were recently performed and reported by the authors (van Zijl *et al.*, 2018). For the particular mix presented here, no plastic shrinkage cracks occurred, even at extreme climatic conditions of 20 km/h wind, 40ºC air temperature and 10% relative humidity.

2.4 3D Concrete Printing Procedure and Product Evolution

2.4.1 Printer calibration

Since the concrete material is novel to 3D printing, none of the commercially available 3D printing software has material pre-set values for concrete. Hence, the determination of the primary printing parameters, such as the extrusion rate, print head speed and layer height, was necessary before printing an object. The fixed parameters are shown in Table 2.3.

Table 2.3 Fixed printing parameters based on the printer specification

Nozzle diameter	25 mm
Filament diameter	25 mm
Extrusion width	25 - 30 mm
Build volume	990 x 860 x 980 mm (X, Y and Z)

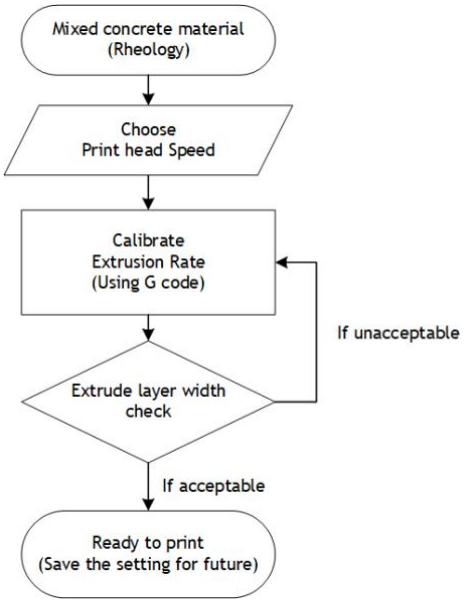

Fig. 2.7 Flowchart depicting the process of obtaining correct layer width for various concrete materials with different rheology

Recall from Section 2.3 that freshly mixed concrete has a certain stiffness and flowability based on the constituents. Since the material rheology cannot be modified simply without changing mechanical properties, the stiffness and flowability of the material must be characterised or investigated in advance to be acceptable for printing, while also attaining appropriate mechanical properties in the hardened state. Thus, the print head speed is only considered as a variable parameter to determine the optimum extrusion rate. The printing speed was tested within a range of 50 – 100 mm/s based on the previous study by Nerella et al. (2016). Since the standardised test for printability of the material has not yet been developed, the determination of the parameter was judged by the authors. For each printing speed, the

extrusion rate must be calibrated until the extruded layer width does not exceed the nozzle diameter by 5 mm, thus a layer width in the range of 25 – 30 mm.

The structural component in the construction environment is, first of all, desired to have global stability then detailing. Hence, the buckling effect as a cause of failure is disregarded to investigate the buildability of the concrete material. A cylindrical hollow column is chosen for a buildability test model. The printing time, the compressibility of each printed layer under the self-weight and printed object height were compared in each printing outcome. The optimum layer thickness was investigated by printing the buildability model. The layer thickness directly affects the interlayer bond strength, which influences the integrity of the structural component and its mechanical properties. The layer thickness was obtained in the range of 10 – 15 mm depending on the condition of the material.

During the calibration process, a few typical observations (Fig. 2.8) of trials performed showing imperfection and irregularity in quality or global failure:

(a) A loose translational pulley not engaged properly with stepper motors resulting in a slip. The slip causes an inaccurate print path or shifting of the printing plane entirely.
(b) Residual water inside of the hose altering the flowability of the material.
(c) At the vertical lifting position for each layer, extra material is deposited due to gravity feed. Thus, an actuator at the nozzle is required to control material flow more accurately.
(d) Printing a bathtub. The action described in (c) causes global deflection of the wall.

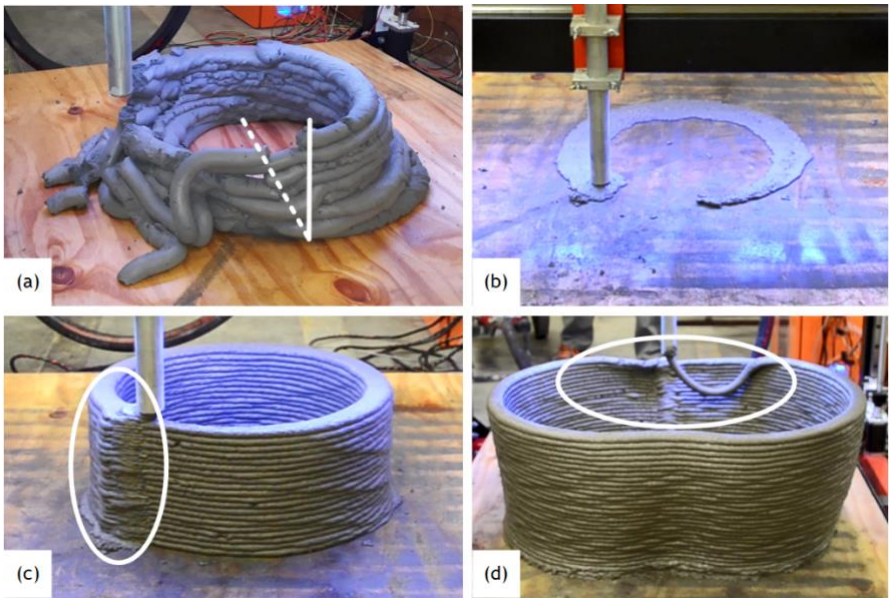

Fig. 2.8 Typical poor condition or failure during the printing process

2.4.2 Printing quality and shape retention

A 400 mm diameter circular hollow column is 3D printed and shown in Fig. 2.9 (a) and (b) to demonstrate progressively improved control and material performance. The nozzle translational speed

while printing of 60 mm/s was maintained for all prints. The very first 3D printed specimen of the group is shown in Fig. 2.9 (a), using a mortar material by another research group (Paul *et al.*, 2018). The specimen exhibited inconsistent layer thickness and some discontinuity in printing due to pump feeder air ingress and poor control in pump speed. The air ingress is caused by the high viscosity of the material, which required more agitation energy in the hopper to feed uniformly. The poor surface quality is shown in the figure which indicates inadequate rheology for 3DPC. The average layer thickness was not recorded since the specimen collapsed due to operator error just after the print process.

The subsequent specimen, shown in Fig. 2.9 (b) showed a near perfect cylindrical column of 47 layers (height 471 mm) despite the presence of additional material deposits at the layer print start position. The rheological improvement of the material led to the notably improved uniformity of the extruded layer and the surface quality. Since a discontinuity is observed at some points, an extra energy source (poker vibrator in hopper) was considered to improve consistency.

Lastly, Fig. 2.9 (c), the Ø250 mm circular hollow column was printed to validate buildability model. The small addition of retarder helped to reduce the required agitation energy for consistent layer printing by extending the period of the fresh state and reducing dynamic yield stress. A concrete poker vibrator is employed to provide additional agitation energy in the hopper. The material modification, together with the poker vibrator usage, resulted in 59 layers (height 590 mm). The use of vase mode improved the uniformity in layer thicknesses. As the specimen was printed until failure for the buildability test, the average layer thickness was not recorded.

(a)  (b)  (c) 

Fig. 2.9 Progression in 3D concrete printing control and material rheology at SU: (a) First printed circular column; (b) improved layer uniformity and surface quality due to improved rheology and pump speed control at the onset of new layers; (c) the buildability test model was printed with increased height before collapse due to plastic yield of bottom layers

(a)  (b) 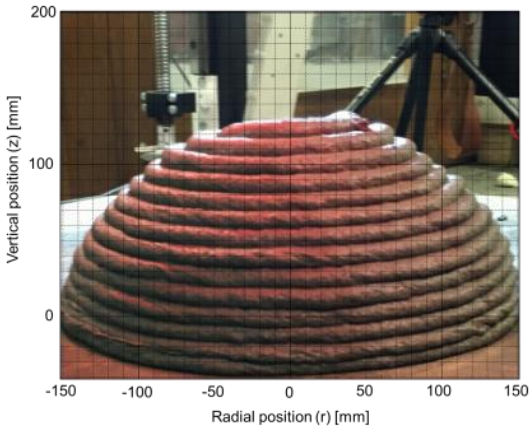

Fig. 2.10 3D printing of (a) fibre concrete column with a 90 degree twist over 0.6 m of the 0.8 m height of 70 layers, showing a top and side view on the right; (b) benchmark dome (Bester *et al.*, 2019)

The geometrical complexity was also validated with a 90 degree twisted square column (Fig. 2.10 a). Irregular layers are seen to be reduced, but still appear due to pump feeder air ingress. However, both specimens could be 3D printed while remaining stable even with the geometrical complexity and high construction rate – see Table 2.4. Finally, benchmark structures for 3DCP quality assessment and standardisation have recently been proposed by the authors (Bester *et al.*, 2019). Fig. 2.10 (b) shows a 3D printed half-sphere dome structure, overlain by a grid for geometrical precision assessment (Bester *et al.*, 2019). The dome structure remained stable, but the pre-final layer (layer number 14, Table 2.4) introduced local instability due to deformation of the upper layers, which have increasingly small interfaces with the support layers. The varying ascending gradient of the dome-structure presents a stringent test for material stability and 3D printer precision.

2.4.3 Buildability and construction speed

While printing the specimen, the 3D printing duration is recorded to correlate the buildability limit with respect to time constraint. The initially printed circular and square columns were printed up to 40 – 70 layers within 30 minutes, excluding the collapsed specimen (Fig. 2.10 (c)) which was purposefully printed at smaller dimension with the same speed. As the material improvement enabled printing to near full height of the gantry frame, the buildability model of higher aspect ratio (height/diameter) with smaller diameter and increased print speed was tested.

As result, the specimen printed with the material of improved rheology by admixtures was printed up to 59 layers within approximately 13 minutes as specified in Section 2.4.2. The failure mechanism is plasticity of the material in the bottom layers, but remains to be confirmed in continued research to rule out geometrical failure (buckling) as cause of the instability.

Details of overall specimen geometry and layer thickness are summarised in Table 2.4.

Table 2.4 3D printed object geometry. Average of 2 - 4 readings (coefficient of variation in brackets)

Figure	Layers	Width (mm)	Height (mm)	3DP duration (min:s)	Average layer thickness (mm)		Remarks on material/control improvement
					Base	Top	
2.9a	40	-	-	13	-	-	Collapsed due to operator error, poor quality surface
2.9b	47	402.5 (0.002)	478.0 (0.033)	21	11.9 (0.046)	9.3 (0.141)	Best print. Good quality surface, improved software control.
2.9c	59	-	590	13	-	-	Uniform layer and best buildability
2.10a	70	250.5 (0.003)	792.5 (0.003)	26	11.9 (0.046)	12.6 (0.152)	Good print; but irregular layers shown due to air ingress
2.10b Dome	14	300	125	3:04	-	-	Reasonable print of varying ascending slope geometry

2.5 Conclusions

3DPC is a burgeoning research field allowing for the creation of innovative construction methods, technology and building materials. What is lacking in the current literature is the characterisation of the materials appropriate for 3DPC, as well as utilising advanced/high-performance composites together with this unique construction method. The 3DPC research team at Stellenbosch University has taken significant steps in the last 2 years in this regard, with the construction of the first industrial-grade gantry type 3D concrete printer on the African continent and preliminary tests on high strength fibre-reinforced concrete for 3DPC. The following conclusions are drawn.

- For successful 3D printing of concrete, a thixotropic material is required to enable pumping and extrusion without segregation and blockage. Once agitation by pumping and extrusion stops, a high static shear yield stress must develop at a rate higher than the building or layer deposition rate, in order to resist the weight of upper layers. Structural collapse will occur at too low rebuilding rates due to plastic yielding of lower filament layers.
- From rheometer stress growth test results the evolution of static shear yield strength can be determined and represented by a bi-linear approximation. From this resistance curve and the demand of upper layer weight, a building rate can be determined that will prevent collapse by plastic yielding.
- An average interfacial flexural bond strength of 6.8 MPa, 19% lower than the inherent composite flexural strength of 8.4 MPa was determined in four point bending tests.

- An evolution in successful 3D printing of concrete elements has been presented. This has led to the proposal of standardisation through benchmark structures for 3D printing of concrete. This presents a stringent test of material suitability, as well as 3D printer precision.

Current work involves developing a range of 3D printable concretes, and the development of prefabricated structural elements and connections for on-site assembly, towards industrialised hybrid construction of low to medium-rise housing.

2.6 References

Bester, F.A., van den Heever, M., Kruger, P.J. & van Zijl, G.P.A.G. 2019. Benchmark structures for 3D concrete printing. *fib Symposium*. 27-29 May 2019, Krakow, Poland.

Björn, A., de La Monja, P.S., Karlsson, A., Ejlertsson, J. & Svensson, B.H. 2012. Rheological characterization, Biogas. S. Kumar (ed.). InTech.

Fuller, W.B., Thompson, S.E. 1907. The laws of proportioning concrete. *Transactions of the American Society of Civil Engineers*. 59(2):67–143.

Kruger, P.J., van Zijl, G.P.A.G., Cho, S. & Zeranka, S. 2018. Multi-physics approach for improved thixotropy of cement-based materials for 3DPC. *Proceedings 3DCP*. 26-28 Nov 2018, Melbourne, Australia.

Kruger, P.J., van den Heever, M., Cho, S., Zeranka, S. & van Zijl, G.P.A.G. 2019a. High-performance 3D printable concrete enhanced with nanomaterials. Sustainable Materials, Systems and Structures (SMSS) – New generation of construction materials, *RILEM Spring Convention*. 18-22 March 2019, Rovinj, Croatia.

Kruger, P.J., van Zijl & G.P.A.G., Zeranka, S. 2019b. 3D construction printing: A lower bound analytical model for buildability performance quantification. *Automation in Construction*. 106: 102904.

Le, T., Austin, S., Buswell, S., Gibb, G. & Thorpe, A. 2012. Hardened Properties of high performance printing concrete. *Cement and Concrete Research*. 42:558–566.

Nerella, V.N., Krause, M., Näther, M. & Mechtcherine, V. 2016. Studying printability of fresh concrete for formwork free Concrete on-site 3D Printing technology (CONPrint3D), *In Proceeding for the 25th Conference on Rheology of Building Materials*. Regensburg, Germany.

Paul, S.C., Van Zijl, G.P.A.G., Tan, M.J. & Gibson, I. 2018. A review of 3D concrete printing systems printing concrete – Current status and future research prospects. *Rapid Prototyping Journal*, 24(4):784-798.

Roussel, N. 2006. A thixotropy model for fresh fluid concretes: Theory, validation and applications. *Cement and Concrete Research*. 36(10):1797–1806.

Russell, H. G. 1999. ACI defines high-performance concrete, *Concrete International*, 21:56-57.

van Zijl, G.P.A.G. 2005. Optimisation of the composition and fabrication methods, applications for precast concrete members, *In: Hochductile Betone mit Kurzfaserbewehrung – Entwicklung, Prüfung, Anwendung*. V. Mechtcherine (ed.). pp. 37-54.

van Zijl, G.P.A.G., Kruger, P.J., Cho, S. & Zeranka, S. 2018. 3D printing polymer fibre concrete. *In: Proceedings of the International Inorganic-Bonded Fiber composites Conference*. 23-26 Oct 2018, Cape Town, South Africa.

van Zijl, G.P.A.G., Paul, S.C. & Tan, M.J. 2016. Properties of 3D printable concrete, *Proceedings 2nd International Conference on Progress in Additive Manufacturing (Pro-AM 2016)*. 16-19 May 2016, Singapore.

Weng, Y., Li, M., Tan, M.J. & Qian, S. 2018. Design 3D printing concrete materials via Fuller Thompson theory. *Construction & Building Materials*. 163:600–610.

Chapter 3

Foam stability of 3D printable lightweight foamed concrete

Seung Cho[1], Algurnon van Rooyen[1], Elsabe Kearsley[2], Gideon van Zijl[1]

[1-] Division for Structural Engineering and Civil Engineering Informatics, Department of Civil Engineering, Stellenbosch University, Stellenbosch, 7600, South Africa

[2-] Department of Civil Engineering, University of Pretoria, South Africa

Reproduced and reformatted from an article submitted to the *Construction and Building Materials Journal*.

Abstract

Hybridisation of foamed concrete, a lightweight construction material, with 3D concrete printing (3DCP), an extrusion-based additive manufacturing technology, holds the potential of synergetic energy and cost benefits in infrastructure. Air voids in foamed concrete are formed by the included aqueous foam – a network of bubbles separated by thin film wall; thus, a notable breakdown of foam by the pumping process in 3DCP must be avoided. This study reports an interdisciplinary background study on the general foam stability and potential concerns during the 3DCP process. Foam stability is, firstly, investigated in various base mixes with different quantified rheological properties characterised with a concrete rheometer without pumping pressure involvement. The investigation subsequently investigates a wide density range in foamed concrete density, namely 700, 1000, 1400 kg/m^3, in both static and dynamic environment by measuring density consistency. Foam stability is secured over the entire pre-pumped sample range, i.e. static foam stability, but a densification is found in the higher density post-pumped samples, i.e. dynamic foam stability. The void structure of the cast samples is studied by X-ray CT scans to compare the measured porosity by defect analysis with the theoretical porosity and quantified data is presented.

Highlights

- An interdisciplinary foam stability theory and experimental investigation are presented.
- Foam stability secured 3D printable foam concrete with a wide density range is developed.
- Theoretical and measured porosity compared in the foam stability study.

Keywords: Foamed concrete; 3D printed concrete; foam stability; void structure; digitally fabricated concrete

3.1 Introduction

Foamed concrete normally consists of a cement paste or mortar that is aerated with a foaming agent to reduce the density of the material, resulting in thermally efficient building material. The air voids are introduced to the mortar in the form of an aqueous foam and the foam stability in the pseudo-solid or elastoplastic material is crucial for quality control. The stability of the foam is not only dependent on the shape and the size of the bubbles in the foam, which are determined by the type of foaming agent and production procedure, but also on the rheology of the paste surrounding the air bubbles.

The development of an extrusion-based digital construction technique, widely known as 3D concrete printing (3DCP), introduces automation in construction allowing construction time and cost reduction, equipping highly skilled workforces and architectural design flexibility as no formwork is involved (Paul *et al.*, 2018). Despite problems with reinforcement and standardisation, 3DCP is unquestionably seen to shift the paradigm shortly in the traditional construction sector thanks to the tireless involvement from academia, industry, public and government. Along with the innovation, there are a few attempts to hybridise 3DCP with lightweight building materials, in particular foamed concrete (Falliano *et al.*, 2020; Markin *et al.*, 2019), to lessen the dead load of the structure and to promote energy efficiency. Those studies showed potential, but further research is required to ensure that the air voids in the foamed concrete can sustain the mechanical agitation and pressure since pumping processes are involved for material transport in 3DCP.

In this paper foam stability with various foam volume fractions and the effect of pumping on the stability of the voids in foamed concrete are investigated. The first part of the paper investigates the influence of the rheology of base mortar mix on foam stability. A stable base mix with the most favourable constructability of 3DCP was chosen based on the first part of the study. The base mix was then used to produce three different densities of 3D Printable Light Weight Foamed Concrete (3DP-LWFC) by varying foam volume fraction for the second part of the study. Prepared fresh concretes were fed into a positive displacement 3D concrete pump and the gravimetric measures of pre- and post-pump densities recorded. Similar experimental work was performed with controlled negative pressure, up to 80 kPa, to study foam stability under constant pressure. X-ray computed tomography (X-CT) was performed in

the second part of the study only for a comparative study on void structure, i.e. porosity, void size distribution, etc.

3.2 Background on Foam Stability

A diluted aqueous surfactant solution flows through a mechanical agitation process with high air pressure to produce a precursor aqueous foam. In the system of aqueous foam, the amphiphilic surfactant molecules populate and adsorb around the air-liquid interface, at the nanometre scale, with the hydrophobic parts in contact with air which creates a thin film, i.e. the surface of a micelle, separating the individual bubbles having a size range of micrometre to centimetre (Fameau & Salonen, 2014). When the thin films are in contact, a liquid skeleton of interconnected channels at the junction points are created by a substantial Laplace pressure difference between the gas and the liquid phase due to the small bending radius of a bubble, known as the Plateau border (Butt, Graf & Kappl, 2003). Foam comprises the network of bubbles and the physical and physicochemical properties of the foam are mainly dictated by the properties of the lower length scales (Fameau & Salonen, 2014).

Since all foams are thermodynamically unstable (Pugh, 1996), foam destabilises over time, so-called foam ageing, with the following mechanisms: (1) *drainage* of gravity-driven liquid flow leading to the separation of the gas and the liquid, (2) *ripening* or *coarsening* where gas diffusion occurs between the different size of bubbles due to the differential Laplace pressures, and (3) *coalescence* which is a merging process of bubbles by film rupture at a critical thickness (Fameau & Salonen, 2014). It should be mentioned the three mechanisms are not discrete, but rather interdependent (Phan *et al.*, 2003).

The liquid film thickness reduces over time. This film thinning process continues until it reaches a metastable equilibrium state, and highly influences the foam stability or the destabilisation rate. Intrinsic physical and physicochemical properties of bubbles, such as surface tension, surface rheology, and film elasticity are mainly determined by the solution concentration and type of surfactant (Wang & Yoon, 2008), but also surface forces which can be explained by a classical DLVO theory (after Derjaguin, Landau, Verwey, and Overbeek) (Basařová & Zedníková, 2019), control the process. The theory explains the aggregation of dispersed particles in a liquid medium by the force balance primarily between two forces, the attractive van der Waals force and the repulsive electrostatic double-layer force (Basařová & Zedníková, 2019; Butt *et al.*, 2003; Pugh, 1996). The balanced surface forces develop a pressure within the liquid lamella to determine the metastable film thickness and the pressure difference between the pressure developed within the film and the applied bulk pressure, called disjoining pressure (Π_d), is defined as the change in Gibbs free energy per unit area with respect to lamella thickness (Derjaguin *et al.*, 1987). Both attractive and repulsive surface forces change over the distance between particles. The disjoining pressure can be expressed in terms of film thickness, h. An idealised disjoining pressure isotherm is depicted in Fig. 3.1.

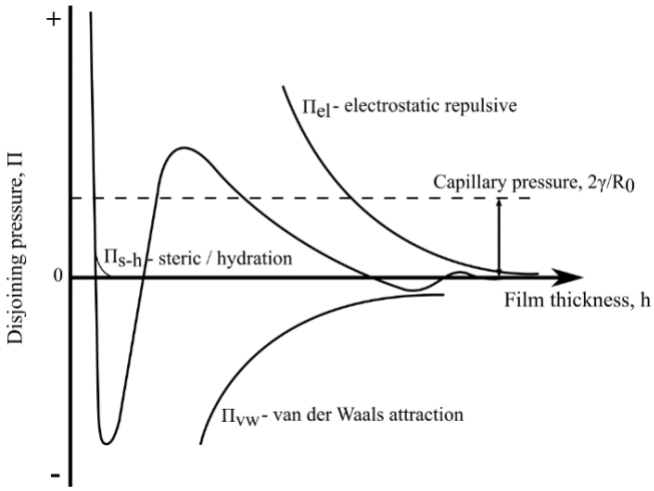

Fig. 3.1 Idealised disjoining pressure isotherm

In a macroscopic aqueous foam, i.e. two-phase system, a (Laplace) capillary pressure, P_σ, develops based on the size of the bubble and surface tension and competes with the disjoining pressure to determine the driving pressure, ΔP, leading to the formation of an equilibrium film. The pressure balance gives

$$\Delta P = P_\sigma - \Pi_d \tag{3.1}$$

When the aqueous foam is incorporated into a cementitious paste, it becomes a multi-phase system, and the foam destabilisation mechanism in the bulk material is subtly modified as the concrete paste separates individual bubbles due to the high solid concentration. The foam bubble is surrounded by the solid paste, i.e. adsorption due to the interplaying surface forces, and the complex solid-bubble interaction takes part in the stability of the foam. A bubble and solid particle approach each other with velocity inducing kinetic energy (*collision*) during a stable cement grain-bubble agglomeration formation (*attachment*) (Fameau & Salonen, 2014; Phan *et al.*, 2003). At an attachment state, the bubble is suppressed by the bulk solid paste and the suppressing pressure, or more common term 'confinement pressure' and denoted as P_c, depending on the bulk density, viscosity and yield stress of solid paste (Jones *et al.*, 2016). Then the pressure balance becomes

$$\Delta P = P_c + P_\sigma - \Pi_d \tag{3.2}$$

For the 3DP-LWFC, there is a rheological requirement for the material that must have sound shape retention and buildability during the construction phase which requires a certain level of yield stress, 0.27 – 0.9 kPa according to (Le *et al.*, 2012). Aqueous foam incorporation tends to decrease the yield stress of the base mix (Feneuil *et al.*, 2019a). The base mix, hence, requires higher yield stress than the nominal rheological requirement. Several studies suggest that high yield stress of solid paste can theoretically retard or completely arrest the drainage and the ripening destabilisation mechanisms by capturing the mobility of a bubble completely (Fameau & Salonen, 2014; Feneuil *et al.*, 2019); however,

the increased confinement pressure may lead to significant bubble breakage by film rupture or coalescence of bubbles.

Pumping is a crucial process in the 3D concrete printing technique. It is widely known that pumping pressure results in the loss of air content, approximately 1% - 1.5% air content loss in the case of a conventional concrete (Hover & Phares, 1996; Lessard *et al.*, 1996). During concrete material transport to the targeted height or position via either a progressive cavity pump, the most common concrete pumps, pumping pressure builds up within the transporting channel (e.g. pipe), so does internal pressure of the concrete matrix. Since the pumping pressure is dependent on various factors, e.g. rheology of the bulk material, pipe geometry, and flow rate, there is no particular quantifying study available in the literature, but the pumping pressure can be generally expected to be 70 kPa (0.7 bar) or higher (Mechtcherine *et al.*, 2020; Panda *et al.*, 2017). The pumping pressure, P_P, is added on the right-hand side in Eq (3.2), leading to

$$\Delta P = P_c + P_\sigma + P_P - \Pi_d \tag{3.3}$$

In concrete pumping, a thin slippage layer is formed, having significantly lower yield stress and plastic viscosity, in between the bulk material and the wall of the pipe, the so-called lubrication layer, mainly due to the Shear-Induced Particle Migration (SIPM) (Choi *et al.*, 2013). Depending on the pumping conditions and the rheological performance of the material, the two flow modes are defined as the slip flow mode, i.e. thin lubricating layer and unsheared plug flow, or the slip-plus-shear flow mode, i.e. a transitional zone present in between the lubrication layer and the unsheared plug flow (Mechtcherine *et al.*, 2020). The SIPM also increases the particle concentration, plastic viscosity and yield stress of bulk material away from the lubrication layer. Thus, this particle migration mechanism is postulated to promote the chance of bubble coalescence due to the increased rheological parameters, but also the continuous kinetic environment of solid particles and bubbles.

Several studies have investigated the foam stability in the cementitious material with a rheological approach. Kearsley et al. (2005) proposed, using the hydraulic flow turntable test, a fluidity range of the base mortar mix, expressed as a slump flow of 220 – 250 mm, for stable foamed concrete production. The authors postulated the degree of saturation of cement grain affects foam stability due to water withdrawal from the film for hydration, which may cause bubble film rupture. Feneuil et al. established a rheological investigation of cement paste for stable morphology-controlled cement foam production (Feneuil *et al.*, 2019b) and a foam stability criterion (Feneuil *et al.*, 2019). The study found a bubble size-dependent destabilisation mechanism in which drainage and ripening are the principal mechanisms and foam instability was found when the yield stress was greater than 10 Pa (up to 100 Pa was considered in the study). However, it is worthwhile to mention that cement foam and foamed concrete must be distinguished because of the substantial solid fraction difference.

3.3 Experimental Programmes

3.3.1 Materials and mix design

Foamed concrete composition design is not standardised to date, but several researchers take into consideration the target wet density (ρ_t) as a prime design factor (Kearsley & Mostert, 2005; van Rooyen, 2020; Wei *et al.*, 2013). Kearsley (2005) proposed a mix design based on the mass and volume balances of constituents with two variables, the cement mass (c) and foam volume (V_f). The sum of dry constituents, free water (w) and foam mass ($RD_f.V_f$) with *RD* denoting relative density, dictates the first equation, Eq. (3.3.4), and this must be balanced with the prime design factor, i.e. target density in the fresh state. The second equation, Eq. (3.3.5), is to consider the unit volume, e.g. one cubic meter, which is equal to the total volume of the entire composition of constituents.

$$\rho_t = c + c \cdot (w/c) + RD_f \cdot V_f \tag{3.4}$$

$$1 = c/RD_c + c \cdot (w/c) + V_f \tag{3.5}$$

These equations can be expanded as additional ingredient materials, such as supplementary cementitious materials (SCMs), and inert materials are included. In this study, the mix design includes calcium sulphoaluminate (*CSA*) cement, fly ash (*a*), silica fume (*sf*), graded fine silica sand (*s*) and nano-silica powder (*nS*) to improve the material performance in both fresh and hardened states (Jones & McCarthy, 2005; Kearsley & Mostert, 2005; Nambiar & Ramamurthy, 2006). The modified foam concrete mix design equations are described in the following equations.

$$\rho_t = c \cdot [\alpha + \beta] + RD_f \cdot V_f \tag{3.6}$$

$$1 = c \cdot [\beta + \gamma] + V_f \tag{3.7}$$

where

$$\alpha = 1 + (CSA/c) + (a/c) + (s/c) + (sf/c) + (nS/c)$$

$$\beta = (w/CSA)(CSA/c) + (w/a)(a/c) + (w/s)(s/c) + (w/sf)(sf/c) + (w/nS)(nS/c)$$

$$\gamma = \frac{1}{RD_c} + \frac{(CSA/c)}{RD_{CSA}} + \frac{(a/c)}{RD_a} + \frac{(s/c)}{RD_s} + \frac{(sf/c)}{RD_{sf}} + \frac{(nS/c)}{RD_{nS}}$$

To establish the two primary variables, *c* and V_f, the water demand and proportion to cement content of each dry material need to be predetermined. The water demand determination can be performed by an adapted ASTM C1437 flowtable test (2015) according to (Kearsley & Mostert, 2005). As the strength of foamed concrete is dominantly influenced by the void fraction, the consistency of foamed concrete is the main benchmark parameter for determining the water demands of the dry constituents. The water demand of each dry constituent can be determined by a sensitivity analysis approach until the mixture of water and dry material has a 220 mm flow table spread diameter after 15 strokes. It is noted that

some dry materials are not pozzolanic or cementitious, so cement is added to those materials for the process of determining their water demand. It must be mentioned that the water-to-cement and water-to-fly ash ratios are not below 0.3 and 0.25 respectively from literature (Kearsley & Mostert, 2005).

In the mix design, CSA cement was introduced since the partial CSA substitution in LWFC was found to improve foam stability by rapid early strength development (Jones *et al.*, 2016). The rapid hardening property is attributed to a high ye'elimite (C_4A_3S) content in sulfoaluminate belite and ferrialuminate clinkers which produces excessive and rapid ettringite formation (Mose & Perumal, 2016). The property is expected to improve the thixotropy rate, and thereby also the constructability of 3DP-LWFC.

The selected cement contains 6 – 20% limestone extenders and is classified as CEM II/A-L 52.5N. The locally sourced fly ash, called Durapozz, is categorised as class F. Both conform to SANS 50197-1 (2013). Nano silicon dioxide (nS) powder with an average particle size of 30 ± 5 nm was selected as extender together with Chryso densified silica fume. Graded silica sand was used as an inert material and has a maximum particle size of 0.5 mm. High aluminate content CSA cement (type III) manufactured by Royal White Cement (RWC) is added in a fixed CSA-to-cement ratio of 10%. The synthetic fibre type for fibre reinforcement is 6 mm long polypropylene (PP) fibre. A summarised water demand and proportion to cement content are presented in Table 3.1, and chemical and physical constituents are summarised in Table 3.2 and Table 3.3 respectively.

Table 3.1 Water demand (w/x) and proportions to cement content (x/c) for 3DP-LWFC mix design

Materials	Cement	CSA	Fly ash	Sand	Silica fume	Nano silica	PP fibre
w/x	0.375	0.375	Variable*	0.08	0.71	0.84	**0.4% of total mix volume
x/c	1.0	0.1	1.0	0.2	0.1	0.02	

* Minimum w/a ratio 0.25 according to (Kearsley & Mostert, 2005)
**No added water for fibre

Table 3.2 Chemical composition (in mass percentages) of pozzolanic materials

	SiO_2	Al_2O_3	Fe_2O_3	CaO	MgO	K_2O	Na_2O	TiO_2	SO_3
Cement	21.5	5.5	3	65.5	2.0	<0.5	<0.5	-	1.5
CSA	10.5	34	2.5	42.5	3.5	-	-	1.5	8.5
Fly ash	54.1	31.8	3.2	4.9	1.2	0.8	0.2	1.7	-
Silica Fume	99.5	<0.1	<0.1	<0.1	<0.1	-	-	-	-

Table 3.3 Physical properties of the dry constituents, with ρ the specific gravity and SA the specific surface area

Materials	OPC	CSA	Fly ash	Silica Fume	Nano SiO_2	Sand	PP fibre
γ (-)	3.15	3.1	2.2	2.9	2.17	2.65	0.91
SA ($m^2\,kg^{-1}$)	400	480	300 - 400	13 000 – 20 000	200 000	97.9	

Table 3.4 Mix designs (units are in kg/m^3 except for *w/a* ratio)

	BM180	BM180CSA	BM200	BM220	TD-7	TD-10	TD-14
w/a	0.25	0.28	0.32	0.35	0.33	0.30	0.28
Cement	452.8	429.3	443.0	438.9	199.5	297.9	429.3
Fly ash	452.8	429.3	443.0	438.9	199.5	297.9	429.3
CSA	-	42.9	-	-	20.0	29.8	42.9
Silica fume	45.3	42.9	44.3	43.9	20.0	29.8	42.9
Sand	90.6	85.9	88.6	87.8	39.9	59.6	85.9
nSiO2	9.1	8.6	8.9	8.8	4.0	6.0	8.6
Water	330.0	341.8	353.8	363.7	168.8	243.2	341.8
Foam	19.6	19.3	18.5	18.0	48.4	35.9	19.3

*PP fibres are constantly added of 4.1 kg/m^3 (0.45% of the mixture volume)

A protein-based foaming agent is diluted by a 1:40 ratio with water and mixed with ferrous sulphate in a ratio 1:80 ratio with water mass is fused as a foam stabiliser. The solution undergoes mechanical agitation with a flow rate of 1 – 3 litres per second and air pressure of 50 – 60 kPa to generate precursor aqueous foam, with a controlled density of 75 ± 5 kg/m^3, according to the specification of the manufacturer. It is assumed that the generated foam is in a metastable phase to minimise the complexity of the foam stability study. It is worthwhile to mention that the type and/or concentration of surfactant highly affects the mechanical properties of the thin film, which is the main factor for the foam stability, yet a constant type and concentration of surfactant is used throughout the current study.

The foam stability assessment in this study is divided into two stages, considering: 1) the influence of rheology of the base mix without the pumping process and 2) the influence of a continuous and dynamic disturbance from the pump pressure to LWFC with target densities, 700, 1000 and 1400 kg/m^3, produced with the selected optimal base mix from the first stage.

It is known that the lower bound of slump flow for stable conventional LWFC is 220 mm, but it is worthwhile to investigate the foam stability in less flowable base mixes, i.e. smaller slump flow, to secure some degree of buildability for LWFC. In the first stage, three base mix designs with different slump flow by varying w/a ratio were prepared, namely 220 mm, 200 mm, and 180 mm allowing ±5 mm tolerance of each. These samples are denoted BM220, BM200, and BM180. Additionally, another base mix with CSA cement was designed, denoted BM180CSA, to accelerate the yield stress evolution rate, and the slump flow of the fourth sample to agree with the smallest slump flow of the three, i.e. 180 mm.

A stable and optimal base mix design for the constructability of a digital construction application was selected for the following stage. The final test set comprises of 3DP-LWFCs with target densities of 700, 1000 and 1400 kg/m^3, named TD-7, TD-10, and TD-14, respectively. This test set was subjected

to a pump process to assess the foam stability under a high-pressure environment. The complete set of mix designs can be found in Table 3.4.

3.3.2 Foam concrete stability test

3.3.2.1 Static foam stability

No standardised foam stability test is available up-to-date, but several researchers perform gravimetric or volumetric measurement for stability studies (Dhasindrakrishna *et al.*, 2020; Jones *et al.*, 2016; She, 2018).

Since the densification of LWFC occurs by the gravity-driven solid particle migration of surrounding paste into the position of the disappeared bubble if an unstable bubble breaks, the densities at different stages should be recorded on regular basis throughout the mixing and casting process. Density is measured by casting a 1 L sample into a known weight 100 mm cube mould, and weighing the captured sample. The measured weight with a unit volume is converted into the density and results in the following parameters: ρ_{base} – base mix density, ρ_{wet} – the wet density of LWFC that is measured as soon as a homogeneous LWFC is produced in the fresh state, and ρ_{mature} – the density obtained from 7-day aged sample kept in controlled air curing conditions (23±2°C and 65±5% RH). The parameters allow the determination of porosity parameters suggested by several researchers presented in Table 3.5 which indicates the stably captured foam volume as well as the void fraction after the final setting of the concrete.

Primarily, the measured wet density of LWFC is checked for the foam stability whether it falls within the tolerance of ±50 kg/m^3 from the desired target wet density (Kearsley & Mostert, 2005; Wei *et al.*, 2013). Since the mature specimen may exhibit a notable degree of volumetric shrinkage during hydration which invalidates the density conversion, the volumetric change can be recorded by measuring the average dimensional change, at the midpoint of each side of the cube to determine.

The subsequent foam stability test is conducted by comparing the wet density and the mature density. This comparison can tell whether the entrained bubbles are secured in the surrounding mortar mix during the hydration process without a significant water loss released from the ruptured bubble film other than the added mix water. Several empirical correlations between mature and wet density can be found in Table 3.6, and those will be compared with the obtained actual results.

Table 3.5 Various porosity calculation

Reference	Porosity equation	Remarks
Wei et al. (2013)	$n = 1 - \frac{\rho_{mature}}{\rho_{base}}$	
Hoff[1] (1972)	$n_t = 1 - \frac{\rho_{wet}(1 + 0.20\gamma_c)}{(1 + k)\gamma_c \rho_w}$	n_t = theoretical porosity γ_c = specific weight of cement k = water/cement ratio by weight ρ_w = density of water
Nambiar et al.[2] (2008)	$n_t = 1 - \frac{\rho_{wet}(1 + 0.20\gamma_c + s_v)}{(1 + k_s)(1 + s_w)\gamma_c \rho_w}$	s_v = filler/cement ratio by weight s_w = filler/cement ratio by volume k_s = water/solids ratio by weight

[1] Theoretical porosity calculation by assuming 20% hydration bound
[2] Expanded equation to account for filler (such as fly ash, sand, etc.)

Table 3.6 Empirical correlation between the mature and wet density of LWFC

Reference	Model equation	Remarks
Wei et al. (2013)	$\rho_{mature} = 1.000\rho_{wet} - 42.947$	Studied density: 300 – 1900 kg/m^3
Falliano et al. (2018)	$\rho_{mature} = 0.809\rho_{wet} + 27.624$	Studied density: 400 – 1000 kg/m^3

3.3.2.2 Dynamic foam stability

External dynamic loading is imposed on LWFC through two types of pressurizing mechanisms, namely 3DCP pumping pressure and negative vacuum pressure, in the second stage of the experimental work. Assuming foam stability of tested samples as discussed in Section 3.3.2.1 is secured, the comparison of pre- and post-pumped densities is the primary work in this section. The wet and mature post-pumped densities are denoted $\rho_{wet.pump}$ and $\rho_{mature\ pump}$ according to the age at the density measurement.

A laboratory-scale gantry 3D concrete printer with a build volume of approximately 1 cubic metre is located in Stellenbosch University (Cho *et al.*, 2019). The 3D concrete printer is paired with a three-phase 380V 3kW progressive cavity concrete pump allowing a maximum aggregate size of 4 mm. On variable frequency drive (VFD) augmentation, the rotary speed can be varied, i.e. material feed speed. The 3D concrete printer setup and pump detail with components are presented in Fig. 3.2.

Since the foam stability of LWFC for additive manufacturing application is of particular interest in this study, the density alteration resulting from the actual 3D concrete printer setup is a crucial parameter to replicate the 3DCP situation. Freshly prepared LWFC is placed in the hopper of the pump, and the

material is transported through the 25-mm diameter sized hose. The end nozzle is lifted to 150 mm in height to catch the post-pumped material. The density of the post-pumped LWFC is captured at various feed durations to track the evolution of density change over time.

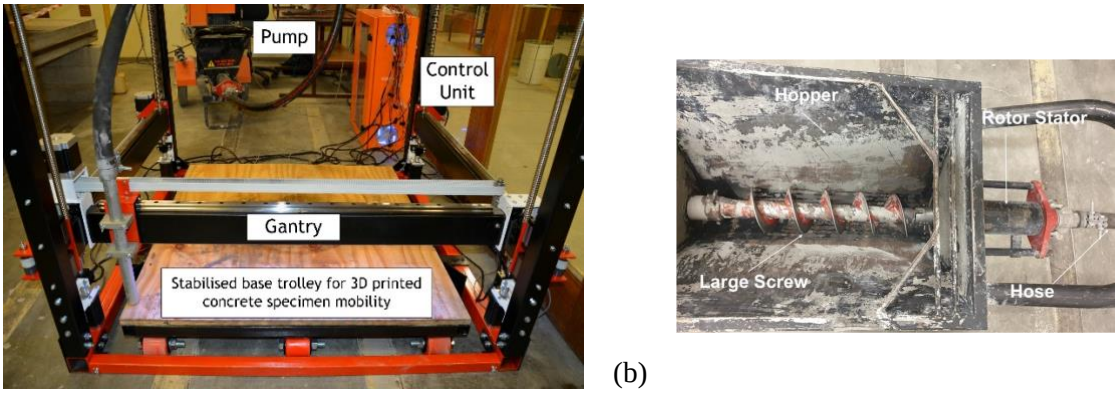

(a) (b)

Fig. 3.2 (a) 3D concrete printer setup situated in Stellenbosch University (Cho *et al.*, 2019); (b) Rockcrete TSL progressive cavity pump indicating the rotor-stator, hopper, hose and large screw (Kruger *et al.*, 2019)

Since no pressure gauge or meter is fitted to the abovementioned concrete pump, the applied pump pressure cannot be determined. Thus, a constant pressure box test was conducted. The freshly prepared mixture was placed in a container with a size of 150 mm (*W*) x 150 mm (*L*) x 50 mm (*H*) and sealed to be air-tight as indicated in Fig. 3.3. A suction pump with a pressure gauge was connected to the container. The pump produced a controlled negative pressure up to 80 kPa which is close to vacuum pressure. The constant pressure was removed after 15 minutes.

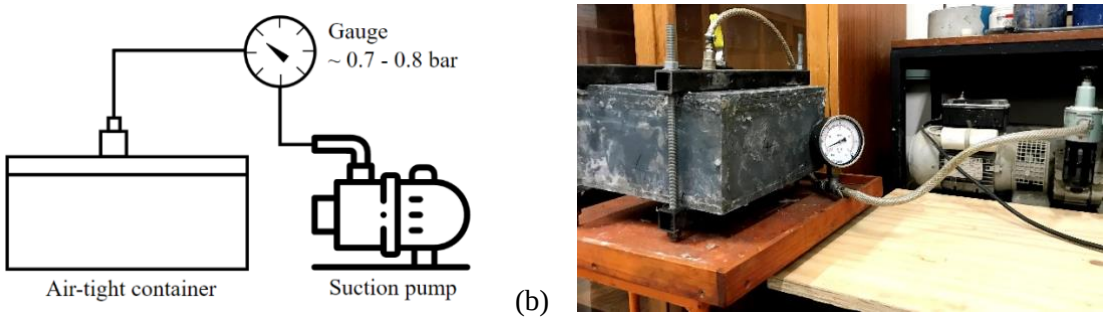

(a) (b)

Fig. 3.3 (a) schematisation of the experimental setup; (b) actual setup for a constant pressure box

3.3.3 Rheometer measurement

The fundamental rheological property of the base mix is characterised by a rotational concrete rheometer manufactured by the International Centre for Aggregate Research (ICAR). The rheometer is composed of a 20-L high-quality stainless-steel container, a driver head with a torque range of 0.01 – 20 N.m and rotational speed range of 0.01 – 0.60 rps, and a four-blade vane welded to a concentric shaft. An anti-slippage mechanism is provided along the container wall by a series of equally spaced vertical strips.

Constant Shear Rate (CSR) testing was performed by conducting the stress growth test over a single batch for 60 s which measures the torque values over time and automatically selects the maximum torque measured during the test. The maximum torque value was converted into static yield stress by using the following equation:

$$\tau_{st} = \frac{2T}{\pi D^3 \left(\frac{H}{D} + \frac{1}{3}\right)} \tag{3.8}$$

where T is measured torque (N.m), D is the vane diameter (m), and H is the vane height (m).

The post-peak stress growth plot tends to reduce and converge to a constant torque value after the initial peak. The converged value was converted into shear stress using Eq. 3.8, and this stress is referred to as the dynamic yield stress, denoted as τ_{dyn}.

A time-dependent rheological parameter, thixotropy, is also a crucial property in the rheological performance of cementitious material. Kruger et al. (2019) proposed a bi-linear thixotropy model, modifying a linear structuration rate thixotropic model developed by Roussel (2006) to distinguish between re-flocculation rate (R_{thix}) and the structuration rate (A_{thix}).

The modified thixotropy model can be obtained by a series of CSR tests with an incremented resting time gap. To simulate the pumping agitation of the particular 3D concrete printer used for this research, a constant rotational vane speed of 0.2 rps was applied, which is equivalent to a shear rate ($\dot{\gamma}$) of 1.0 s^{-1}. The resting time gap series comprised of 0, 10, 20, and 30-minute intervals. From the set of test results, the thixotropic parameters, R_{thix} and A_{thix}, can be calculated using the following equation:

$$\tau(t) = \begin{cases} \tau_{D,i} + R_{thix} \cdot t & t \leq t_{rf} \\ \tau_{S,i} + A_{thix} \cdot \left(t_{rf} - t\right) & t > t_{rf} \end{cases} \tag{3.9}$$

where $\tau_{D,i}$ is initial dynamic yield stress, $\tau_{S,i}$ is initial static yield stress, and t_{rf} is re-flocculation time defined as $t_{rf} = (\tau_{S,i} - \tau_{D,i})/R_{thix}$.

Furthermore, the Bingham parameters, dynamic yield stress (τ_{dyn}) and plastic viscosity (μ_p), were determined by a flow curve test. To obtain an accurate result, a breakdown pre-shear was imposed at a 2.5 s^{-1} shear rate for 20 s. After the initial breakdown, the shear stresses were measured at 7 equally divided shear rate steps in descending order between the initial shear rate of 2.5 s^{-1} and the final shear rate of 0.25 s^{-1} for 5 s at each step. The measured dynamic yield stress, plastic viscosity and R-squared are reported.

3.3.4 Void structure analysis

Before and after extruded samples of TD-7, TD-10 and TD-14 were cast into cylindrical hollow 3D printed polylactic acid (common term, PLA) moulds with 20-mm inner diameter, 40-mm height and 0.4 mm wall thickness. It is noted that the PLA moulds were 3D printed with 0.15 mm layer height, 0.4

mm nozzle diameter, 50 mm/s print speed, 200°C nozzle temperature and 40°C bed temperature. The cast samples were stored for 7 days in the same air curing condition specified in Section 3.3.2.1.

Hardened samples, without removing PLA moulds, were subjected to X-ray computed tomography (CT) scan at the Stellenbosch CT Scanner Facility (du Plessis *et al.*, 2016), using a General Electric VTomeX L240 system. The scans were done at 160 kV, 150µA and 25 µm voxel size with copper beam filtration of 0.1 mm to reduce beam hardening artefacts. The 2400 images, recorded during one 360-degree rotation of the sample, were acquired at 500 ms per image and 2000 rotation steps. The detailed procedure can be found in du Plessis *et al.* (2016). Visualization and analysis were performed with Volume Graphics VGStudioMax 3.4, as can be seen in Fig. 3.4. The software package allows for defect analysis, allowing assessment of the average porosity and pore counts, and foam structure analysis, providing pore size distribution and air void size characterisation along with the height.

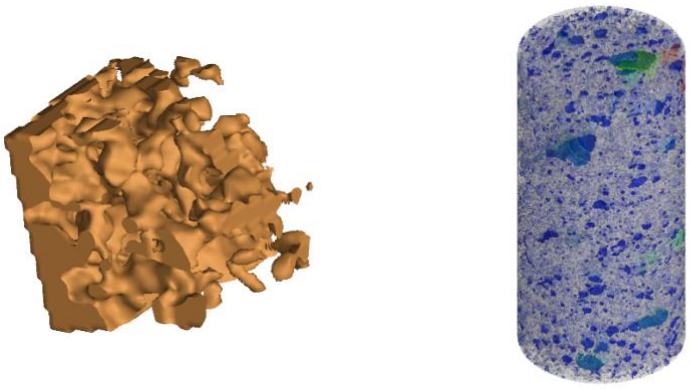

(a) (b)

Fig. 3.4 X-ray tomography scanned foamed concrete. (a) 3D visualised image for defect analysis; (b) foam structure analysis outcome

3.4 Results and Discussion

3.4.1 Foam concrete stability test

Before the stability test, the actual incorporated foam volume for each 10-litre batch of LWFC mix was recorded for BM220, BM200, BM180, and BM180CSA based on sensitivity analysis. Once the base mix is prepared, 50 – 80% of foam (by mass) is added according to the mix design – no foam breakdown occurrence situation. In the density check, the mixture is accepted if it is within the tolerance, i.e. ±50 kg/m^3 of target density. In case the density is lower than the tolerance, the mixture is discarded while more foam is added when the density is higher than the tolerance. The process is iterated until the mixture is acceptable and the recorded foam volume is plotted in Fig. 3.5 (a).

Due to the tolerance, the measured foam amounts of each mixture are linearly normalised by the density offset to the target density. The result shows TD-14 is the most sensitive sample to the fluidity of the base mix by presenting a steep gradient in the trendline, while TD-7 and TD-10 have relatively flattened

gradients. The ranges of added foam volume are 4.58 – 5.23 L for TD-7, 3.54 – 3.90 L for TD-10, and 1.59 – 3.53 L for TD-14 per each 10 L batch. It must be clarified that the amount of foam volume incorporated into the LWFC mixture is not necessarily equivalent or analogous to the actual foam fraction of LWFC since the incorporated foam is partially degraded when mixed by several factors.

The degraded foam volume increase when it is mixed with a stiffer base mix with a higher static yield stress and viscosity in which the dissipating potential energy is higher, particularly in a dynamic environment such as when cement particles migrate for the foam insertion. When the energy transferred to the bubble exceeds a threshold, breaching the ultimate strength of the film, the bubble rupture propagates, and it leads to failure of the bubble.

Moreover, the stiffer base mix has low fluidity, containing a higher volume of unsaturated cement grains. The unsaturated cement grains have better wettability, smaller contact angle due to the hydrophilicity and greater total surface free energy which attracts a greater number of water molecules for adsorption (Klein *et al.*, 2012). In other words, stronger attachment is expected for a higher surface energy solid grain, e.g. unsaturated cement grain, due to hydrogen bonds and van der Waals forces. At the contact between the unsaturated cement grain and a thin film with low free water condition, the unsaturated cement grain is thus postulated to withdraw liquid on or from the bubble film surface due to the high surface free energy. Moreover, the smaller contact angle promotes capillary pressure at contact (Butt *et al.*, 2003), which leads to further bubble film thinning process.

When the bubble film ruptures, in general, the liquid inside of the bubble film is released, and it increases the liquid fraction of the bulk material. As the fluidity of the bulk material increases, the strain energy of the cementitious bulk material is lowered until it reaches the ultimate strength of the bubble film, which can be called *ideal fluidity*, allowing eased placement and dispersion of foam into the bulk material without major degradation. This mechanism is argued to be the reason behind the inversely proportional relation between foam volume addition and slump flow of TD-14 in Fig. 3.5 (a).

The actual foam volumes of each dataset are compared with the foam volume of the calculated mix design based on Eqs. (3.6) and (3.7), depicted in Fig. 3.5 (b), to show how much more or less foam volume is added to match target density than the theoretically required foam volume. The result shows that TD-14 solely requires extra amounts of foam, as high as +59.6%, to match the target density. The required foam volume of TD-14, where the foam volume fraction $\phi_{foam,TD-14}$ is 19.8 to 22.1%, is remarkably lower than TD-7, where $\phi_{foam,TD-7}$ is 62.5 to 63.0%, according to the theoretical calculation. Even though the stiffness of base mix and the amount of foam volume used to reach the *ideal fluidity* are identical for the different target densities, the foam volume of TD-14 that 'survived' may likely be insufficient to bring the density down by the remained bubbles. This can be validated by considering the TD-14 sample with higher fluidity which shows close to zero or less foam volume required to match the target density.

The negative offset values, especially for TD-7 and TD-10, can be explained by the foam density and base mix density fluctuation. As discussed in Section 3.3.1, there is a range for the foam density (70 – 80 kg/m^3) because the physical properties of foam can be altered depending on the production condition even though it is controlled. Moreover, the base mix density does not always match the one from the calculated mix design. The required foam volume from the mix design is, however, calculated based on the constant foam density and base mix density. It should be mentioned that the dataset presented in Fig. 3.5 represents the results based on the 10 L LWFC batch, and the linear scalability for the larger volume has not been validated.

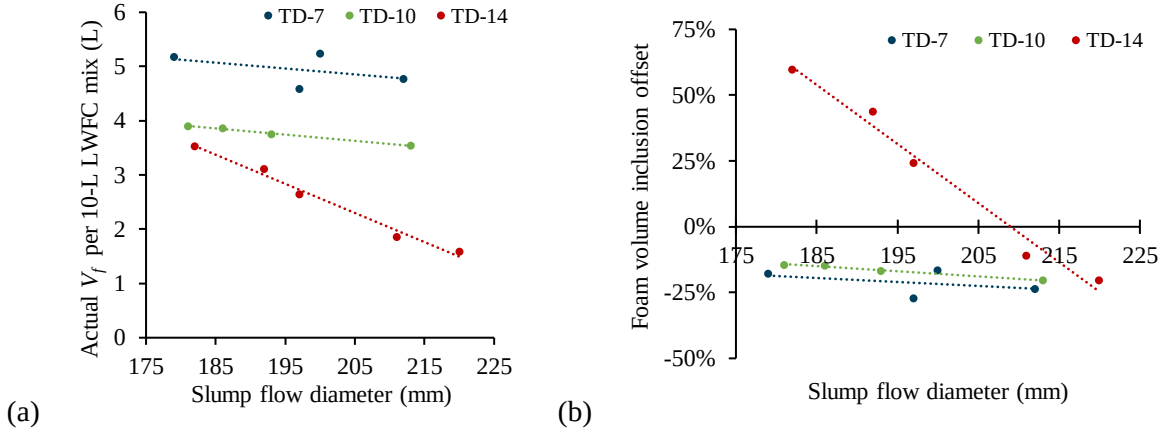

Fig. 3.5 (a) Actual incorporated foam volume for 10-L LWFC batch with fluidity variation in the base mix; (b) Foam volume offset to the required foam volume in mix design with fluidity variation in the base mix

3.4.1.1 Stability under normal condition

Based on the observation above, various LWFC mixes, namely BM180, BM180CSA, BM200 and BM220, were prepared to investigate the stability through mature and wet density comparison and porosity. The design wet target density of the sample was set to be 700 kg/m^3 since it is generally more difficult to secure the stability for LWFC with lower density. Table 3.7 presents the actual wet and dry density for various base mix designs.

The result shows the wet densities of all the samples fall within the tolerable region to the target density, i.e. 650 – 750 kg/m^3. While BM180CSA shows the highest density reduction, which is -48.9 kg/m^3 or -6.9%, no significant defect or volumetric instability was found in the dry specimens by observation.

Table 3.7 also shows computed mature densities based on the various empirical models calculated by the actual wet density, and Fig. 3.6 (a) shows the mature-to-wet density ratios. The model of Wei et al. presents the closest trends over the samples in which there is only a limited discrepancy (< 12%) with Falliano's model. Fig. 3.6 (b) presents the empirical correlation between the mature and wet density obtained in this study. By assuming the sample volume remained unchanged, the mass reductions are seemingly in a reasonable range by the comparison. This result supports the security of foam stability

within a stiff base mix and the compatibility of CSA cement in LWFC, thus BM180CSA was selected for the upcoming study, considering foam stability and printability.

Table 3.7 Actual wet and mature densities (Units are in kg/m^3)

Sample	Actual ρ_{wet}	Actual ρ_{mature}	Wei et al. ρ_{mature}	Falliano et al. ρ_{mature}
BM180CSA	704.8	655.9	661.9	597.8
BM180	691.3	670.7	648.4	586.9
BM200	681.8	655.3	638.8	579.2
BM220	694.8	666.3	651.8	589.7

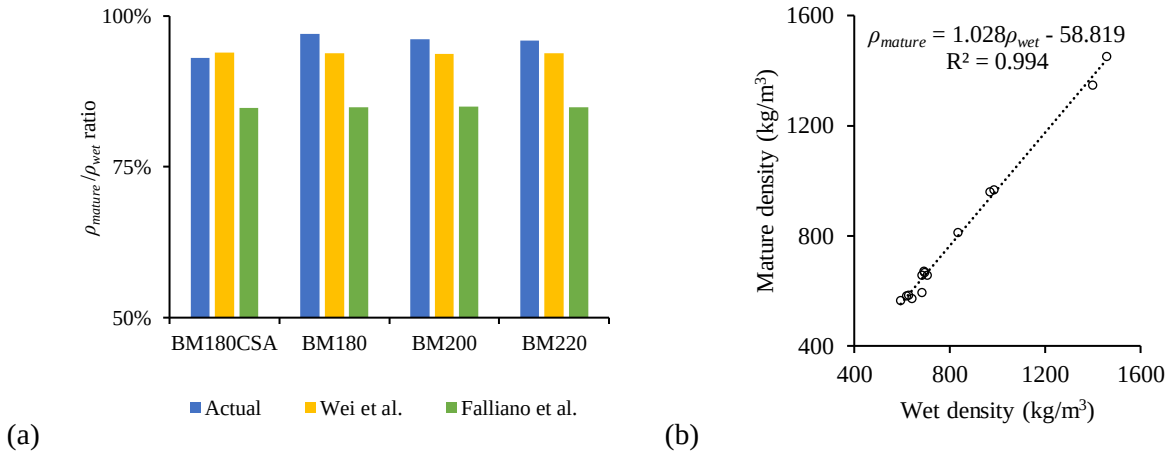

Fig. 3.6 (a) Mature-to-wet density ratio comparison with various empirical model (b) correlation between actual mature and actual wet density

With the selected base mix, various LWFC samples with different target densities were prepared and the physical property of LWFC results are summarised in Table 3.8. Comparing the wet density measured in the fresh state with wet target density is an initial stability check, and all the samples were within an acceptable density range. Volumetric changes during the setting period are shown in Table 3.8. It is worthwhile to mention the centre of the casting surface tends to bulge even after levelling with a trowel, which may contribute to the positive dimensional change where concrete, in general, shrinks with time. Overall, the density conversion from the casted cube specimen is valid as the volumetric changes seem to be insignificant.

Various measured and theoretical porosities are shown in Table 3.8. For Nambiar et al.'s theoretical porosity model, fly ash, silica fume, nano-silica, and fine sands are considered as a filler as per the literature (Nambiar & Ramamurthy, 2008). Since Hoff's model only considers cement, water and foam, other constituents are completely ignored which leads to an imbalance of total volume and mass. While the theoretical porosities calculated with the equations proposed by Hoff and Nambiar et al. are similar

to each other, they are significantly higher than the porosity model proposed by Wei et al, with the difference increasing as the target density increases. These parameters are further discussed with measured porosity from the void structure analysis results in Section 3.4.3.

Fig. 3.7 shows the comparison between the actual mature-to-wet density ratio and the ratio computed based on various empirical models. Providing volumetric stability of the specimen, there is no notable mass reduction between the casting and mature densities. Based on the discussed results and observations, it seems that the slump flow diameter region of the base mixture should be in a range of 185 – 195 mm for better foam stability and printability in 3DCP applications.

Table 3.8 Physical properties of fresh and hardened state LWFC with different target densities (Coefficient of variations are defined in the bracket)

	ρ_{base} (kg/m^3)	ρ_{wet} (kg/m^3)	ρ_{mature} (kg/m^3)	Wei et al. n (%)	Hoff n (%)	Nambiar et al. n (%)	dV (%)
TD-7	1796.0	704.8 (1.95)	655.9 (1.98)	63.5	73.0	73.3	-0.63
TD-10	1776.0	967.3 (2.98)	958.6 (2.46)	46.0	62.9	63.1	+0.79
TD-14	1784.0	1397.8 (1.15)	1346.0 (1.27)	24.6	46.4	46.3	-0.36

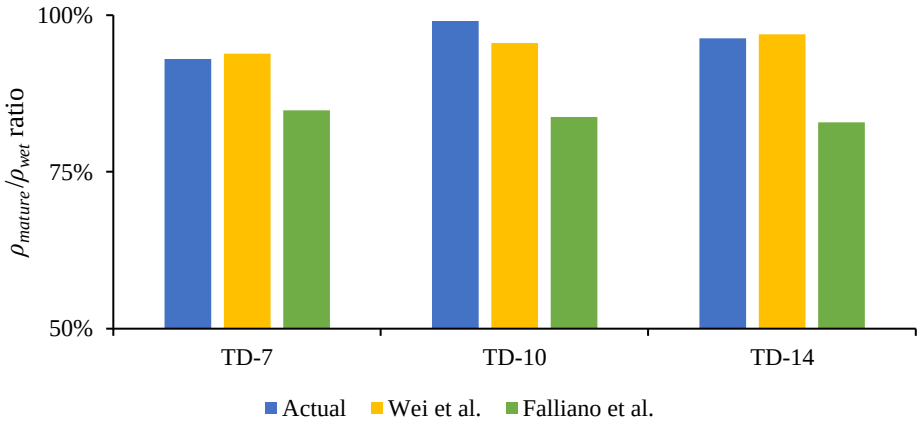

Fig. 3.7 Mature-to-wet density ratio of various empirical models

3.4.1.2 Stability under external pressure

Providing foam stability of LWFC with a wide density range in a static condition, foam stability under high pressure has been investigated with the concrete pump used for the 3D concrete printer. Pre-pressure (ρ_{wet}) and post-pressure density ($\rho_{wet.pump}$) measurements are presented in Fig. 3.8 (a) – (c) for TD-7, TD-10, and TD-14, respectively. Solid lines represent ρ_{wet} measured from the mixing container when fresh LWFC material is prepared. $\rho_{wet.pump}$'s are shown as dots in the figure while three different timings for the sample capturing are considered for better representability in the continuous pumping process of 3DCP. Dashed lines indicate the upper/lower boundaries of the tolerance to the target density.

The results show that TD-7 is the most stable sample under pumping pressure condition by showing only a subtle difference in density with pumping duration, and all densities are within the tolerance boundaries. It may be contributed by the "cushioning effect" impeding the intensity of external disturbance which is more prominent in bulk material with higher foam volume fraction (Zeng *et al.*, 2020). While foam stability is shown in the pre-pressure density of TD-14, the post-pressure densities are unacceptable, even for the initial post-pressure density. In most concrete pumping processes, the lubricating layer is formed between the pipe wall and the bulk material. The yield stress and plastic viscosity of the lubrication layers are considered as about one fifth and one-fifteenth of the bulk material, respectively (Mechtcherine *et al.*, 2020). Since the rheological properties and the thickness of the lubrication layer are inherited by the parental material, the lubrication layer of TD-14 is expected to have higher yield stress and plastic viscosity which has higher solid concentration leading to higher rheological parameters (Choi *et al.*, 2013). This results in the build-up of higher internal stress than TD-7 which can be a cause of foam instability for TD-14. The pre-pressure density, as well as the initial post-pressure density of TD-10, are acceptable, even though the following post-pressure densities have rapidly increased density, which is outside the tolerance. In this case, a continuous concrete mixer can be a remedy.

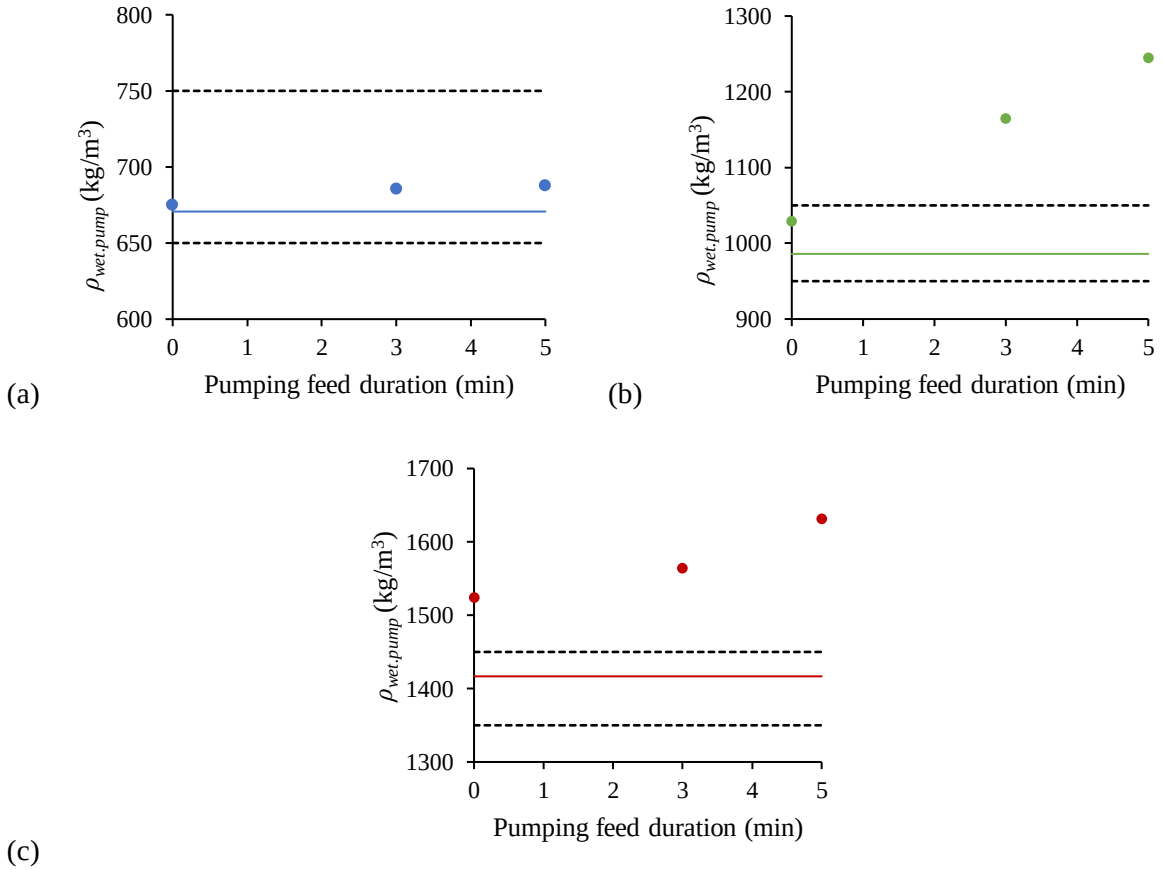

Fig. 3.8 Foam stability check under pumping pressure. ρ_{wet} – solid line and $\rho_{wet.pump}$ – three dots for (a) TD-7, (b) TD-10, and (c) TD-14

During the 3D printing, process material is also subjected to negative pressures and thus the samples were also subjected to negative pressure, i.e. creating vacuum condition by sucking air, and investigated for the density changes. The results are shown in Table 3.9. This investigation showed a lesser degree of change in density than the previous pumping experiment, however, it agrees with the tendency of the abovementioned results in which higher target density LWFC loses more void fraction, leading to density increase. Table 3.9 shows the density alteration over pre- and post-pressure densities of TD-7, TD-10 and TD-14. It must be mentioned all presented densities in this section are wet densities.

From the observation above, the rheology of bulk material is one of the key factors for foam stability, in particular, under the pumping pressure condition. Hence, it is recommended that, if the foamed concrete is designed to be pumped, the rheology of TD-14 should be adapted by adjusting the water-to-solid ratio to reduce the solid concentration.

Table 3.9 Gravimetric measurement of LWFC under negative pressure environment. (Coefficient of variations are defined in the bracket)

	TD-7	TD-10	TD-14
Pre-pressure density (kg/m^3)	670.7 (1.57)	967.3 (0.29)	1410.2 (0.69)
Post-pressure density (kg/m^3)	694.4 (4.44)	1002.5 (1.87)	1484.7 (1.46)

3.4.2 Fresh state characterisation of base mix

This section reports rheometer results of the base mixes for the different slump flow discussed in previous sections. Table 3.10 summarizes initial static and dynamic yield stresses, re-flocculation rate, structuration rate, plastic viscosity and kinematic viscosity of BM180, BM180CSA, BM200 and BM220. A series of stress growth curves for the samples can be found in Fig. 3.9 (a) showing inversely correlated relationships between slump flow and yield stress, and the flow curve is presented in Fig. 3.9 (b) showing similar trends to the stress growth curve results except for BM180CSA. Even though time-dependent thixotropy parameters (R_{thix} and A_{thix}) are not of particular interest in this study since the base mix is immediately mixed with foam during LWFC production, this still shows outstandingly improved thixotropic behaviour of mixture containing CSA cement. Thus, it is believed the inclusion of CSA cement promotes the printability of LWFC.

The plastic and kinematic viscosities of the sample are plotted in Fig. 3.9 (c). Kinematic viscosity is the normalised parameter of plastic viscosity by the density when comparing the flow behaviour of each sample. It is hard to explain the both of plastic and kinematic viscosity reduction in BM180CSA compared to BM180 having the same slump flow values, or stiffness since CSA inclusion normally increases the viscosity of the bulk material according to (Chen *et al.*, 2018; Ke *et al.*, 2020). This may

be because of the single batch for the rheometer test only. Thus, repetition is encouraged for better representation.

Table 3.10 Rheological characterisation of base mixes with different slump flows

Sample	S[a] (mm)	$\tau_{S,i}$ [b] (Pa)	$\tau_{D,i}$ [c] (Pa)	R_{thix} (Pa/s)	A_{thix} (Pa/s)	μ[d] (Pa.s)	ν[e] (m^2/s)
BM220	221.5	160.4	128.2	Not measured	Not measured	0.5	0.00030
BM200	195	396.0	335.8	0.101	0.026	1.6	0.00093
BM180	180	991.8	759.4	0.138	0.157	2.5	0.00138
BM180CSA	180	1376.0	980.5	0.692	2.12	1.8	0.00100

[a]Slump flow; [b]Initial static yield stress; [c]Initial dynamic yield stress; [d] Plastic viscosity; [e]Kinematic viscosity

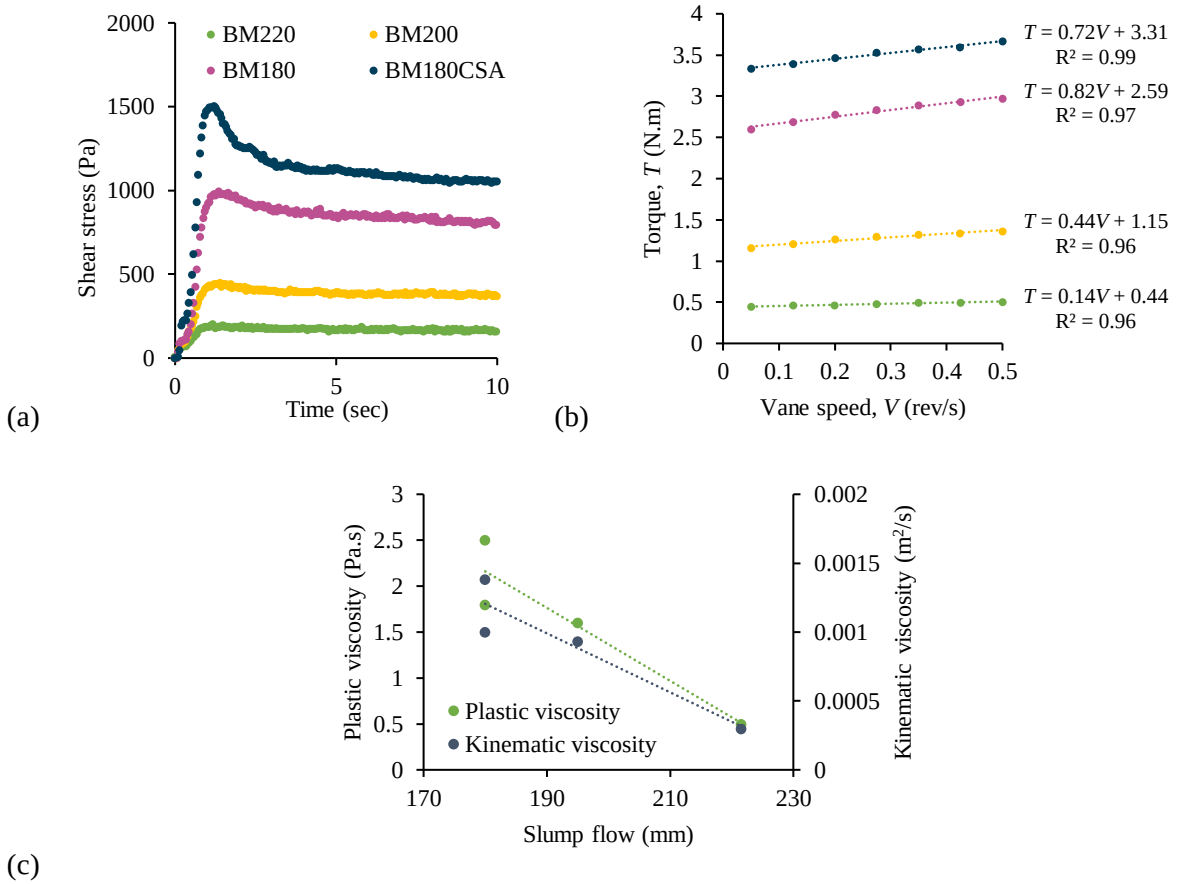

Fig. 3.9 (a) stress growth test results; (b) flow curve test results; (c) plastic and kinematic viscosity of various slump flows

Feneuil et al. (2019) presented critical yield stress values depending on the bubble size which causes drainage and ripening destabilisation mechanisms in cement foam. Once the yield stress of bulk material exceeds the critical yield stress, the bulk material captures the movement of bubbles and no or negligible

drainage and ripening may occur. For bubbles with a diameter of 100µm and surface tension of 30mN/m, as presented in the study, the critical yield stress where ripening is the dominant destabilisation mechanism is calculated to be 300 Pa.

Thus, the assumption of no ripening and drainage is valid for BM200, BM180 and BM180CSA, and it can be seen that coalescence is the dominant destabilisation mechanism. The same study also mentioned coalescence that film breakage may occur even when the capillary pressure does not exceed disjoining pressure due to dynamics during bubble rearrangement. It is, therefore, hypothesised that the highly stiff mortar having high yield stress, like the studied base mixes, leads to significant coalescence by the combination of large capillary pressure and kinetic energy.

3.4.3 Void structure analysis

Cross-sectional images produced by three-dimensional X-CT scans of samples are shown in Fig. 3.10. These images were used to calculate the mean void fraction in each sample, and the result is shown in Table 3.11. The table also contains the mean sphericity of each scanned sample. The result shows porosity reduction in each target density in the post-pump samples, which is directly linked to the density increase discussed in Section 3.4.1. It is not easy to assess the foam stability by the obtained porosity directly, however, the TD-10 post-pump sample is deemed to have foam instability due to the significant porosity reduction compared to the other samples.

The measured pre- and post-pumped porosities are compared with the porosity models discussed in Section 3.3.2.1. The calculated porosity and theoretical porosities are plotted against the measured pre- and post-pumped porosity which can be found in Fig. 3.11, with the unity line as a dotted line. Theoretical porosities still show the largest discrepancy to the measured porosities while the computed porosity proposed by Wei et al. is close to the unity line for the pre-pumped porosity. However, the latter model also shows the deviation in the plot against post-pumped porosity. The inconsistency is due to the porosity drop through the pumping process while the computed porosities remained unchanged.

It is postulated that the material transport procedure through the pump pipe lowers the sphericity by confinement as reported in the literature (Kruger *et al.*, 2021). This is however not true for TD 7, where the sphericity increased as a result of pumping. These results seem to indicate that the low density foamed concrete would be perfectly suited for 3D printing, as the quality of the voids in the cement improves when pumping takes place.

Fig. 3.12 presents pore size-frequency distributions of pre- and post-pumped LWFC samples with different target densities. All distributions are significantly skewed to the right, meaning smaller pore diameter/size, mainly 100 – 400 µm in diameter, are dominant in the matrix. Post-pump TD-7 and TD-10 samples contain slightly smaller sized pores than pre-pump samples, while only negligible change is found in TD-14 samples. Bubble size is highly dependant on applied pressure to the bubble. Since

post-pump samples have experienced extra pumping pressure, the higher smaller sized pore fraction is expected to be higher than in the pre-pump sample.

Table 3.11 Mean porosity and sphericity results from XCT analysis

		TD-7	TD-10	TD-14
Porosity	Pre-pump	52.77%	33.62%	19.94%
	Post-pump	52.31%	22.20%	16.07%
Sphericity	Pre-pump	0.596	0.619	0.544
	Post-pump	0.604	0.535	0.536

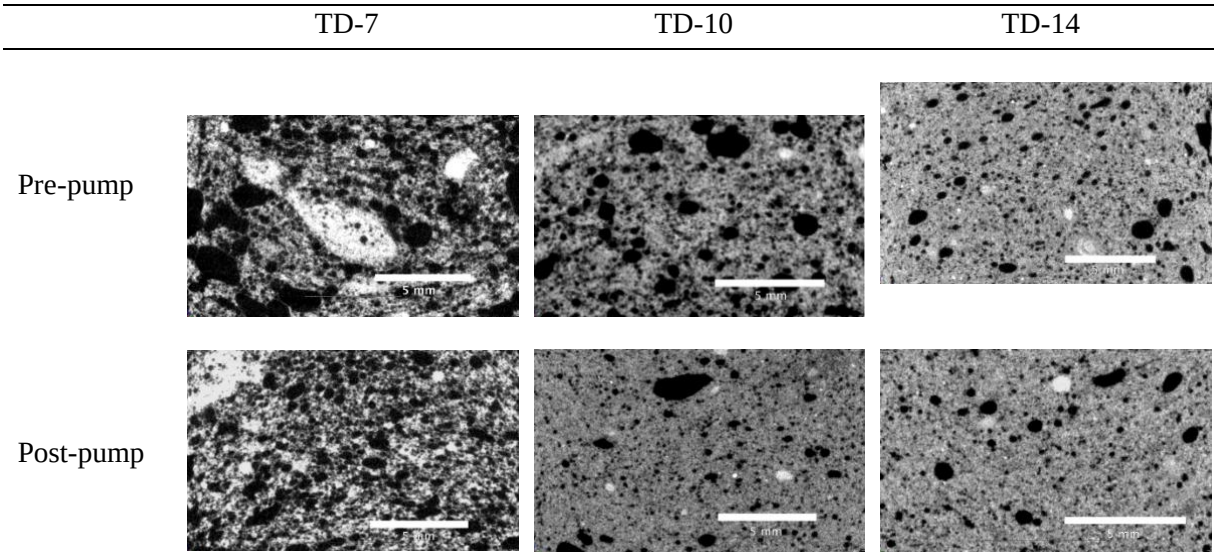

Fig. 3.10 2D cross-section image of hardened pre- and post-pump LWFC obtained by X-ray tomography

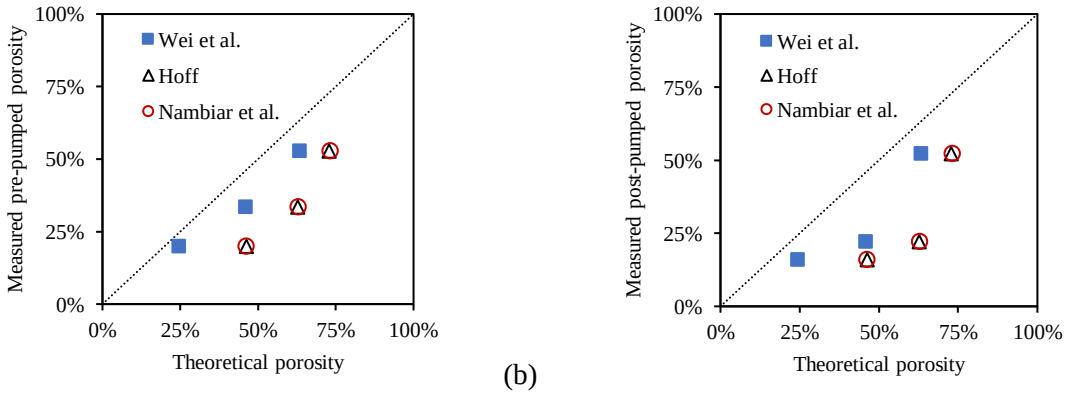

Fig. 3.11 Computed theoretical porosity plot against (a) measured pre-pumped porosity, and (b) measured post-pumped porosity

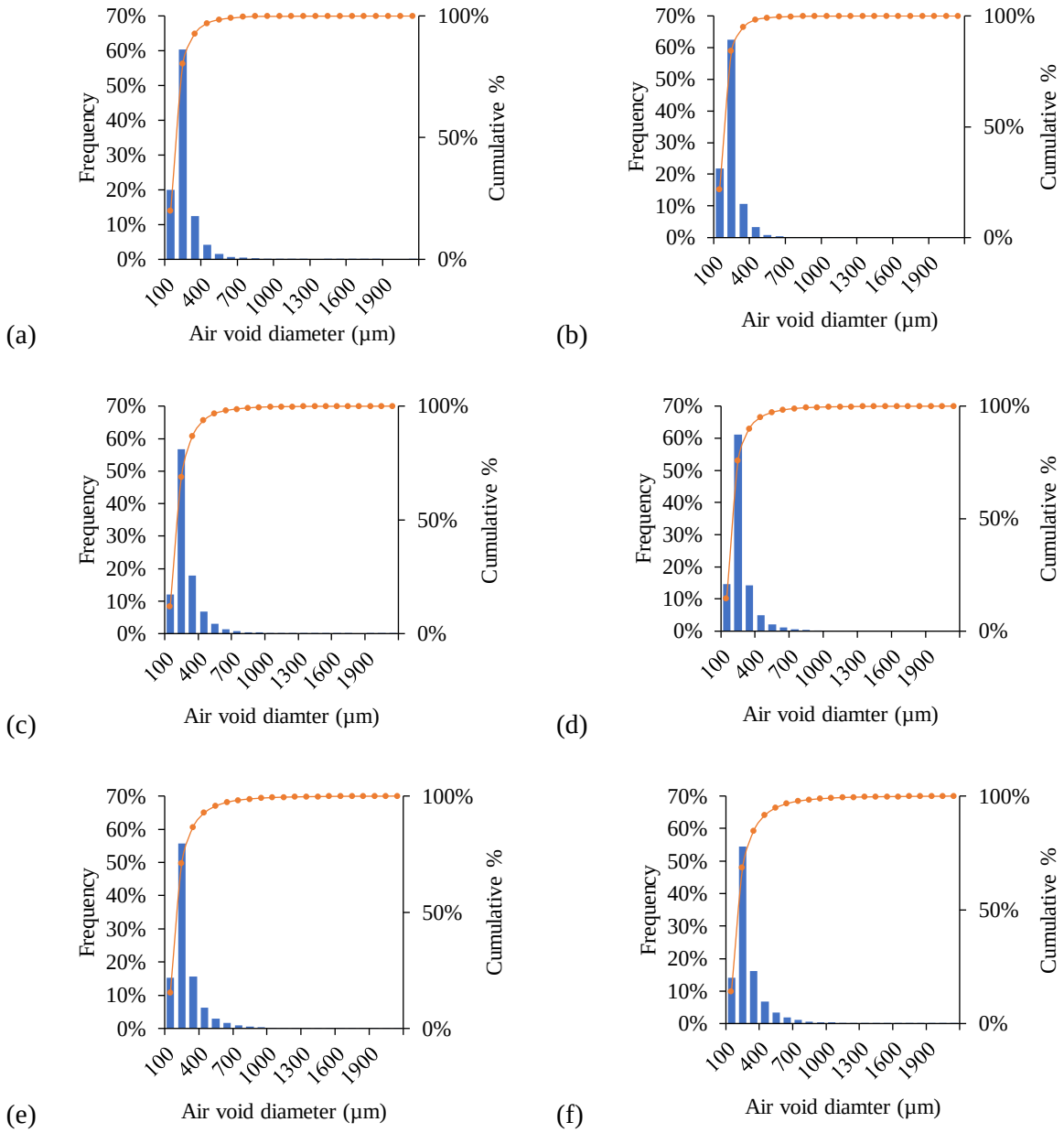

Fig. 3.12 Pore size distribution of (a) pre-pump TD-7, (b) post-pump TD-7, (c) pre-pump TD-10, (d) post-pump TD-10, (e) pre-pump TD-14, and (f) post-pump TD-14

3.5 Conclusions

A stability assessment of a novel additive manufacturing application of LWFC and foam destabilisation mechanisms under dynamic condition, i.e. pumping, are reported in a comprehensive manner. It is hypothesised that coalescence is the dominant foam destabilisation mechanism for highly stiff concrete mix, the yield stress of 100 Pa or more, in which most reports studying the stability of foam concrete mainly focus on ripening and drainage in a base mix with a yield stress of 10 – 100 Pa.

Obtaining the most appropriate stiffness for the base mix, to satisfy foam stability as well as buildability, is the most challenging work for developing 3D printable material due to the countering nature between

securing foam stability and buildability. LWFC with a target density of 700 kg/m^3 was produced with various base mixes and all samples showed stability. The influence of external pressure on foam stability was investigated once the first part of the study was completed. The key findings of the second part of the study are as follows:

- In a static condition, most LWFC with different wet density is clearly seen to secure foam stability from the gravimetric and volumetric measure comparisons between wet and mature densities.
- When extra constant pressure of 80 kPa is applied, no significant density change was found. This indicates that the studied LWFC can bear up to the applied pressure without significant foam degradation.
- When pumping pressure is applied, TD-7 shows only subtle density changes over various pumping feed durations. This may be a result of the cushion effect due to the high foam volume fraction.
- TD-10 and TD-14 show notable density increase throughout the pumping feed durations, and the post-pump densities are eventually outside the tolerance region. A continuous concrete mixer for the pump and base mix stiffness modification may remedy this and further research is required to investigate the use of a continuous concrete mixer for 3DP-LWFC.
- The void structure of LWFC was analysed by X-CT, and dominant pore size of 100 – 400 µm in diameter was found. This analysis allowed a comparison of the porosity and sphericity of pre- and post-pump LWFC samples, and reduction of porosity and sphericity was found in the TD-10 and TD-14 post-pump samples.
- Pumping pressure increased the sphericity and reduced void size of TD-7, which is an indication of high-quality foam. Investigating a possible threshold foam content beyond which pumping improves the void microstructure, is recommended.
- From the pore size-frequency distribution, smaller sized pore fractions are found in the post-pump samples due to the extra pressure.

Declaration of competing interest

None.

CRediT authorship contribution statement

Seung Cho: Conceptualisation, Data curation, Methodology, Formal analysis, Validation, Writing – original draft, Visualisation, Investigation. **Algurnon van Rooyen**: Conceptualisation, Supervision, Writing – review & editing. **Elsabe Kearsley**: Conceptualisation, Data curation, Investigation, Writing – review & editing. **Gideon van Zijl**: Conceptualisation, Supervision, Writing – review & editing, Project administration, Funding acquisition.

Acknowledgements

Cathay Industries (Africa) is acknowledged for providing CSA cement. The research is supported by The Concrete Institute in South Africa.

3.6 References

ASTM International. 2015. ASTM C1437-15 Standard test method for flow of hydraulic cement mortar.

Basařová, P. & Zedníková, M. 2019. Effect of surfactants on bubble-particle interactions, in Ashim Kumar Dutta (ed.). *Surfactants and Detergents*. IntechOpen.

Butt, H.J., Graf, K. & Kappl, M. 2003. *Physics and Chemistry of Interfaces*. Wiley Online Books.

Chen, M., Li, L., Zheng, Y., Zhao, P., Lu, L. & Cheng, X. 2018. Rheological and mechanical properties of admixtures modified 3D printing sulphoaluminate cementitious materials. *Construction and Building Materials*. 189:601–611.

Cho, S., Kruger, J., Zeranka, S. & van Zijl, G. 2019. 3D printing concrete technology and mechanics. *Concrete Beton Technical Journal*. (158). [Online], Available: https://concretesociety.co.za/images/stories/publications/cb-issue-158.pdf.

Choi, M.S., Kim, Y.J. & Kwon, S.H. 2013. Prediction on pipe flow of pumped concrete based on shear-induced particle migration. *Cement and Concrete Research*. 52:216–224.

Derjaguin, B. V, Churaev, N. V & Muller, V.M. 1987. *Surface Forces*. New York: Consultants Bureau.

Dhasindrakrishna, K., Pasupathy, K., Ramakrishnan, S. & Sanjayan, J. 2020. Effect of yield stress development on the foam-stability of aerated geopolymer concrete. *Cement and Concrete Research*. 138:106233.

Falliano, D., De Domenico, D., Ricciardi, G. & Gugliandolo, E. 2018. Experimental investigation on the compressive strength of foamed concrete: Effect of curing conditions, cement type, foaming agent and dry density. *Construction and Building Materials*. 165:735–749.

Falliano, D., De Domenico, D., Ricciardi, G. & Gugliandolo, E. 2020. 3D-printable lightweight foamed concrete and comparison with classical foamed concrete in terms of fresh state properties and mechanical strength. *Construction and Building Materials*. 254:119271.

Fameau, A. & Salonen, A. 2014. Effect of particles and aggregated structures on the foam stability and aging. *Comptes Rendus Physique*. 15(8–9):748–760.

Feneuil, B., Roussel, N. & Pitois, O. 2019a. Yield stress of aerated cement paste. *Cement and Concrete Research*. 127:105922.

Feneuil, B., Aimedieu, P., Scheel, M., Perrin, J., Roussel, N. & Pitois, O. 2019. Stability criterion for fresh cement foams. *Cement and Concrete Research*. 125:105865.

Feneuil, B., Roussel, N. & Pitois, O. 2019b. Optimal cement paste yield stress for the production of stable cement foams. *Cement and Concrete Research*. 120:142–151.

Hoff, G.C. 1972. Porosity-strength considerations for cellular concrete. *Cement and Concrete Research*. 2(1):91–100.

Hover, K.C. & Phares, R.J. 1996. Impact of concrete placing method on air content, air-void system parameters, and freeze-thaw durability. *Transportation Research Record*. 1532(1):1–8.

Jones, M.R. & McCarthy, A. 2005. Utilising unprocessed low-lime coal fly ash in foamed concrete. *Fuel*. 84(11):1398–1409.

Jones, M.R., Zheng, L. & Ozlutas, K. 2016. Stability and instability of foamed concrete. *Magazine of Concrete Research*. 68(11):542–549.

Ke, G., Zhang, J., Xie, S. & Pei, T. 2020. Rheological behavior of calcium sulfoaluminate cement paste with supplementary cementitious materials. *Construction and Building Materials*. 243:118234.

Kearsley, E. & Mostert, D. 2005. Designing mix composition of foamed concrete with high fly ash contents. in *Use of Foamed Concrete in Construction* (Conference Proceedings). Thomas Telford Publishing. 29–36.

Klein, N.S., Bachmann, J., Aguado, A. & Toralles-Carbonari, B. 2012. Evaluation of the wettability of mortar component granular materials through contact angle measurements. *Cement and Concrete Research*. 42(12):1611–1620.

Kruger, J., Zeranka, S. & van Zijl, G. 2019. An ab initio approach for thixotropy characterisation of (nanoparticle-infused) 3D printable concrete. *Construction and Building Materials*. 224:372–386.

Kruger, J., du Plessis, A. & van Zijl, G. 2021. An investigation into the porosity of extrusion-based 3D printed concrete. *Additive Manufacturing*. 37:101740.

Le, T., Austin, S., Lim, S., Buswell, R.A., Gibb, A. & Thorpe, A. 2012. Mix design and fresh properties for high-performance printing concrete. *Materials and Structures*. 45:1–12.

Lessard, M., Baalbaki, M. & Aïtcin, P.-C. 1996. Effect of pumping on air characteristics of conventional concrete. *Transportation Research Record*. 1532(1):9–14.

Markin, V., Nerella, V.N., Schröfl, C., Guseynova, G. & Mechtcherine, V. 2019. Material design and performance evaluation of foam concrete for digital fabrication. *Materials*. 12(15).

Mechtcherine, V., Bos, F.P., Perrot, A., da Silva, W.R.L., Nerella, V.N., Fataei, S., Wolfs, R.J.M., Sonebi, M., et al. 2020. Extrusion-based additive manufacturing with cement-based materials –

Production steps, processes, and their underlying physics: A review. *Cement and Concrete Research*. 132:106037.

Mose, M.P. & Perumal, D. 2016. Latest advances in alternative cementations binders than portland cement. *IOSR Journal of Mechanical and Civil Engineering*. 13:45–53.

Nambiar, E.K.K. & Ramamurthy, K. 2006. Influence of filler type on the properties of foam concrete. *Cement and Concrete Composites*. 28:475–480.

Nambiar, E.K.K. & Ramamurthy, K. 2008. Models for strength prediction of foam concrete. *Materials and Structures*. 41(2):247–254.

Panda, B., Paul, S.C. & Tan, M.J. 2017. Anisotropic mechanical performance of 3D printed fiber reinforced sustainable construction material. *Materials Letters*. 209:146–149.

Paul, S.C., van Zijl, G.P.A.G. & Gibson, I. 2018. A Review of 3D concrete printing systems and materials properties : current status and future research prospects. *Rapid Prototyping Journal*. 24(4):784–798.

Phan, C.M., Nguyen, A. V., Miller, J.D., Evans, G.M. & Jameson, G.J. 2003. Investigations of bubble-particle interactions. *International Journal of Mineral Processing*. 72(1–4):239–254.

du Plessis, A., le Roux, S.G. & Guelpa, A. 2016. The CT Scanner Facility at Stellenbosch University: An open access X-ray computed tomography laboratory. *Nuclear Instruments and Methods in Physics Research Section B: Beam Interactions with Materials and Atoms*. 384:42–49.

du Plessis, A., Olawuyi, B.J., Boshoff, W.P. & le Roux, S.G. 2016. Simple and fast porosity analysis of concrete using X-ray computed tomography. *Materials and Structures*. 49(1):553–562.

Pugh, R.J. 1996. Foaming , foam films , antifoaming and defoaming. *Advances in Colloid and Interface Science*. 64:67–142.

van Rooyen, A.S. 2020. *Mechanics and durability of surface treated structural foamed concrete*. Published doctoral dissertation. Stellenbosch University.

Roussel, N. 2006. A thixotropy model for fresh fluid concretes: Theory, validation and applications. *Cement and Concrete Research*. 36(10):1797–1806.

She, W., Du, Y., Zhao, G., Feng, P., Zhang, Y. & Cao, X. 2018. Influence of coarse fly ash on the performance of foam concrete and its application in high-speed railway roadbeds. *Construction and Building Materials*. 170:153-166.

South African National Standard. 2013. SANS 50197-1 Part 1 : Composition, specifications and conformity criteria for common cements.

Wang, L. & Yoon, R. 2008. Effects of surface forces and film elasticity on foam stability. *International Journal of Mineral Processing*. 85:101–110.

Wei, S., Yiqiang, C., Yunsheng, Z. & Jones, M.R. 2013. Characterization and simulation of microstructure and thermal properties of foamed concrete. *Construction and Building Materials*. 47:1278–1291.

Zeng, X., Lan, X., Zhu, H., Liu, H., Umar, H.A., Xie, Y., Long, G. & Ma, C. 2020. A review on bubble stability in fresh concrete: Mechanisms and main factors. *Materials*. 13(8):1–24.

Chapter 4

Rheology and application of buoyant foam concrete for digital fabrication

Seung Cho, Jacques Kruger, Algurnon van Rooyen, Gideon van Zijl

Division for Structural Engineering and Civil Engineering Informatics, Stellenbosch University, 7600, South Africa

Reproduced and reformatted from an article published in the *Composites Part B: Engineering Journal*.

Abstract

In the fresh state, conventional lightweight foam concrete (LWFC) has low yield stress, in the order of tens of Pascal, which challenges shape retention and buildability in digital construction. Several literatures attempt to address the rheological performance of 3D printable lightweight foam concrete (3DP-LWFC) in essence. This research presents a comprehensive laboratory rheological characterisation with controlled shear rate tests and flow curve tests over different foam volume fractions and densities of 700 kg/m^3, 1000 kg/m^3 and 1400 kg/m^3. LWFC is appropriately adapted for extrusion-based 3D printing. Accordingly, this allows to evaluate yield stress (347 – 812 Pa), thixotropic performance (rate of reflocculation (R_{thix}) 0.21 – 3.15 Pa/s and rate of structuration (A_{thix}) 0.06 – 1.02 Pa/s), viscosity (2.5 – 3.4 Pa.s), and elastic shear modulus evolution depending on the densities of LWFC. To analyse the constructability in additive manufacturing, shape retention and buildability are investigated , resulting in up to 15 deposited filament layers to be reached in a buildability test. Lastly, a potential 3DP-LWFC practical application is addressed by producing a buoyant 3D printed façade element, i.e. wet density less than 1000 kg/m^3 leading to further lowered mature density.

Highlights

- A comprehensive light weight foam concrete comparative study of rheology and 3D printability is presented
- 3D printable foam concrete is adapted and validated to be constructable at reasonable building rates
- A digitally fabricated and parametrically designed buoyant LWFC façade element is presented

Keywords: Foamed concrete; 3D printed concrete; rheology; constructability; fibre reinforced concrete; digitally fabricated concrete

4.1 Introduction

The advent of a new era for industrial revolution 4.0 (4IR) has successfully been unfolded with fast-growing rate and the movement has captured great attention from various parties such as industry, academia, government, and society. A demand to embrace the technological advancement for the construction industry has appeared as digital construction (DC). The key driver of the demand is to develop the most cost-effective and optimised construction method by acquiring the building geometry freedom, such as topology optimisation. It is believed that extrusion-based 3D concrete printing (3DCP), the most common type of DC, will satisfy the demand by primarily reducing material waste generation and lowering costs by negating the use of formwork, amongst many other benefits. (Buswell *et al.*, 2018; Jayathilakage *et al.*, 2020; Panda *et al.*, 2019).

In parallel to technological advancement, the construction industry has been strongly urged to move towards sustainable development to reduce environmental impacts (Yeo & Gabbai, 2011). Portland Cement (PC) is mainly accused of the significant energy consumption in cement production, 8 – 10 EJ per year (approximately 2 – 3% of global primary energy use), and high carbon dioxide release, approximately up to 8 % of global CO_2 anthropogenic emissions from cement industry (Andrew, 2019; Taylor *et al.*, 2006) in the construction industry. In "green construction", the total energy consumption is optimised during the material and structural design processes. During the material design process, carbon content can be largely reduced by substituting with low-carbon cement, recycled aggregates and/or by-product pozzolans generated by other industries as supplementary cementitious materials (SCMs) in which the latter is the most widely used method (Yeo & Gabbai, 2011). A careful structural optimisation leads to total structure weight reduction, but also a lightweight building material selection is the way to reduce the embodied energy of a concrete structure.

A highly porous cementitious material engineered by foam inclusion, so-called lightweight foamed concrete (LWFC) with a density range of 400 – 1600 kg/m^3 proportional to the foam volume fraction (van Rooyen, 2020), is known as an energy-efficient building material due to its excellent thermal and acoustic insulative properties mainly contributed by the high cavity volume and sound mechanical

property with high strength-to-weight ratio, so-called specific strength, which may be exploited in its application as a structural component (Jones & McCarthy, 2005b; Kearsley & Wainwright, 2001), also including steel bar reinforcement (de Villiers, van Zijl & van Rooyen, 2017). Owing to the advantageous nature of LWFC, this material has widely been used in the construction industry either non-structurally, e.g. void and trench backfilling, or structural purposes, e.g. pre-cast slab (van Rooyen, 2020). More recently, several attempts have been made to adapt LWFC for extrusion-based 3DCP application via rheological modification (Cho *et al.*, 2019; Falliano *et al.*, 2020; Markin *et al.*, 2019) as classic LWFC is originally designed to have self-levelling properties, which links to high workability or low fresh state shear yield capacity in the order of tens of Pascals (Ahmed *et al.*, 2009).

Knowing many successful sustainable 3D printable materials are reported in the literature (Bong *et al.*, 2019; Chen *et al.*, 2019; Panda *et al.*, 2017), the marriage of LWFC and 3DCP is an auspicious attempt for sustainability in several aspects. Precursor foam addition leads to a reduction in weight of bulk material which consequently reduces the embodied energy of built structures as well as binder content since the volume of air can constitute approximately up to 77% of the bulk material depending on the designed density. Moreover, several studies attempted designing LWFC with high fly ash content, up to 75% of binder mass, and agreed that, thereby, mechanical and microstructural properties improve over the long term, such as up-trending compressive strength even at 56 days and increased pore wall thickness due to late hydration at the interface of pores contributed by fly ash (Jones *et al.*, 2017; Kearsley & Wainwright, 2001). Calcium sulfoaluminate (CSA) cement is a suitable substitutive material for Portland cement (PC) as it requires less energy in production and emits less carbon dioxide during manufacturing. Jones et al (Jones *et al.*, 2016) found partial substitution with CSA cement in LWFC lead to significantly improved foam stability due to rapid early strength evolvement. On top of the promising properties, the rapid hardening property of CSA, excessive and rapid ettringite formation by high ye'elimite (C4A3S) content which is present in sulfoaluminate belite and ferrialuminate clinkers (Mose & Perumal, 2016), in LWFC is expected to increase the constructability in 3DCP application.

Extrusion-based 3DCP requires a certain rheological performance of cementitious materials for the pumping and layer deposition processes, namely pumpability and buildability, respectively. Foremost the deposited filament should retain its extruded shape, known as shape retention in 3DCP terms, without significant deformation at the instant of material deposition dominantly under gravity-induced stress, ρgh, with ρ material bulk density, g gravitational acceleration, and h is the filament layer height. Mechtcherine et al. (2020) reported a normal weight cement-based material with yield stress below 100 Pa exhibits significant deformation after extrusion, thus recommended a yield stress in the range of a hundred to a few thousand Pa to prevent initial deformation. It should be mentioned that the inertia stress occurs during the printing process, but only becomes significant for fast deposition process, i.e. head speed >> extrusion rate, whilst surface tension only controls the shape in the case of extremely

thin layers (Roussel, 2018). From the completion of the first layer, the bottom-most layer suffers under the gradually increasing gravity-induced stress from the weight of the subsequent layers as the printing process continues. Several studies reported a range of yield stress, 0.27 – 0.9 kPa, and plastic viscosity, 21.1 – 38.7 Pa.s, of the normal weight concrete for suitable pumping and extrusion without noticeable rupture in the filament during 3DCP (Le *et al.*, 2012; Thrane *et al.*, 2010).

Fresh concrete fails mainly due to relative particle movement in compression like soil, i.e. plastic yield in shear failure whilst the gravity-induced stress resulting from the upper layers, the governing loading, acts as a normal stress. Thus, conversion between normal and shear stress needs to be addressed for the accurate 3DCP material behaviour modelling under loading. Perrot et al (Perrot *et al.*, 2015) borrowed a squeeze flow theory (Engmann *et al.*, 2005; Roussel & Lanos, 2003) to provide a direct proportionality between normal and shear stresses with a geometric factor in 3DCP, namely $\sigma(t)=\alpha_{geom}\cdot\tau(t)$, where α_{geom} is a built shape-dependent geometric factor. Kruger et al (Kruger *et al.*, 2019a) established the relationship between normal and shear stresses based on the rheo-mechanical approach by introducing the strength correction factor which is normalised to Tresca shear failure at a filament layer aspect ratio of two. Meanwhile the general shear-normal stress relationship is complex to obtain due to the time-dependent variables, such as cohesion, friction angle, surface friction and stiffness of the material, but the strength correction factor, denoted as F_{AR}, simplifies the relationship, namely $\tau = \sigma/(2F_{AR})$, based on the principle that the stress ratio increases as the material friction angle increases due to increased confinement. It is worthwhile to mention that the strength correction factor is dependent on the aspect ratio of 3DCP filament layer, which generally is less than one due to stability issues. The adjusted strength correction factor-aspect ratio plot for general 3DCP can be found in (Kruger *et al.*, 2019a), but may differ between materials. More generalised shear-normal stress relation in a 3D printed filament which is not excessively confined and shows the zonal difference in shear-normal stress ratio can be found in (Kruger *et al.*, 2020).

A thixotropy nature, i.e. a microstructural restoration ability at rest immediately after internal structure breakdown occurred, of visco-plastic cementitious materials is crucial for most 3DCP techniques in which short yield stress recovery time of the agitated material is preferred (Roussel, 2018). Material strength evolves with either intermolecular force interaction linked to flocculation or the re-flocculation mechanism (Kruger *et al.*, 2019b) in the more short term, or microstructural build-up, linked to the structuration mechanism over a longer period due to ettringite and portlandite formation at rest ettringite and portlandite formation at rest (Reiter *et al.*, 2018) while the material stiffness, e.g. elastic shear modulus $G(t)$, also evolves over time (Roussel, 2018). Roussel et al (2006) proposed a thixotropy model with constant material strength increase by a constant hydration product formation rate during the dormant period, which is linked to a constant heat of hydration and the constant rate is named as structuration rate and denoted as A_{thix}. Based on the constant structuration rate, the time-dependent material yield stress is defined as $\tau(t) = \tau_0 + A_{thix}\cdot t$, where τ_0 is the initial yield stress of the material. The

linear material strength build-up model was partially modified by Kruger et al. (2019b). The authors proposed a bi-linear model composed of initial strength build-up segment from the initial dynamic yield stress to initial static yield stress of material with constant increasing rate, the so-called re-flocculation rate and denoted as R_{thix} as a measure of thixotropy, followed by a structuration segment with a constant A_{thix} value from the restored initial static yield stress point and onward. The bi-linear model is expressed by the following equations:

$$\tau(t) = \begin{cases} \tau_{D,i} + R_{thix} \cdot t & t \leq t_{rf} \\ \tau_{S,i} + A_{thix} \cdot (t_{rf} - t) & t > t_{rf} \end{cases} \quad (4.10)$$

where $\tau_{S,i}$ is initial static yield stress, $\tau_{D,i}$ is initial dynamic yield stress and t_{rf} is re-flocculation time defined as $t_{rf} = (\tau_{S,i} - \tau_{D,i})/R_{thix}$.

The latter modified model is, in particular, more applicable for 3DCP because the deposited material is mostly sheared during pumping and the freshly deposited layer starts to re-flocculate the material microstructure at rest from the initial dynamic yield stress due to prior shear action. Thus, a high re-flocculation rate is preferred so that the bottom layer does not show a plastic yield of material when it is pressured by the subsequent layer which leads to excellent buildability performance in 3DCP.

The buildability remains a challenge due to the relatively low yield capacity of LWFC, and rheology modification of LWFC is therefore required for 3DCP application (3DP-LWFC). The rheological modification of LWFC is largely branched into two methods, namely increasing packing density with high fineness constituents, such as silica fume and nanoparticles, and the usage of chemical additives. Cho et al. (2019) attempted to modify the rheology of LWFC with a density of 1400 kg/m^3 via nano-silica powder incorporation without chemical additives and reported a static yield shear stress range of 224.2 Pa – 1169.9 Pa depending on the amount of nanoparticle addition. However, the study found unusual R_{thix} and A_{thix} gradients, i.e. negative or constant rate, and it was ascribed to segregation between the material stuck in the rheometer vane and the rest resulting in measuring the torque of the mass inertia of the LWFC adhered to the vane blades, rendering the test invalid. The study nevertheless produced a 3D printed 250 mm diameter hollow circular column with 10 mm layer height and achieved 17 successfully deposited filament layers. Markin et al. (2019) reported a systematic approach to develop 3DP-LWFC with aid of chemical additives by showing a stable 3D printed 160-mm high rectilinear wall object, and the authors carried on the experimental works on hardened state properties such as mechanical, microstructural, and thermal conductivity characterisations. The same group followed up a study on the rheological assessment of 3DP-LWFC with a density of 1200 kg/m^3 evaluating plastic viscosity, static yield stress and dynamic yield stress at various rest time for structuration rate determination (Markin *et al.*, 2020). The study found aluminosilicate incorporation increased the structuration rate (A_{thix} = 4.9 Pa/min) as well as static yield stress (388 Pa) and plastic viscosity (9.6 Pa.s). Falliano et al. (2020) investigated an extrudable LWFC with a density range of 400 – 800 kg/m^3

for a potential 3DP-LWFC application with lateral expansion and slump measures of a vertically extruded specimen. A zero slump LWFC was achieved by viscosity-enhancing agent (VEA) incorporation and the static yield stress of 800 kg/m^3 LWFC was measured as 150 Pa in (Falliano *et al.*, 2020). Given the broad range, there appears not to be agreement on "printable" rheology for the range in reported densities of LWFC.

This present paper focuses on fresh state characterisation of 3DP-LWFC over three different target densities, namely 700, 1000, and 1400 kg/m^3. Foremost, 3DP-LWFC modification process and production procedures are discussed in detail. Setting time analysis with Vicat penetration method is performed to determine printing open time, i.e. the maximum duration the material is still in flowable or pumpable condition. Rheological properties are characterised by rotational concrete rheometry over two types of tests, namely, shear rate-controlled test for static yield stress (τ_S) and flow curve test for dynamic yield stress (τ_D) and plastic viscosity known as Bingham parameters (μ). Thixotropic parameters, R_{thix} and A_{thix}, are calculated from a series of shear rate-controlled test results over different rest periods, e.g. 1 min, 5 min, 10 min, 15 min, and 30 min. To investigate flowability after agitation, standardised slump flow table test (ASTM International, 2015) is performed and linked with rheological parameters as per (Cho *et al.*, 2020). After the fresh state characterisation, an expected number of buildable layers is calculated for the three test samples according to the buildability model, and finally 3D printing a concrete circular hollow column until failure occurs. Lastly, several buoyant façade structure fabrications, i.e. mature density (air curing dry density) less than 1000 kg/m^3, are reported to discuss the practical application of 3DP-LWFC.

4.2 Methodology

4.2.1 Material properties and mix design

Conventional LWFC mix design is comprised of mainly unary or binary cement systems, namely cement and fly ash (Kearsley & Mostert, 2005; Nambiar & Ramamurthy, 2006), whilst ternary cement system is occasionally used to reduce the cement content further (Jones *et al.*, 2017). To mitigate the highly workable cementitious material, water content reduction and packing densification in micro- and macro scale of base mortar mix are employed motivated by high-performance concrete mix design approach (Abd & Hillemeier, 2014). Based on the provided mix design, binary cement system and sand, with lower bound of water demands of cement and fly ash (Kearsley & Mostert, 2005), a portion of cement is substituted by fine aggregates to enhance the rheology. Silica fume, a pozzolanic material with high specific surface area, increases flow resistance and gel strength by early gel formation due to the ionisation of the surface of silica fume particle bonding with polyvalent cations, e.g. calcium (Vikan & Justnes, 2007). In parallel, nanoparticle inclusion in cementitious material with the high surface area-to-volume ratio which is equivalent to significantly larger contact surface with reacting particles, is believed to accelerate the pozzolanic chemical reaction, i.e. portlandite and ettringite production at a

higher rate in a well-dispersed state (Paul *et al.*, 2018). The accelerated ettringite and portlandite formation contributes the flocculation strength and floc size that may lead to an increase in viscosity and shear yield capacity (Voigt *et al.*, 2010). Jones et al. (Jones *et al.*, 2016) proposed and validated the CSA cement addition for foam stability of LWFC by accelerating solidification rate than bubble destabilising rate. Furthermore, the rapid ettringite formation in the early stage is hypothesised to contribute to promoting mainly A_{thix} while it still affects R_{thix}. Several literatures studied synthetic fibre reinforcement in LWFC (Jones & McCarthy, 2005a; Kearsley & Mostert, 2005). Fibre addition has advantages of workability reduction, crack control, tensile strength and impact resistance improvement. No chemical additive is considered in this paper.

The cement type is here selected to be CEM II/A-L 52.5N which contains 6 – 20% limestone extenders and conforms to SANS 50197-1 (2013). Locally manufactured fly ash called Durapozz and categorised as class F according to SANS 50197-1 (2013), FerroAtlantica silica fume, and nano silicon dioxide ($nSiO_2$) powder with an average particle size of 30 ± 5 nm are selected as extenders. Fine graded sand is used as inert material in the mix design with particle size range 0.1 – 0.5 mm. It is noted that larger aggregate particles up to 4.8 mm have successfully been used by the authors in foam concrete (Kruger *et al.*, 2020), and would comply with the 3DCP pump specification used, but have not been studied here. Type III CSA cement manufactured by Royal White Cement (RWC), with a subtle change in SiO_2 and Al_2O_3 content, is used for the fixed CSA to cement ratio of 10%. Synthetic fibre type for fibre reinforcement is 6 mm polypropylene (PP) fibre, included for plastic shrinkage crack control, handling and impact resistance. Chemical and physical attributes of constituents are summarised in Table 4.1 and Table 4.2, respectively.

Table 4.1 Chemical composition (in weight percentages) of cement, CSA, Fly ash, and Silica fume

	SiO_2	Al_2O_3	Fe_2O_3	CaO	MgO	K_2O	Na_2O	TiO_2	SO_3
Cement	21.5	5.5	3	65.5	2.0	<0.5	<0.5	-	1.5
CSA	10.5	34	2.5	42.5	3.5	-	-	1.5	8.5
Fly Ash	54.1	31.8	3.2	4.9	1.2	0.8	0.2	1.7	-
Silica Fume	99.5	<0.1	<0.1	<0.1	<0.1	-	-	-	-

Table 4.2 Physical properties of the particles, with ρ the density and S the specific surface area

Materials	OPC	CSA	Fly ash	Silica Fume	Nano SiO_2	Sand	PP fibre
ρ (kg m^{-3})	3.15	3.1	2.2	2.9	0.2	2.65	0.91
S (m^2 g^{-1})	0.40	0.48	0.3 - 0.4	13 - 20	200		

A mix design is formulated based on the principles of mass conservation and foam stability with a prime design factor of target wet density (Kearsley & Mostert, 2005). The formulation is comprised of two parts, the first balance equation indicating total constituents must make up the target wet density and the second part is the balance of total volume to be unit volume, with two variables which are cement content (c) and precursor foam volume (V_f) as follows:

$$\rho_t = c \cdot [\alpha + \beta] + RD_f \cdot V_f \tag{4.11}$$

$$1 = c \cdot [\beta + \gamma] + V_f \tag{4.12}$$

where *c* cement, *a* fly ash, *s* sand, *sf* silica fume, *nS* nano silica and

$$\alpha = 1 + (CSA/c) + (a/c) + (s/c) + (sf/c) + (nS/c)$$

$$\beta = (w/CSA)(CSA/c) + (w/a)(a/c) + (w/s)(s/c) + (w/sf)(sf/c) + (w/nS)(nS/c)$$

$$\gamma = \frac{1}{RD_c} + \frac{(CSA/c)}{RD_{CSA}} + \frac{(a/c)}{RD_a} + \frac{(s/c)}{RD_s} + \frac{(sf/c)}{RD_{sf}} + \frac{(nS/c)}{RD_{nS}}$$

Thus, constituents are proportioned to cement content *(x/c)*, and water demand *(w/x)* determined for appropriate flowability by using ASTM flow table tests (2015). Water demand of each constituent is determined by sensitivity analysis to have the same consistency by controlling the slump flow of 220 mm (Kearsley & Mostert, 2005). In general, water demand of cement is first determined, and each constituent is mixed with cement and water to determine both water demand and proportion to cement thereof. It must be mentioned the fly ash-to-water ratio (*w/a*) is the only variable to control the rheology of LWFC. Though there is a risk for foam stability, the flow diameter of modification is unavoidable for 3DCP application and the range of 185 mm – 195 mm is desired and controlled based on the sensitivity analysis by varying *w/a* ratio. In appreciation of the rapid hardening process by CSA cement, the foam instability issue is postulated to be partially or completely counteracted. No specific investigation is made or reported for foam stability testing since that is beyond the scope of this study, but foam stability of 3DP-LWFC is currently under investigation by the authors. The determined ratios are summarised in Table 4.3. Three 3DP-LWFC test samples with different wet target densities are prepared, namely 700, 1000 and 1400 kg/m^3, and named TD-7, TD-10, and TD-14, respectively. Based on the flow diameter of the base mix, water-to-fly ash ratios of 0.33, 0.30 and 0.28 are used for TD-7, TD-10, and TD-14, respectively.

Table 4.3 Water demand (w/x) and proportions to cement content (x/c) for 3DP-LWFC mix design

Materials	Cement	CSA	Fly ash	Sand	Silica fume	Nano silica	PP fibre
w/x	0.375	0.375	Variable*	0.08	0.71	0.84	*0.4% of total mix volume
x/c	1.0	0.1	1.0	0.2	0.1	0.02	

* Minimum w/a ratio 0.25 according to (Kearsley & Mostert, 2005)

4.2.2 3DP-LWFC production

Though there are several LWFC production methods available, this study focuses on the precursor aqueous foamed concrete. In this case, foamed concrete is comprised of a binary step production process, namely fine aggregate mortar mix, so-called base mix, and precursor aqueous foam inclusion. Base mix production is identical to a normal concrete mix process. An aqueous surfactant solution is prepared by diluting commercially available protein-based foaming agent with a ratio of 1:40 with ferrous sulphate inclusion by 1.25% per mass of water as a foam stabiliser. Precursor foam is generated through a mechanical agitation process of the aqueous solution with a flow rate of 1 – 3 litres per second and air pressure of 5 – 6 bar. The generated aqueous foam is considered to be stable, and density is controlled to be 75 ± 5 kg/m^3. A homogeneous LWFC is produced by mixing the individually prepared based mix and aqueous foam. Density measure of freshly produced LWFC is used as acceptability check whether wet density falls within the tolerance of target wet density, namely ± 50 kg/m^3. If the actual density measures 50 kg/m^3 more than the target density, a reasonable amount of foam can be added to attain the target density, while LWFC with actual density under the tolerance is recommended to be discarded.

4.2.3 Setting time

Setting times of three 3DP-LWFC samples are measured in a climate-controlled room, 23±2^{o}C and 65±5% relative humidity, by Vicat penetration method standardised in BS EN 196-3 (2016).

4.2.4 Rheometer measurement

Since the rheological property is measured in a fresh state of anisotropic cementitious material, the rheological characterisation is intricate and changes over time. Thus, a reliable instrument must be chosen for correct measurement and the test needs to be designed with care. A rotational concrete rheometer developed by International Centre for Aggregate Research (ICAR) is used here throughout the rheometer measurement test period. The rheometer records the reaction torque generated by the vane relative to the reference stationary point.

4.2.4.1 Controlled shear rate test

A typical material response curve of a controlled shear rate (CSR) test is depicted in Fig. 4.1. The torque build-up is recorded until the first peak implying the static yield stress point, and plateaus at a

depreciated torque value implying the dynamic yield stress. CSR test results are highly dependent on the shear history of a sample; thus, the shear disturbance must be minimised before the initial static and dynamic yield stress measurement.

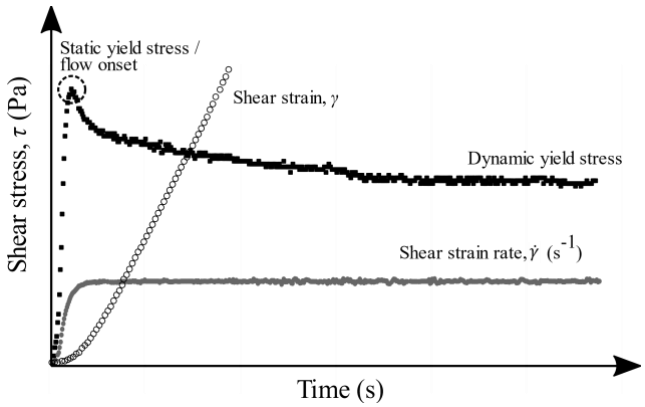

Fig. 4.1 CSR test responsive curve

A constant shear strain rate of 0.125 s^{-1} is appropriate for many concrete materials according to the recommendation of the manufacturer, but the proposed shear rate is not suitable to replicate the pumping process of 3DCP at Stellenbosch University. Kruger et al. (Kruger *et al.*, 2019a) proposed a shear rate of 1 s^{-1} converted from vane rotational speed of 0.2 revolutions per second which is equivalent to screw speed of the pump facilitated in the concrete laboratory of Stellenbosch University for 60 mm/s printing speed. The recorded torque is converted to yield stress according to the formula:

$$\tau = \frac{2T}{\pi D^3 \left(\frac{H}{D} + \frac{1}{3}\right)} \tag{4.13}$$

where T is the maximum torque, D is the diameter of the vane, and H is the height of the vane.

Fig. 4.2 illustrates the shear strain rate calculation in the annulus between vane and container of the rheometer. With linear velocity, v, at the radius of the vane, r, corresponds to $v = r \cdot \omega$; where ω is the angular velocity of the vane in radians per second. This yields shear strain rate $\dot{\gamma} = \frac{\omega r}{Z}$; where Z is the distance between the wall of the container and the vane radius (Laskar & Bhattacharjee, 2011).

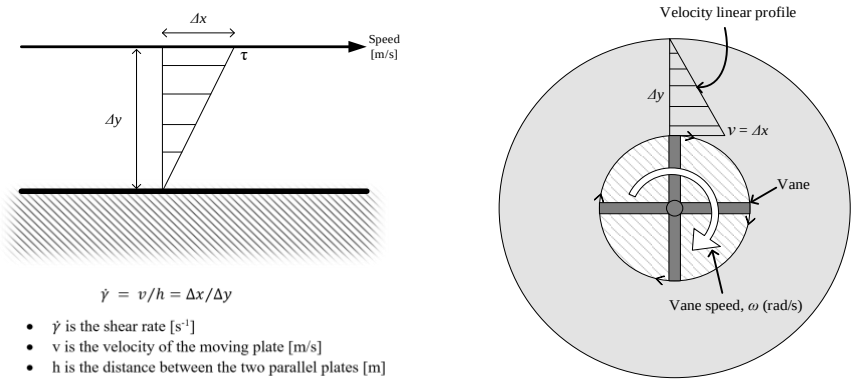

Fig. 4.2 Shear strain rate calculation, reworked from (Laskar & Bhattacharjee, 2011)

Shear strain is then calculated from the shear rate according to Eqs (4.14) and (4.15). The calculate shear strain rate and shear strain profiles of typical CSR tests are depicted in Fig. 4.1.

$$\dot{\gamma} = \frac{d\gamma}{dt} \tag{4.14}$$

$$thus, \qquad \gamma = \int \dot{\gamma} \cdot dt \tag{4.15}$$

After the initial measurement, a series of the CSR tests is performed by allowing resting intervals of 1, 5, 10, 15, and 30 min, each starting after the end of the previous test of a 20L LWFC batch. It should be mentioned that the resting interval can be adjusted according to the rheological performance of the material. Each test results in static and dynamic yield stresses and thixotropic parameters for 3DCP, re-flocculation rate R_{thix} and structuration rate A_{thix}, can be calculated from the test outputs as discussed in Section 4.1.

4.2.4.2 Flow curve test

Bingham parameters, namely dynamic yield stress and plastic viscosity, are measured by the flow curve test. The flow curve test is comprised of a series of flow curve points measured over different shear rates after the initial breakdown or pre-shear phase. The flow curve point can be measured with either descending or ascending shear rate, but only the descending shear rate flow curve is performed to obtain necessary data. The prepared batch is pre-sheared with break down shear rate of 0.5 rev/s for 20 seconds, then seven flow curve points are measured with the equally divided stepwise decreasing shear rate between 0.5 rev/s and 0.05 rev/s. The linear fitting curve is calculated and intersects point, dynamic yield stress (Pa), the gradient of the linear line, plastic viscosity (Pa.s), and R-squared value are reported.

4.2.5 Slump flow table measurement

Slump flow is measured by a mini-slump cone test method described in ASTM C1437 (2015) with the flow table and mould specified in ASTM C230 (2008). Several researchers performed slump flow test to investigate fresh state behaviour of LWFC and to correlate with rheometer results (Cho *et al.*, 2020; Jones & McCarthy, 2005b; Nambiar & Ramamurthy, 2008). In fluid mechanics, kinematic viscosity (υ), defined as a resistance capacity against the flow of a fluid under gravitational force, is used to proportionate viscosity and density of the fluid, namely $\upsilon = \mu/\rho$. Due to the different density of LWFC and flowing behaviour under dynamic loading which already exceeds static yield stress are investigated, this parameter is expected to be suitable for correlation with slump flow.

In this paper, slump flow of cementitious material is measured with multiple dynamic impacts and the correlations between the result, yield stress and kinematic viscosity of material, are investigated since flow characteristics are part of a rheologic property. Thus, both base mix and LWFC mix slump flow

results are reported for characterising flow behaviour of 3DP-LWFC as well as for quality control purposes.

4.2.6 3D concrete printing

After the fresh state characterisation of 3DP-LWFC material, the buildability performance is investigated by a rheo-mechanics based analytical buildability model presented by Kruger et al. (Kruger *et al.*, 2019a) while the investigation on pumpability is performed by observation whether there are discontinuities present in the printed filament. The model provides a buildable number of layers, which depends on the thixotropic and printing parameters until the printed structure shows plastic collapse, disregarding structural failure in the form of elastic buckling. The model compares the microstructural build-up linked to shear capacity build-up and the building rate of 3DCP. In other words, the printing object fails if the vertical building rate gradient is greater than either R_{thix} or A_{thix}. The following lists are the input parameters to the model:

- Material parameters
  - Initial static yield shear stress, $\tau_{S,i}$
  - Initial dynamic yield shear stress, $\tau_{D,i}$
  - Re-flocculation rate, R_{thix}
  - Structuration rate, A_{thix}
  - Density of LWFC, ρ
- Printing parameters
  - Filament layer width, w_l
  - Filament layer height, h_l
  - Printing path length per layer, l_p
  - Printing or nozzle speed, v

Stellenbosch University facilitates a 3-axis gantry 3D printer with positive-displacement piston pump system (Cho *et al.*, 2019). It must be mentioned the concrete batch is mixed externally and transported to the hopper of the pump for 3D printing.

The model was validated with 250 mm diameter circular hollow column structure with no infill because circular profile has a constant second moment of area about any axis and continuously provides lateral self-support leading to a more stable structure than a square hollow column. The profile provides a print path length of 785 mm per layer and it takes 13.1 s to complete each layer (pass time) based on a printing speed of 60 mm/s. A layer height of 10 mm is chosen, which roughly yields a 30 mm filament layer width from the 25 mm diameter circular nozzle. Assuming the filament profile is approximately rectangular, the aspect ratio becomes 0.33 that is equivalent to a strength correction factor of roughly 1.7 according to (Kruger *et al.*, 2019a). The model prediction and actual printing result are reported and compared.

While the buildability model is to predict failure, the reversed principle can prove as a structural design guideline (Kruger *et al.*, 2020). The failure criteria are rearranged and expressed in terms of predicted building height, $H_{predicted}$, that must always be greater than the design height of the 3DCP structure for a stable printing, implying vertical building rate does not intersect with shear capacity build-up curve of the material. A stable 3DCP structure can be designed without global failure by controlling the user-defined printing parameters such as filament layer height for structural integrity or aesthetics or printing speed and print path for construction time optimisation. Since 3DP-LWFC generally shows low yield stresses and poor buildability compared to normal weight concrete, a slower printing speed, 40 mm/s or lower, and longer printing path, 8000 mm or longer, are used to design and produce façade structures that do not collapse on the printer bed during construction.

4.3 Results and Discussion

4.3.1 Setting time

Fig. 4.3 shows the Vicat penetration measurements of TD-10 and TD-14 for initial and final setting time determination. It must be mentioned that hardened TD-7 can be crumbled merely by hand even after 24 hours of ageing. Furthermore, the needle entirely penetrates through the height of the porous TD-7 specimen at the completely hardened state. Thus, the conventional Vicat penetration instrument cannot measure the setting time of TD-7, and an alternative method, namely heat of hydration measurement (Hu *et al.*, 2014), is encouraged.

Density measurements and several fractions of the samples are specified in Table 4.4. Water content and water-to-binder ratios are in a small range, but the varying foam volume fraction produces the different densities. This foam volume fraction difference explains the setting time difference between TD-14 and TD-10, with both initial and final setting times of TD-14 roughly half those of TD-10, while the incorporated foam volume of TD-10 is double that of TD-14. It is postulated that the higher foam volume creates greater interstitial distance between cement grains during hydration, which weakens the attractive forces in the matrix despite the rapid early hydration forming rate from CSA cement. However, it must be mentioned that the lesser solid content of TD-10 would have led to the same effect for the TD-7 result for which complementary research is required to validate the postulation. This result of TD-14 shows profoundly shortened initial setting time (180 min) compared to the same mix design LWFC without CSA reported by the same author (390 min) (Cho *et al.*, 2019). This result is comparable to the setting time of 3D printable normal weight concrete without accelerator chemical additives, reported to have initial and final setting times of 210 min and 430 min respectively (Moelich *et al.*, 2020).

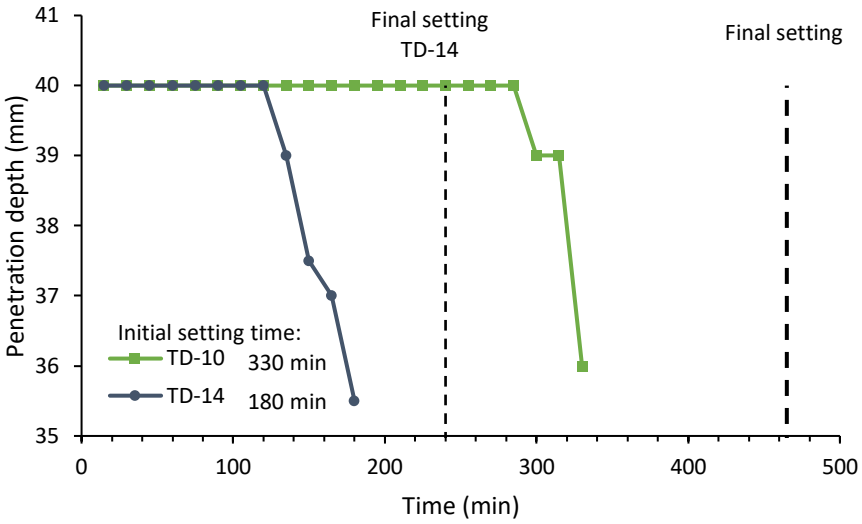

Fig. 4.3 Vicat penetration setting time measurement

Table 4.4 LWFC constituent ratios and density measurement

	ρ_{base} (kg/m^3)	ρ_{wet} (kg/m^3)	ρ_{mature} (kg/m^3)	Water content	w/binder	V_{foam} (%)
TD-7	1776.0	704.8	655.9	24.2%	0.385	62.6%
TD-10	1761.7	1001.6	951.7	24.4%	0.371	45.1%
TD-14	1784.0	1397.8	1346.0	24.5%	0.362	21.7%

4.3.2 Rheometer measurement

Initial CSR test results of three samples are plotted in Fig. 4.4 (a) Initial CSR test plot over three samples; (b) Unitless normalised shear stress to imposed stress(a), showing the initial static and dynamic yield stresses. The freshly extruded layer material has experienced shearing through the pumping process; thus, the material capacity immediately after extrusion is considered to be the initial dynamic yield stress. The critical layer, the bottom-most layer, is subjected to the weight induced vertically by the printed height *h*, causing vertical stress of $\sigma = \rho \cdot g \cdot h$. The material must bear the load and retain the desired shape to be considered constructable. As discussed earlier, the normal stress needs to be converted with a strength correction factor, as shear failure governs fresh concrete. Thus, the initial imposed shear stress is defined as $\tau_{impose,i} = \sigma_1/2 \cdot F_{AR}$.

The initial imposed shear stress for three samples with density difference is calculated based on the buildability model parameters, i.e. 10 mm layer height (*h*) and 1.7 strength correction factor (F_{AR}) for the aspect ratio of 0.33 for the printed filament. This corresponds to imposed shear stress due to gravity of 20.2 Pa, 28.9 Pa, and 40.4 Pa for the first (single) layer of TD-7, TD-10, and TD-14, respectively. From the obtained result, the material shear capacities, in which initial dynamic yield stress is a relevant parameter to compare, are significantly higher than the hypothetical imposed stress, thus sound shape retention is expected for all samples at the first layer. It is acknowledged that this argument entails

strength and resistance to plastic yielding resulting in flow, and does not consider the fresh concrete stiffness, which allows finite layer deformation.

The density of printing material is the source of the imposed stress; thus, it is worthwhile to investigate the proportionality between the initial material shear capacity and the initial imposed stress of each test set. The initial CSR test responsive curve is normalised to the imposed shear stress, defined as $\tau_{material,i}/\tau_{impose,i}$, and depicted in Fig. 4.4 (a) Initial CSR test plot over three samples; (b) Unitless normalised shear stress to imposed stress(b). This relative curve shows a different tendency than Fig. 4.4 (a) Initial CSR test plot over three samples; (b) Unitless normalised shear stress to imposed stress(a) in which TD-7 has a larger shear capacity margin against the applied stress even though the absolute static and dynamic yield stress values are slightly inferior to TD-10 mainly attributed to lower density and still good rheological performance.

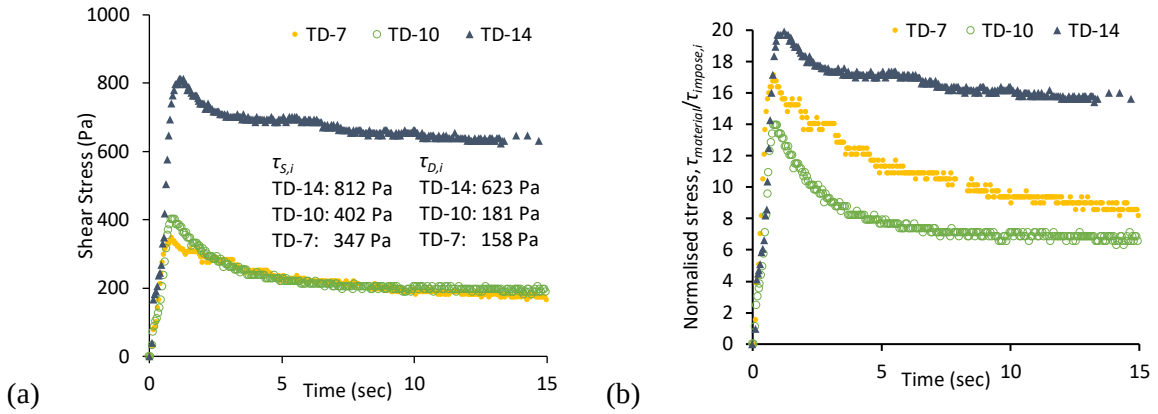

Fig. 4.4 (a) Initial CSR test plot over three samples; (b) Unitless normalised shear stress to imposed stress

The follow-up CSR tests over various resting time intervals are performed for thixotropic parameter determination. The full data set of CSR tests for three samples are plotted in Fig. 4.5. The curves clearly show a noticeable strength evolution over time of TD-10 and TD-14 while the stress growth rate of TD-7 is low. A bi-linear material strength evolution curve is plotted in Fig. 4.6 based on t_{rf}, R_{thix} and A_{thix} calculation according to Eq (4.10), and the determined results summarised in the graph. It must be mentioned that the static yield stress of 30 min resting interval is used for A_{thix} calculation, i.e. t = 30 min and $\tau_{S,30min}$ for all test sets.

The applied shear strain rate is first calculated, and shear strain for the data set is then calculated. The obtained shear strain is plotted against shear stress to analyse the stiffness development over time, $G(t)$, where $G = \tau / \gamma$. Fig. 4.7 is a partial stress-strain curve, $\tau(\gamma)$, clearly showing the constant gradient at the beginning of each graph which refers the linear elastic region corresponding elastic shear modulus as per (Ivanova & Mechtcherine, 2020; Nerella *et al.*, 2019). Elastic shear modulus evolution over time for all test sets can be seen in Fig. 4.8. Bingham model parameters are determined from flow curve tests with seven stress measurement points in between vane speeds of 0.5 rev/s and 0.05 rev/s, which

correspond to shear rates of 2.51 s^{-1} and 0.25 s^{-1}. A flow curve test result with torque measurement and vane speed is seen in Fig. 4.9 and converted dynamic yield stress and plastic viscosity are specified in the graph. The obtained results are summarised in Table 4.5.

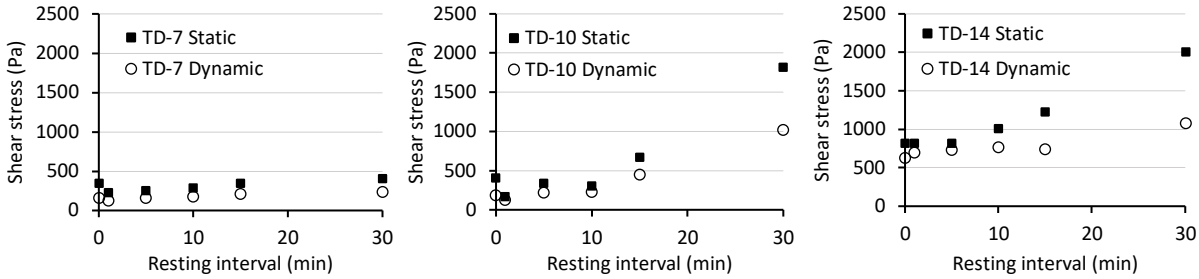

(a) TD-7 (b) TD-10 (c) TD-14

Fig. 4.5 Full set of the series of CSR tests for thixotropic parameter calculation

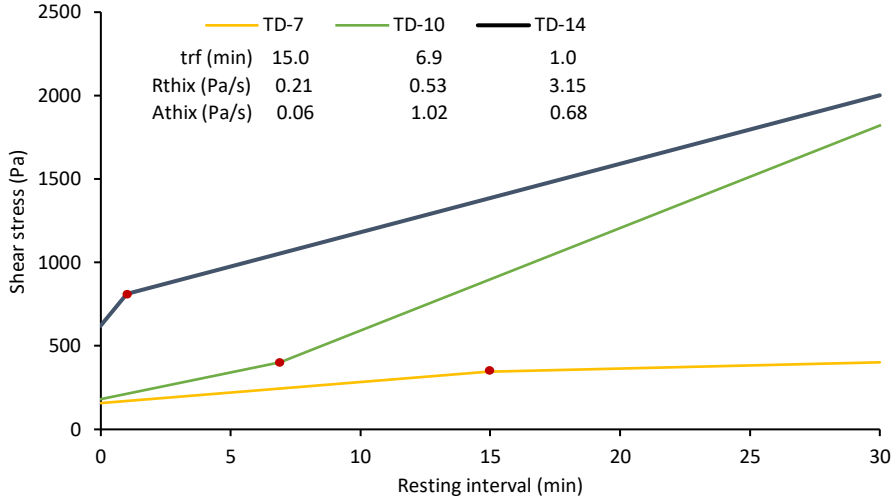

Fig. 4.6 Material strength evolution curve with thixotropic parameters, Rthix is dotted line, Athix is solid line and trf is red dot

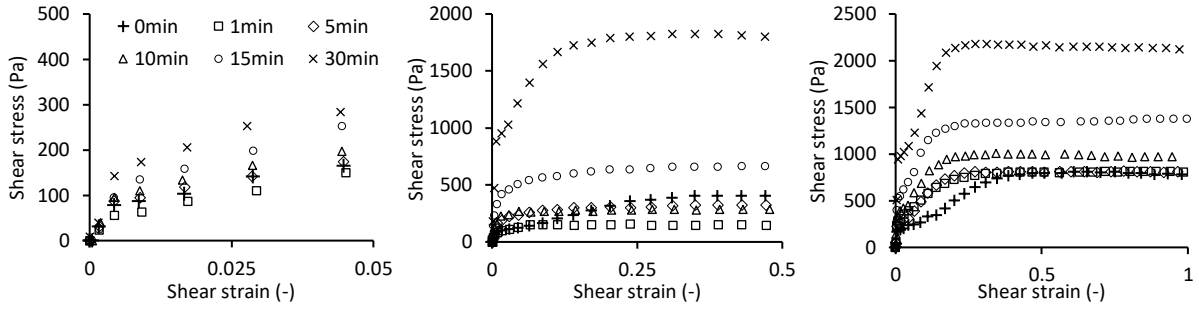

(a) TD-7 (b) TD-10 (c) TD-14

Fig. 4.7 Shear strain-shear stress graphs over various resting intervals

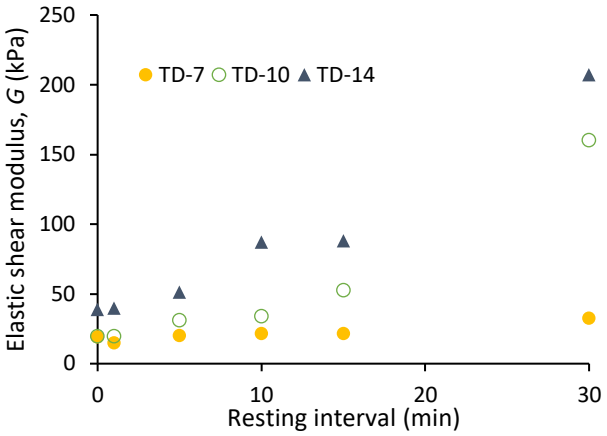

Fig. 4.8 Elastic shear modulus, *G*, evolution over resting interval

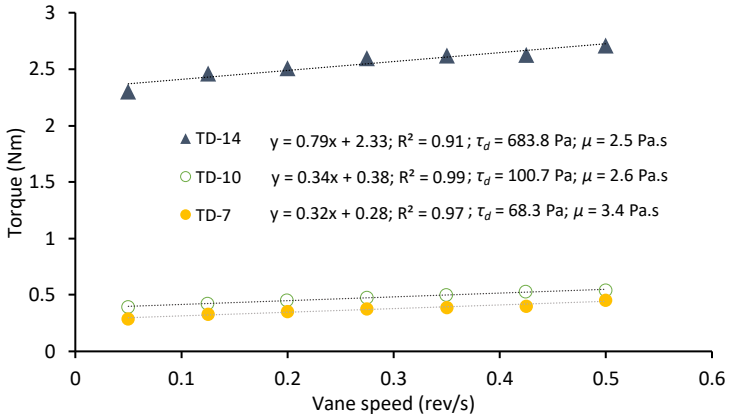

Fig. 4.9 Flow curve test result

Table 4.5 Rheological parameters of 3DP-LWFC

	$\tau_{S,i}$ (Pa)	$\tau_{D,i}$ (Pa)	$G_{,i}$ (kPa)	t_{rf} (min)	R_{thix} (Pa/s)	A_{thix} (Pa/s)	μ (Pa.s)
TD-7	346.79	157.63	19.31	15.00	0.21	0.06	3.4
TD-10	401.97	181.28	19.77	6.90	0.53	1.02	2.6
TD-14	811.82	622.65	38.76	1.00	3.15	0.68	2.5

The result obtained above shows that the higher density LWFC has higher rheological parameters except for viscosity. The mechanisms governing yield stress of LWFC are more complex than normal weight concrete due to the existence of more influencing factors and their inter-dependence, e.g. surfactant type, surfactant concentration, solid-bubble kinetics, among others (Feneuil *et al.*, 2019; Rosen & Kunjappu, 2012). It is postulated that the yield stress of LWFC is mainly attributed by the type and concentration of surfactant for foam production and base mix yield stress (Feneuil *et al.*, 2019). The former determines the physical and chemical properties of the foam bubble, such as adsorption amount and rate, deformability, bubble wall thickness, but this topic is beyond the scope of this paper. It is, thus, noted that a single surfactant type, protein-based foam agent, and constant surfactant solution

concentration are used throughout the study. The latter determines bubble size, size distribution, bubble mobility rate, etc., and is controlled by the base mix consistency as reflected by the slump flow diameter before foam insertion. Other than the aforementioned factors, the main attribution of the difference in rheological performance can be linked to foam volume fraction, or the solid particle volume fraction deviation.

The hydrophilicity and surface charges of cement grain lead to cement particle adsorption around oppositely charged bubbles, which mechanism separates individual bubbles. The amount and rate of adsorption and solid particle coagulation are promoted in a LWFC matrix with high solid particle volume ratio due to closer interstitial distance between solid particles having greater Van der Waals attraction, inversely proportional to the square of the interparticle distance, and lesser Born repulsion or electric double layer repulsion in molecular interaction (Butt *et al.*, 2003; Cheng, 1987). This is in agreement with a yield stress model of suspension, so-called Yodel, developed by (Flatt & Bowen, 2006) mentioning that the interparticle force is highly influenced by the distance between solid grains. Also, the lower density of LWFC with high foam volume fraction yields increased bubble size, as found by (Nambiar & Ramamurthy, 2007) which significantly lowers the interparticle force, and hence the yield stress. The liquid encaptured by the adsorbed surfactants in a bubble may be released at breakage, which subtly increases the liquid fraction, and the possibility is higher at high foam volume incorporation. Thus, it is postulated that the close distance solid particle network in a porous matrix allows a higher yield stress and better thixotropic behaviour (Kruger *et al.*, 2019b). Vice versa, a high foam volume fraction leads to low yield stress and a low yield stress evolution rate, as seen in the results above. The yield stresses of TD-14 for all resting intervals are recorded as the highest value. However, these values are considered as low compared to the normal weight 3D printable concrete for printing tall and slender structure (Kruger *et al.*, 2019a).

Profound thixotropic parameters, R_{thix} and A_{thix}, are found in TD-14 in which the same mix design, only without CSA cement, showed a constant or negative value of thixotropic parameters in the previous study due to cohesive nature of LWFC (Cho *et al.*, 2019). TD-10 shows uncommon build-up rates with $A_{thix} > R_{thix}$. A relatively high foam volume fraction of TD-10, more than double the V_f of TD-14, struggles to re-flocculate at the shorter resting interval similar to TD-7, but it is assumed to attain structural build-up rate rapidly by early hydration products attributed by CSA cement. Even though the discrepancy of structuration rate, A_{thix}, between TD-10 and TD-14 is not clearly understood, both results are comparable to normal weight 3D printable concrete with nanoparticle inclusion in a range of 0.61 – 1.17 Pa/s (Kruger *et al.*, 2019b).

Strain-stress graphs of all test sets show uptrending shear stiffness, or elastic shear modulus *G(t)*, over time as expected in (Roussel, 2018). This development is clearer for TD-14, while TD-10 and TD-7 struggles for the first four sets, i.e. up to 10 min resting intervals. The sudden surge of *G(30 min)* of TD-10 corresponds to the yield stress trend shown in Fig. 4.5 (b).

Fig. 4.9 shows a subtle variation in plastic viscosity, exhibiting an opposite trend than the previously discussed results. This result agrees with viscosity assessment of foamed cement by extended Stokesian dynamic simulation (Rosenbaum *et al.*, 2019). The study plotted relative viscosity against foam volume fraction with several model equations, and all are in agreement with increased viscosity with foam volume fraction either linearly or exponentially depending on the prediction model.

4.3.3 Slump flow table measurement

Table 4.6 shows the obtained slump flow results of a base mix as well as LWFC mix. This validates that the base mix of all the samples falls within the abovementioned controlled slump flow region.

Fig. 4.10 (a) shows a direct proportional relation between density and slump flow diameter while an inverse proportionality is observed between density and viscosity as discussed in Section 4.2.5. Dynamic yield stress-slump flow diameter and kinematic viscosity-slump flow diameter correlations can be seen in Fig. 4.10 (b) and (c), respectively. Both have a good tendency, but the latter correlation has a strong linear relation.

Table 4.6 Slump flow measurement results, Sb and Sf referring to base mix and foamed concrete slump flow, respectively

	S_b (mm)	S_f (mm)
TD-7	185	161
TD-10	192	164
TD-14	185	168

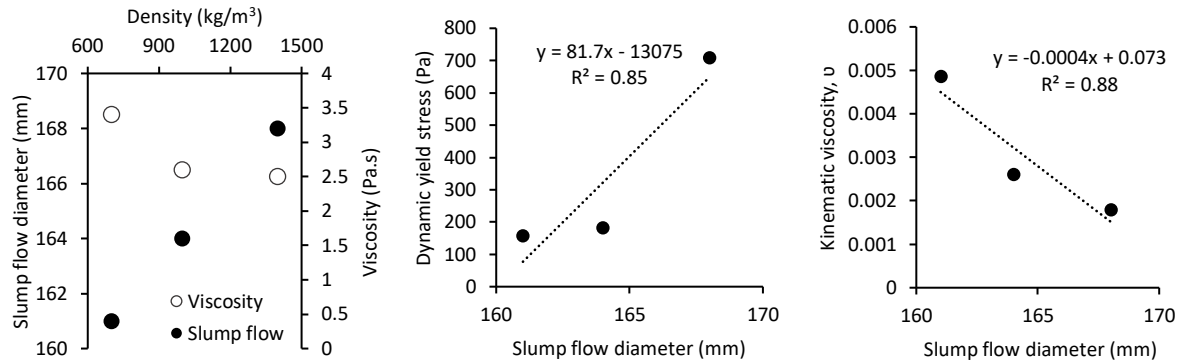

(a) (b) (c)

Fig. 4.10 (a) slump flow diameter and viscosity plot against density; (b) correlation between slump flow diameter and yield stress; and (c) kinematic viscosity plot against slump flow diameter

4.3.4 3D concrete printing

4.3.4.1 Buildability model

At the completion of rheological characterisation, material parameters can be substituted in the buildability model to predict the number of printable layers before plastic collapse. This allows calculating material-specific fixed gradient line which is the straight line from 0 to $\tau(t_{rf})$. The material-specific gradient is used to determine either R_{thix} or A_{thix} dependent buildability model equation by comparing to the building rate, i.e. the R_{thix}-based equation is used if building rate > material-specific fixed gradient line. Building rate calculations can be found in Kruger *et al.* (2019a). The calculated material-specific fixed gradient line and building rate are populated in the material thixotropic bi-linear graphs in Fig. 4.11. This graph shows that the R_{thix}-based equation is used for buildability prediction of TD-7 and TD-10 while the A_{thix}-based dependent equation is used for TD-14.

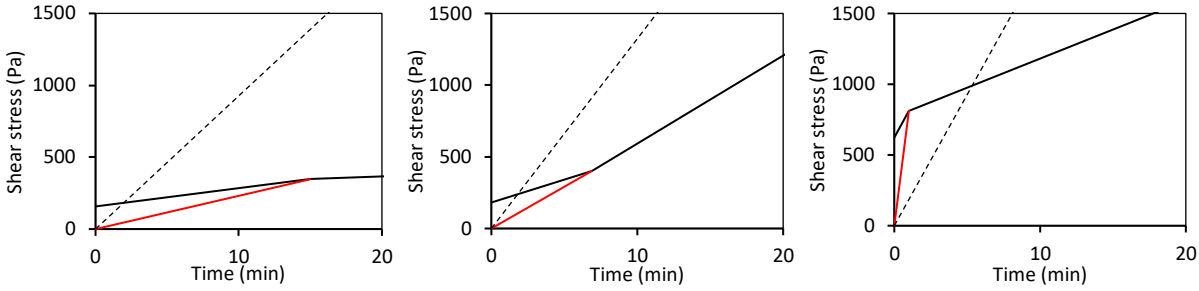

(a) TD-7 (b) TD-10 (c) TD-14

Fig. 4.11 Material yield stress evolution curve with building rate line (black dotted) and material-specific fixed gradient line (red solid)

Based on the input parameters, the number of printable layers is predicted to be 9 layers (1.7 min printing time), 8 layers (1.5 min printing time), and 24 layers (4.5 min printing time) for TD-7, TD-10 and TD-14, respectively. Actual 3D printed hollow column test results of all sets are depicted in Fig. 4.12. The first layer is shown to validate shape retention of the critical layer, i.e. the initially printed bottom-most layer, under its self-weight. As expected, limited deformation occurs in the first layer for all test sets. In the last image of each 3D printing object, plastic yield is observed, instead of elastic buckling failure as discussed in Section 4.1.

For TD-7, a large deformation is found at the transition between layer 7 and layer 8 which corresponds the error % of -22.2% to -11.1% in predicted constructed height before plastic collapse. TD-10 shows a sound buildability up to layer 8, and the bottom layers start to yield at layer 9, showing deformation which leads to complete collapse at layer 10. This results in an error % of 0% to +12.5%. Unlike previous results, TD-14 shows subtle deformations up to the point of collapse. Plastic yielding seems to initiate during printing of layer 15 and it causes a sagged global object, leading to the slightly thicker top layer 16 due to not adjusting the nozzle height accordingly. This test set results in the greatest

discrepancy error % of -41.7% to -37.5%. The large percentage range values are associated with the small denominator of each calculation, given the relatively low number of layers achieved at the adopted building rate. The number of buildable layer results validate the rheometer results in which higher density has better rheological performance. It is also worthwhile to mention that TD-14 shows the finest extruded filament throughout the printing whereas the porous filament of TD-7 yields below the standard surface finish. Nozzle technology and improved 3D printer system (e.g. robotic arm) are envisaged to improve the surface finish and geometric perfection in future work.

Providing the accuracy of this buildability model, within ± 20%, from the previous validation works (Cho *et al.*, 2020; Cho *et al.*, 2019; Kruger *et al.*, 2019a), this large discrepancy, ten fewer layers printed than the predicted model, is not a usual result and incompletely understood for the cause of inaccuracy other than a highly porous cementitious material might not yield the same shear failure, i.e. different strength correction factor. Thus, it is recommended a careful geometric design with printing parameter selection must be considered for this specific material.

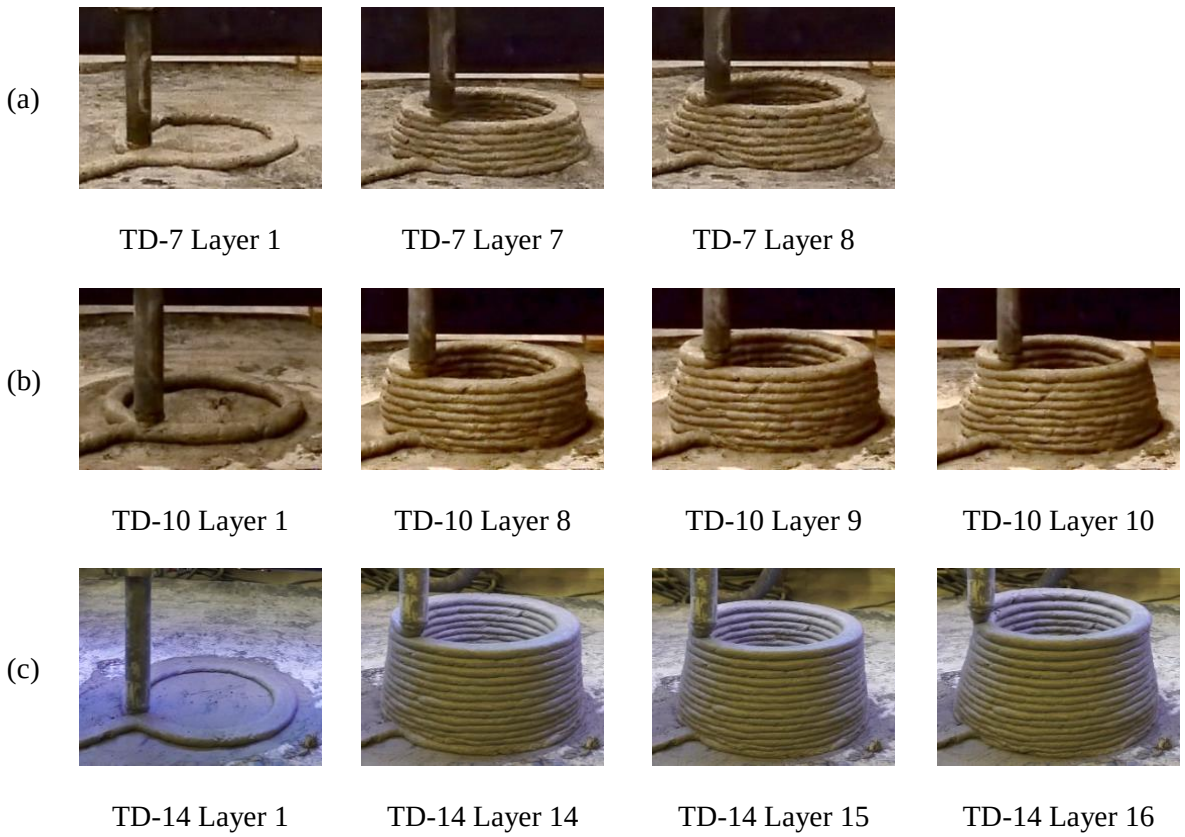

Fig. 4.12 Actual hollow column 3D printing showing the first layer and the layers in the vicinity of collapse

4.3.4.2 Buoyant façade structure 3D printing

The first trial for 3D printed façade element is a honeycomb patterned rectangular unit with the TD-7 mix. The 3D printed object is composed of rectilinear movement as per Fig. 4.13. In total 5 layers stacked for the outer perimeter, and 3 layers are printed for the inner pattern with 10 mm layer height.

Due to high porosity, the printed filament is porous which does not provide a good surface finish, and discontinuity of filament at some points occurred which reduce the structural integrity.

(a) (b) (c)

Fig. 4.13 (a) Closed loop print path profile with G-code coordinate; (b) and (c) 3D printed façade object with TD-7

Secondly, a system of parametric sine-wave equations describing complex harmonic motion is employed to design the façade element. A closed-loop curve, famously known as Lissajous figure (Palmer, Ridgway, Al-Rawi, *et al.*, 2011), is created by two sine functions, namely $x = A \cdot sin(a \cdot t + \theta)$ and $y = B \cdot sin(b \cdot t)$, in which the amplitude, frequency and phase angle offset determines the final geometry. The generated geometry is highly sensitive to the frequency ratio of a/b, and the geometry shown in Fig. 4.14 uses a = 4, b = 5 and θ = -57°. For this façade element, TD-10 is selected with 12.5 mm layer height and 40 mm/s printing speed. In total 6 layers are printed which corresponds to 75 mm in object height. The weight of the façade element is approximately 43 kg each in Fig. 4.14 (c).

(a) (b) (c)

Fig. 4.14 Lissajous figure façade element printing (a) print path; (b) after the completion of printing; and (c) façade element layout example

Based on the result above, the printability of LWFC is entitled, even for the density lower than a portable water implying a huge value in practical application. From the practical point of view, the buoyant construction material can expand the use not only on the ground, but on water like a floating house manufacturing. Appreciating the light weight and the geometric freedom in production, an aesthetically pleasing and customisable modular-basis façade element which can be installed as cladding outside of buildings will be the most viable and practical application for 3DP-LWFC although an improvement is

inevitable in surface finish and printer control. Since TD-14 can be used for structural components (Dunn *et al.*, 2018) and has notable constructability, sustainable residential housing construction can be achieved with LWFC.

4.4 Conclusions

Rheological assessment and 3D printability of a novel and sustainable cementitious material, LWFC, has been studied in many aspects, namely yield stress, thixotropic parameters, elastic shear modulus and viscosity, through various tests in this work. A wide range in density (700 – 1400 kg/m^3) samples with large foam volume fraction deviation are investigated and TD-10 and TD-14 showed promising thixotropic behaviour and 3D printability. Different forms of façade elements have been designed and produced by additive manufacturing to propose a practical application. Buoyant façade elements ease handling, installing and self-weight induced loading to the parental structure. The findings are as follows:

- Foam volume fraction significantly influences rheological properties of LWFC, attributed to the physics of attraction on nano- and microstructural level and the larger interstitial separation caused by increased foam content.
- TD-14 (V_f = 21.7%) records the highest initial yield stress and elastic shear modulus which are up to double those of the other test sets (V_f = 62.6% and 45.1% for TD-7 and TD-10, respectively).
- TD-14 shows short re-flocculation time, 1 min, leading to profoundly high R_{thix} value for foamed concrete particularly.
- TD-7 records the highest viscosity which validates many prediction models saying high foam volume fraction results in high viscosity.
- A good linear regression model has been found between kinematic viscosity and the slump flow diameter.
- Accuracy of the buildability model may be questioned due to the high discrepancy in the outcome of TD-14 (-41.7%), but the rest showed good agreement.

Declaration of competing interest

None.

CRediT authorship contribution statement

Seung Cho: Conceptualisation, Data curation, Methodology, Formal analysis, Validation, Writing – original draft, Visualisation, Investigation. **Jacques Kruger**: Conceptualisation, Validation, Methodology, Writing – review & editing. **Algurnon van Rooyen**: Conceptualisation, Supervision,

Writing – review & editing. **Gideon van Zijl**: Conceptualisation, Supervision, Writing – review & editing, Project administration, Funding acquisition.

Acknowledgements

Cathay Industries (Africa) is acknowledged for providing CSA cement. The research is supported by The Concrete Institute in South Africa.

4.5 References

Abd, M. & Hillemeier, B. 2014. Combined effect of fine fly ash and packing density on the properties of high performance concrete : An experimental approach. *Construction and Building Materials*. 58:225–233.

Ahmed, R.M., Takach, N.E., Khan, U.M., Taoutaou, S., James, S., Saasen, A. & Godøy, R. 2009. Rheology of foamed cement. *Cement and Concrete Research*. 39(4):353–361.

Andrew, R.M. 2019. Global CO2 emissions from cement production, 1928-2018. *Earth System Science Data*. 11(4):1675–1710.

ASTM International. 2008. ASTM C230/C230M Standard specification for flow table for use in tests of hydraulic cement.

ASTM International. 2015. ASTM C1437-15 Standard test method for flow of hydraulic cement mortar.

Bong, S.H., Nematollahi, B., Nazari, A., Xia, M. & Sanjayan, J. 2019. Method of optimisation for ambient temperature cured sustainable geopolymers for 3D printing construction applications. *Materials*. 12(6):902.

Buswell, R.A., Leal de Silva, W.R., Jones, S.Z. & Dirrenberger, J. 2018. 3D printing using concrete extrusion: A roadmap for research. *Cement and Concrete Research*. 112:37–49.

Butt, H.J., Graf, K. & Kappl, M. 2003. *Physics and Chemistry of Interfaces*. Wiley Online Books.

Chen, Y., li, Z., Chaves Figueiredo, S., Çopuroğlu, O., Veer, F. & Schlangen, E. 2019. Limestone and calcined clay-based sustainable cementitious materials for 3D concrete printing: A fundamental study of extrudability and early-age strength development. *Applied Sciences*. 9:1809.

Cheng, D.C.-H. 1987. Thixotropy. *International Journal of Cosmetic Science*. 9(4):151–191.

Cho, S., Kruger, J., van Rooyen, A., Zeranka, S. & van Zijl, G. 2019. Rheology of 3D printable lightweight foam concrete incorporating nano- silica, in *Rheology and Processing of Construction Materials*. Springer International Publishing: 373-381.

Cho, S., Kruger, J., Zeranka, S. & van Zijl, G. 2019. 3D Printing concrete technology and mechanics. *Concrete Beton Technical Journal*. (158). [Online], Available: https://concretesociety.co.za/images/stories/publications/cb-issue-158.pdf.

Cho, S., Kruger, J., Bester, F., van den Heever, M., van Rooyen, A. & van Zijl, G. 2020. A compendious rheo-mechanical test for printability assessment of 3D printable concrete, in *Second RILEM International Conference on Concrete and Digital Fabrication*. Springer International Publishing: 196-205.

de Villiers, J.P., van Zijl, G.P.A.G. & van Rooyen, A.S. 2017. Bond of deformed steel reinforcement in lightweight foamed concrete. *Structural Concrete*. 18(3):496–506.

Dunn, T.P.A., van Zijl, G.P.A.G. & van Rooyen, A.S. 2018. Investigating a reinforced lightweight foamed concrete walling system for low-rise residential buildings in moderate seismic regions. *Journal of Building Engineering*. 20:663–670.

Engmann, J., Servais, C. & Burbidge, A.S. 2005. Squeeze flow theory and applications to rheometry: A review. *Journal of Non-Newtonian Fluid Mechanics*. 132(1):1–27.

European Standard. 2016. BS EN 196-3:2016 - Methods of testing cement. Determination of setting times and soundness.

Falliano, D., De Domenico, D., Ricciardi, G. & Gugliandolo, E. 2020. 3D-printable lightweight foamed concrete and comparison with classical foamed concrete in terms of fresh state properties and mechanical strength. *Construction and Building Materials*. 254:119271.

Falliano, D., Crupi, G., De Domenico, D., Ricciardi, G., Restuccia, L., Ferro, G. & Gugliandolo, E. 2020. Investigation on the rheological behavior of lightweight foamed concrete for 3D printing applications. in *Second RILEM International Conference on Concrete and Digital Fabrication*. Springer International Publishing:246–254.

Feneuil, B., Roussel, N. & Pitois, O. 2019. Yield stress of aerated cement paste. *Cement and Concrete Research*. 127:105922.

Flatt, R. & Bowen, P. 2006. Yodel: A yield Stress model for suspensions. *Journal of the American Ceramic Society*. 89(4): 1244-1256.

Hu, J., Ge, Z. & Wang, K. 2014. Influence of cement fineness and water-to-cement ratio on mortar early-age heat of hydration and set times. *Construction and Building Materials*. 50:657–663.

Ivanova, I. & Mechtcherine, V. 2020. Possibilities and challenges of constant shear rate test for evaluation of structural build-up rate of cementitious materials. *Cement and Concrete Research*. 130:105974.

Jayathilakage, R., Rajeev, P. & Sanjayan, J.G. 2020. Yield stress criteria to assess the buildability of 3D concrete printing. *Construction and Building Materials*. 240:117989.

Jones, M. & McCarthy, A. 2005a. Preliminary views on the potential of foamed concrete as a structural material. *Magazine of Concrete Research*. 57:21–31.

Jones, M.R. & McCarthy, A. 2005b. Utilising unprocessed low-lime coal fly ash in foamed concrete. *Fuel*. 84(11):1398–1409.

Jones, M.R., Zheng, L. & Ozlutas, K. 2016. Stability and instability of foamed concrete. *Magazine of Concrete Research*. 68(11):542–549.

Jones, M.R., Ozlutas, K. & Zheng, L. 2017. High-volume, ultra-low-density fly ash foamed concrete. *Magazine of Concrete Research*. 69(22):1146–1156.

Kearsley, E. & Mostert, D. 2005. Designing mix composition of foamed concrete with high fly ash contents. in *Use of Foamed Concrete in Construction* (Conference Proceedings). Thomas Telford Publishing. 29–36.

Kearsley, E.P. & Wainwright, P.J. 2001. The effect of high fly ash content on the compressive strength of foamed concrete. *Cement and Concrete Research*. 31(1):105–112.

Kruger, J., Zeranka, S. & van Zijl, G. 2019a. 3D concrete printing: A lower bound analytical model for buildability performance quantification. *Automation in Construction*. 106:102904.

Kruger, J., Zeranka, S. & van Zijl, G. 2019b. An ab initio approach for thixotropy characterisation of (nanoparticle-infused) 3D printable concrete. *Construction and Building Materials*. 224:372–386.

Kruger, J., Zeranka, S. & van Zijl, G. 2020. A rheology-based quasi-static shape retention model for digitally fabricated concrete. *Construction and Building Materials*. 254:119241.

Kruger, J., Cho, S., Zeranka, S., Barnardo Viljoen, C. & van Zijl, G. 2020. 3D concrete printer parameter optimisation for high rate digital construction avoiding plastic collapse. *Composites Part B Engineering*. 183:107660.

Laskar, A.I. & Bhattacharjee, R. 2011. Torque–speed relationship in a concrete rheometer with vane geometry. *Construction and Building Materials*. 25(8):3443–3449.

Le, T., Austin, S., Lim, S., Buswell, R.A., Gibb, A. & Thorpe, A. 2012. Mix design and fresh properties for high-performance printing concrete. *Materials and Structures*. 45:1–12.

Markin, V., Nerella, V.N., Schröfl, C., Guseynova, G. & Mechtcherine, V. 2019. Material design and performance evaluation of foam concrete for digital fabrication. *Materials*. 12(15).

Markin, V., Ivanova, I., Fataei, S., Reissig, S. & Mechtcherine, V. 2020. Investigation on structural build-up of 3D printable foam concrete. in *Second RILEM International Conference on Concrete and Digital Fabrication*. Springer International Publishing: 301–311.

Mechtcherine, V., Bos, F.P., Perrot, A., da Silva, W.R.L., Nerella, V.N., Fataei, S., Wolfs, R.J.M., Sonebi, M., et al. 2020. Extrusion-based additive manufacturing with cement-based materials – Production steps, processes, and their underlying physics: A review. *Cement and Concrete Research*. 132:106037.

Moelich, G., Kruger, J. & Combrinck, R. 2020. Plastic shrinkage cracking in 3D printed concrete. *Composites Part B: Engineering*. 200:108313.

Mose, M.P. & Perumal, D. 2016. Latest advances in alternative cementations binders than portland cement. *IOSR Journal of Mechanical and Civil Engineering*. 13:45–53.

Nambiar, E. & Ramamurthy, K. 2008. Fresh state characteristics of foam concrete. *Journal of Materials in Civil Engineering*. 20(2):103-111.

Nambiar, E.K.K. & Ramamurthy, K. 2006. Influence of filler type on the properties of foam concrete. *Cement and Concrete Composites*. 28:475–480.

Nambiar, E.K.K. & Ramamurthy, K. 2007. Air-void characterisation of foam concrete. *Cement and Concrete Research*. 37(2):221–230.

Nerella, V.N., Beigh, M.A.B., Fataei, S. & Mechtcherine, V. 2019. Strain-based approach for measuring structural build-up of cement pastes in the context of digital construction. *Cement and Concrete Research*. 115:530–544.

Palmer, K., Ridgway, T., Al-Rawi, O., Johnson, I. & Poullis, M. 2011. Lissajous figures: an engineering tool for root cause analysis of individual cases--a preliminary concept. *The journal of extra-corporeal technology*. 43(3):153–156.

Panda, B., Paul, S.C., Hui, L.J., Tay, Y.W.D. & Tan, M.J. 2017. Additive manufacturing of geopolymer for sustainable built environment. *Journal of Cleaner Production*. 167:281–288.

Panda, B., Lim, J.H. & Tan, M.J. 2019. Mechanical properties and deformation behaviour of early age concrete in the context of digital construction. *Composites Part B: Engineering*. 165:563–571.

Paul, S.C., van Rooyen, A.S., van Zijl, G.P.A.G. & Petrik, L.F. 2018. Properties of cement-based composites using nanoparticles: A comprehensive review. *Construction and Building Materials*. 189:1019–1034.

Perrot, A., Rangeard, D. & Pierre, A. 2015. Structural built-up of cement-based materials used for 3D-printing extrusion techniques. *Materials and Structures*. 49:1213-1220.

Reiter, L., Wangler, T., Roussel, N. & Flatt, R. 2018. The role of early age structural build-up in digital fabrication with concrete. *Cement and Concrete Research*. 112:86-95.

van Rooyen, A.S. 2020. *Mechanics and durability of surface treated structural foamed concrete*. Published doctoral disseration, Stellenbosch University.

Rosen, M.J. & Kunjappu, J.T. 2012. *Surfactants and Interfacial Phenomena*. Wiley Online Books.

Rosenbaum, E., Massoudi, M. & Dayal, K. 2019. The influence of bubbles on foamed cement viscosity using an extended stokesian dynamics approach. *Fluids*. 4:166.

Roussel, N. 2006. A thixotropy model for fresh fluid concretes: Theory, validation and applications. *Cement and Concrete Research*. 36(10):1797–1806.

Roussel, N. 2018. Rheological requirements for printable concretes. *Cement and Concrete Research*. 112:76-85.

Roussel, N. & Lanos, C. 2003. Plastic fluid flow parameters identification using a simple squeezing test. *Applied Rheology*. 13:132–141.

South African National Standard. 2013. Cement - Part 1: Composition, specifications and conformity criteria for common cements.

Taylor, M., Tam, C. & Gielen, D. 2006. Energy efficiency and CO 2 emissions from the global cement industry energy efficiency and CO 2 emission reduction potentials and policies in the cement. in *IEA*. 4-5 September 2006, Paris.

Thrane, L., Pade, C., Nielsen, C., Jeknavorian, A., Schemmel, J. & Dean, S. 2010. Determination of rheology of self-consolidating concrete using the 4C-rheometer and how to make use of the results. *Journal of Astm International*. 7(1).

Vikan, H. & Justnes, H. 2007. Rheology of cementitious paste with silica fume or limestone. *Cement and Concrete Research*. 37(11):1512–1517.

Voigt, T., Mbele, J.-J., Wang, K. & Shah, S. 2010. Using fly ash, clay, and fibers for simultaneous improvement of concrete green strength and consolidatability for slip-form pavement. *Journal of Materials in Civil Engineering*. 22(2):196.

Yeo, D. & Gabbai, R.D. 2011. Sustainable design of reinforced concrete structures through embodied energy optimization. *Energy and Buildings*. 43(8):2028–2033.

Chapter 5

Nanotechnology for improved 3D concrete printing constructability

Jacques Kruger*, Seung Cho, Marchant van den Heever, Frederick Bester, Algurnon van Rooyen, Gideon van Zijl

Division for Structural Engineering and Civil Engineering Informatics, Stellenbosch University, 7600, South Africa

Reproduced and reformatted from an article submitted to the *ACI Materials Journal*.

Abstract

This paper investigates the application of nanotechnology in 3D concrete printing (3DCP), in particular for enhancing thixotropic material behavior, improving buildability or the vertical building rate, and the amelioration of typical 3DCP anisotropic mechanical properties. Two 3D printable cementitious materials are investigated in this study: 1) high-performance concrete (HPC) with respective nano-silica (nS) and silicon carbide (SiC) nanoparticle additions and 2) lightweight foamed concrete (LWFC) with nS addition. The results indicate a significant increase in thixotropic material behavior for the HPC at low nanoparticle dosages. The inclusion of SiC nanoparticles improved the HPC's buildability performance by 45%. The incorporation of 3% nS to the LWFC increased the static yield shear stress by up to 5 times, which is validated by the improved buildability performance. Hardened state mechanical properties improved for both cementitious materials and nanoparticle additions. Especially noteworthy is nanoparticles' favorable influence on the interlayer bond strength.

Keywords: 3D concrete printing; nanoparticles; rheology; thixotropy; buildability; mechanical properties; lightweight foamed concrete; high-performance concrete; interlayer bond strength

5.1 Introduction

Industry 4.0 technologies, such as 3D printing and nanotechnology, are revolutionizing several manufacturing sectors to improve productivity and quality, whilst mostly reducing costs. This research combines these two complementary technologies to further augment and amplify the prospects for mass adoption of 3D printing in the construction sector (Bos *et al.*, 2016). Nanoparticles are broadly defined as having diameters less than 100 nm, which results in their behavior being dominated by atomic, molecular and ionic interactions (Panneerselvam & Choi, 2014). Addition of these nanoparticles to concrete has been found to enhance several properties, including rheology and thixotropy (Kruger *et al.*, 2019a; Roussel, 2006), mechanical strengths (Said *et al.*, 2018) and durability (Paul *et al.*, 2018). These advantageous effects are primarily attributed to increased pozzolanic reactivity induced by nanoparticle addition (García-Taengua *et al.*, 2015). This research investigates the constructability and mechanical advantages of nanoparticle incorporation specifically into 3D printable concretes.

Two types of nanoparticles are investigated in this study, namely nano-silica (nS) and silicon carbide (SiC), by various weight percentage incorporations of cement mass. All nanoparticles are sourced from Nanostructured and Amorphous Materials in the USA (Nanostructured & Amorphous Materials, 2020). nS particles are commercially more available and economical than SiC and available in significantly smaller sizes. Hence, nS particles are employed in this study with the primary aim to improve material rheology (Senff *et al.*, 2009) and thixotropy, and ultimately, fresh state 3D concrete printing constructability. A study by Mahawish et al. (2017) found that addition of titanium carbide (TiC) to concrete significantly improves mechanical strength, more so than the addition of SiC. However, 5% SiC addition by cement mass still increased the mechanical properties of reference concrete up to threefold. Due to the TiC nanoparticles being exceptionally more expensive at the time of conducting this study, SiC nanoparticles were rather acquired, which is more affordable. Therefore, SiC nanoparticles is employed in this study with the primary aim to improve mechanical properties of hardened state concrete.

Two different reference 3D printable concretes are also investigated in this study, namely a high-performance concrete (HPC) and a lightweight foamed concrete (LWFC). The HPC is the standard 3D printing material employed at Stellenbosch University, demonstrating superior fresh and hardened state properties. The aim of adding nanoparticles to this concrete is to determine if a 3D printable HPC can further be improved, specifically for 3D printing application. In contrast, LWFC is a relatively new material where breakthrough developments (Jones & McCarthy, 2005; Kearsley & Mostert, 2005) have led to the possibility of structural application, at typical wet densities between 1200 and 1600 kg/m^3. With LWFC typically demonstrating high flowability under self-weight by nature, the main concern here is the printability and constructability performance of LWFC in 3D printing application. Although LWFC possesses lower mechanical properties than normal-weight concrete directly caused by the

incorporation of significantly high volumes of entrained air, the primary focus is not to increase the mechanical strength of LWFC (where a high strength-to-weight ratio is expected), but such a result is welcomed. Therefore, the aim of adding nanoparticles to this concrete is to determine if the constructability performance, with particular focus on buildability, can be enhanced. Only nS addition is considered in this case.

Initially, for both concretes and various nanoparticle additions, the rheological behavior is characterized using the bi-linear thixotropy model developed by Kruger et al. (2019a) that specifically pertains to 3D printable cementitious materials. Thereafter, the perceived rheological improvements are practically captured by performing buildability tests (Kruger *et al.*, 2019b). Hardened state mechanical properties, including compressive and flexural strengths and Young's modulus, are determined. Additionally, the influence of improved thixotropy via nanoparticle addition on the interlayer bond strength (Kruger & van Zijl, 2021) is investigated via four-point bending tests.

5.2 Research Significance

The addition of nanoparticles to 3D printable concrete materials may improve thixotropy behavior that will consequently aid the general 3D printing constructability process, namely pumpability, extrudability, filament shape retention and buildability. In the case of LWFC, buildability performance might be improved to an acceptable degree where the requirement for chemical accelerators is negated. In the case of HPC, higher vertical building rates might be achieved together with constructability optimization (Kruger *et al.*, 2020) without requiring chemical accelerators, which generally is detrimental towards obtaining mechanically strong interlayers. An added benefit of nanoparticle addition is the improved hardened state mechanical properties obtained at low dosages.

5.3 Experimental Procedure

Three cases are investigated in this research. Initially, nS particles are added to the HPC by 1, 2 and 3% (cement mass) dosages. Similarly, SiC particles are added to the HPC by 1, 2 and 3% cement mass dosages. Lastly, nS particles are added to LWFC by 2 and 3% cement mass dosages. The nS particles are mainly used to improve rheology behavior and hence, 3D printing constructability performance. These nanoparticles have a specific surface area (SSA) that is 16 times that of the SiC nanoparticles used in this study, due to them being twice as small in diameter. The SiC nanoparticles, on the other hand, possess greater mechanical properties and are envisaged to improve hardened concrete state mechanical properties. This section describes the experimental procedures followed in order to conduct all the material preparation and characterization tests.

5.3.1 Materials

The properties of the nS and SiC nanoparticles employed in this study are given in Table 5.1. The particles are used in powder form and added together with the other dry constituents before mixing. A modified polycarboxylate polymer superplasticizer (SP), Chryso Premia 310, is used to disperse the nanoparticles. Eleven different 3D printable concrete mixes are investigated in this study, seven HPCs given in Table 5.2 and four LWFCs given in Table 5.3 CEM II/A-L 52.5N cement is used containing between 6 and 20% limestone extender. The SCMs include Ulula Class S fly ash, which is equivalent to Class F according to ASTM C618 (2019), together with FerroAtlantica silica fume, mainly utilized for enhanced rheology properties. The aggregate is a locally mined fine Malmesbury sand that consists of a continuously graded particle size distribution and maximum particle size of 4.75 mm. Ordinary potable tap water is used. Polypropylene (PP) fibres, 6 mm in length and 40 µm in diameter, are added to the LWFC to enhance fresh state stiffness. The LWFC comprises of the fly ash and cement paste base mixed to a fluid consistency, which is subsequently combined and thoroughly mixed with precursor foam of density 75 kg/m^3 made from a protein-based foam agent solution, FoamTech, with a water-solution dilution ratio of 1:40 and ferrous sulfate as a stabilizer with a dilution water-powder ratio of 1:80. By the addition of pre-mixed and predetermined amounts of foam, the target wet densities of 1400±50 kg/m^3 and 1600±50 kg/m^3 investigated in this paper are achieved. These wet densities relate to dry densities of roughly 1230 and 1450 kg/m^3, which have been shown to be applicable for structural use as load-bearing walls in buildings (Dunn *et al.*, 2018; de Villiers *et al.*, 2017). Current work on 3D printable LWFC of wet densities between 700 and 1000 kg/m^3 for load-bearing low-rise structural walling is advancing and to be reported in a future publication.

Table 5.1 Silica and Silicon Carbide nanoparticles' material properties (Nanostructured & Amorphous Materials, 2020)

	Silica (nS)	Silicon Carbide (SiC)
Purity	99.5 %	97.5 %
Average Particle Size (APS)	15 – 20 nm	45 – 55 nm
Specific Surface Area (SSA)	640 m^2/g	35 – 40 m^2/g
Color	White	Dark Grey
Morphology	Spherical	Spherical
Bulk Density	0.1 g/cm^3	0.068 g/cm^3
True Density	2.2 – 2.6 g/cm^3	3.22 g/cm^3
Synthesis Method	-	Plasma CVD

Table 5.2 Reference HPC mix and nanoparticle mixes' constituents and quantities

Mix name	Mixture constituents and quantities (kg)							
	Cement	Sand	Fly Ash	Silica Fume	Water	SP	nS	SiC
HPC_ref	579	1167	165	83	261	12.2	-	-
HPC_nS1	573.2	1167	165	83	261	12.2	5.8	-
HPC_nS2	567.4	1167	165	83	261	12.2	11.6	-
HPC_nS3	561.6	1167	165	83	261	12.2	17.4	-
HPC_SiC1	573.2	1167	165	83	261	12.2	-	5.8
HPC_SiC2	567.4	1167	165	83	261	12.2	-	11.6
HPC_SiC3	561.6	1167	165	83	261	12.2	-	17.4

Table 5.3 Reference LWFC mix and nanoparticle mixes' constituents and quantities

Mix name	Wet density (kg/m^3)	Mixture constituents and quantities (kg)					
	Pre-post 3DP	Cement	Fly Ash	Water	PP	Foam	nS
LWFC_ref	1 410-Not Measured	506.2	506.2	369.6	4.1	18	-
LWFC_nS2	1 435-1 445	506.2	506.2	369.6	4.1	18	11.6
LWFC_nS3	1 445-1 461	506.2	506.2	369.6	4.1	18	17.4
LWFC_nS2_new*	1 648-1 720	524.8	524.8	330.6	4.1	19.8	11.6

* Adjusted mix to reduce the total water content

5.3.2 Rheology characterisation

To capture thixotropy behavior pertaining to 3D printing of concrete, the bi-linear thixotropy model developed by Kruger et al. (2019a) is employed in this study. The model distinguishes between short term re-flocculation (R_{thix}), which is a physical, interparticle force equilibrium process, and long term structuration (A_{thix}), which is a chemical process mostly grounded in hydration kinetics. Higher R_{thix} values indicate increased thixotropy behavior, whereas higher A_{thix} values imply reduced settings time of the material. Furthermore, lower dynamic yield shear stresses ($\tau_{D,i}$) are favorable for pumping of a material, whereas higher static yield shear stresses ($\tau_{S,i}$) improves 3D printing buildability. Fig. 5.1 depicts the bi-linear static yield shear stress evolution model employed in this research to quantify material rheology.

This model is developed using data obtained from multiple stress growth tests conducted at various resting time intervals with the Germann ICAR rheometer (2020; Kruger *et al.*, 2019a). A shear rate of 1/s is employed for the HPC rheometry testing, which is the approximate shear induced by the concrete

pump during 3D printing. The LWFC that typically is much more viscous, is tested at a shear rate of 0.124/s due to the lower 3D printing speed employed in the buildability test, thus yielding reduced pump speed and pressure. For both materials, a stress growth test duration of 60 seconds is employed. By plotting the recorded $\tau_{S,i}$, $\tau_{D,i}$, R_{thix} and A_{thix} values, the bi-linear static yield shear stress evolution curve is obtained, as depicted in Fig. 5.1.

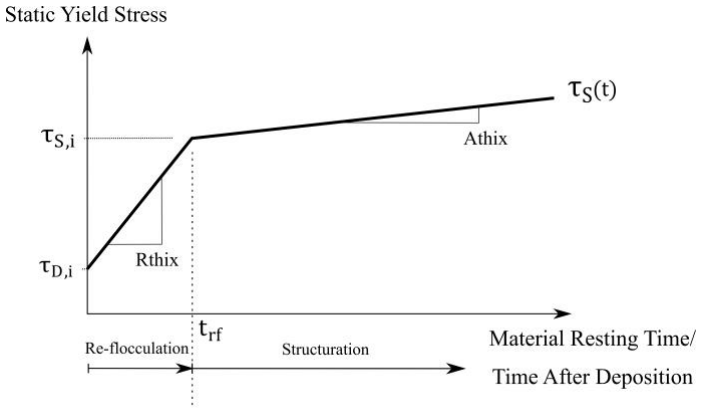

Fig. 5.1 Bi-linear static yield shear stress evolution model pertaining to 3D printing of concrete rheology quantification(Kruger *et al.*, 2019a)

5.3.3 Buildability performance characterisation

Buildability in terms of 3D printing of concrete refers to the number of filament layers that can be deposited onto one another in a successive manner without excessive deformation occurring that could result in in-print collapse (Kruger *et al.*, 2019b). The higher the total build height and vertical building rate, the better the buildability performance. Failure typically occurs due to either plastic yielding (material) or elastic buckling (instability) (Wolfs & Suiker, 2019). In order to solely focus on material plastic yielding, long straight elements must be avoided and element geometry selected such that near equal moment of inertias are obtained about all axes, in which case a circular hollow column is widely employed (Suiker *et al.*, 2020). For this research, a 250 mm diameter circular hollow column is printed at 60 mm/s nozzle speed, 10 mm deposition and layer height obtained from a 25 mm diameter circular nozzle, yielding a layer width of approximately 35 mm. Due to the LWFC being more flowable than the HPC, thus expecting significantly less comparative buildability, a print speed of 40 mm/s is employed to achieve failure at a higher number of layers. This yields a vertical building rate of 0.05 m/min for the HPC and 0.03 m/min for the LWFC. For all buildability tests, a column is printed until failure occurs and the total number of deposited layers achieved at failure captured.

5.3.4 Mechanical properties characterisation

The mechanical properties of 3D printable mixes are determined via conventional casting and testing methods. Printed samples are not considered as the interlayer bond significantly contributes to the overall strength observed in various testing directions, which is not ideal for comparative purposes. The

mechanical properties considered are the compressive and flexural strength, as well as Young's modulus characterisation. At least three specimens were tested for each mechanical property and 3D printable material combination. Note that, in the case of the LWFC, only LWFC_ref and LWFC_nS2 are considered (see Table 5.3) for mechanical testing, due to the limited total available amount of nanoparticles, justified by the focus on rheology. Concrete testing ages include 1, 7, 28 and 56-days for the HPC mixes and 14 and 28-days for the LWFC. Altogether, a total of at least 274 specimens were tested. All specimens are initially cured at laboratory conditions while still in the molds; however, a day after casting all specimens are demolded and cured in water at 23±2°C until their respective concrete testing ages are reached.

The flexural and compressive strengths are characterized according to EN 196-1 (2016). Flexural specimens with dimensions 40x40x160 mm are tested in four-point bending, in order to ensure little to no shear is present where failure is expected to occur, i.e. pure bending behavior is investigated. The specimens are tested in a Zwick Z250 material testing machine. A span of 150 mm is employed with loading points (via rollers) spaced at 50 mm intervals. A vertical load is transferred to two rollers and onto the specimen at a rate of 50 N/s. After conducting the flexural tests, an undamaged 40x40 mm segment of the flexurally-tested prism half is tested in compression (EN 196-1, 2016). Platens of 40x40x10 mm are placed above and below the specimen for accurate load transfer onto the specimen. Specimens are uniaxially loaded at a rate of 2 400 N/s. The Young's modulus is determined according to ASTM C469-02 (2002). Cylindrical test specimens of 100 mm diameter and 200 mm height are circumferentially instrumented with three linear variable differential transducers (LVDTs) at 120° intervals, over a 70 mm gauge length. The testing is conducted in a 2 MN Contest press machine with a 2 MN loadcell and measurements captured via an HBM Spider8 data acquisition system. The specimens are uniaxially loaded up to 40 % of their ultimate compressive capacity for the Young's modulus determination.

5.3.5 Interlayer bond strength characterisation

The interlayer bond strength (IBS) is determined from 3D printed specimen loaded in four-point bending (EN 196-1, 2016) with filament layers oriented vertically (O-III) (Kruger & van Zijl, 2021), as depicted in Fig. 5.2. The IBS specimens with dimensions 40x40x160 mm are extracted via saw cutting from a 175x175x350 mm square hollow column. This column is printed at a nozzle speed of 60 mm/s, yielding layer heights and widths of 10 and 40 mm, respectively. Altogether, a pass time (i.e., the time between successive depositions of filament layers) of 12 s is obtained (Le *et al.*, 2012). Only the 28-day concrete testing age is considered in this case. Furthermore, only the mixes that yielded the best improvement in terms of thixotropy are considered due to the limited amount of nanoparticles available. The reduction in bond strength is determined using the following equation (Kruger & van Zijl, 2021):

$$S_R(\%) = \left(1 - \frac{S_{III}}{S_m}\right) \cdot 100 \tag{5.1}$$

with S_R the effective IBS reduction in % compared to the mold-cast specimens (S_m) and S_{III} the 3D printed elements' flexural strengths determined in the test series in O-III.

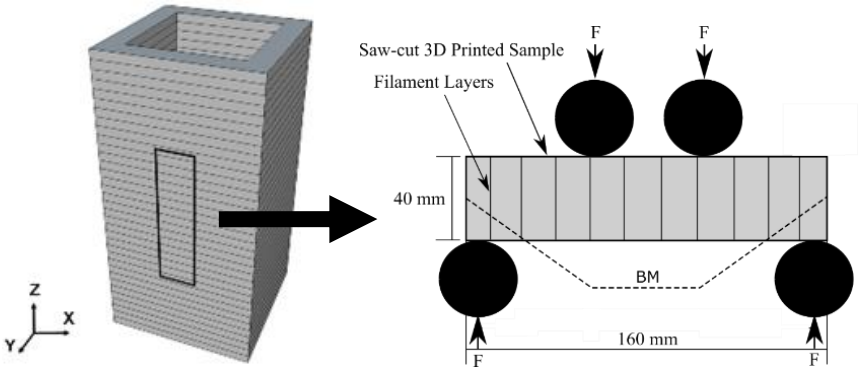

Fig. 5.2 A 3D printed 175x175x350 mm square hollow column from which the 40x40x160 mm IBS specimens are extracted and tested in four-point bending according to EN 196-1(EN 196-1, 2016)

5.4 Experimental Results and Discussion

5.4.1 High-performance 3D printable concrete

5.4.1.1 Static yield shear stress evolution & thixotropy

The static yield shear stress evolution curves for the HPC mixes containing nS and SiC nanoparticles are depicted in Fig. 5.3 and the respective model parameters given in Table 5.4. The same HPC reference mix was used for the SiC investigations as for the nS investigations; however, discrepancies are observed between the two listed reference HPC rheology properties. This is due to the SiC investigations being conducted at a different time period than that of the nS, and fresher constituent materials were used for the SiC investigations. A drastic increase in static yield stress is observed for the nS addition for every percentage increment. For 2% nS addition, a 100 % increase in static yield stress is observed from the reference mix. However, it was visually observed that the HPC_nS2 and HPC_nS3 mixes do not possess the required workability to be pumpable. One percent nS addition was found to increase the thixotropy, specifically R_{thix}, by 16 %. However, R_{thix} deteriorated for every percentage nS addition thereafter. A_{thix} reduced for every percentage increment of nS addition. The SiC nanoparticles significantly improved the rheology behavior of the HPC_ref* mix. In particular, a 149 and 141 % improvement in R_{thix} and A_{thix} was observed, respectively, for 1 % SiC addition. However, only a maximum of 30 % increase in static yield stress is obtained with SiC addition, compared to 137 % with nS addition. This is mainly ascribed to the SSA of the nanoparticles, of which the nS's SSA is more than 16 greater than that of the SiC nanoparticles. Consequently, larger water or SP dosage is required to disperse the (nano)particles and release entrapped water. Hence the drastic

increase in static yield stress observed by the nS addition. In the case of the SiC presenting less SSA, better dispersion of particles is obtained, which therefore does not significantly influence static yield stress. Instead, the tremendous number of dispersed nanoparticles contribute to the thixotropy mechanism, thus especially improving R_{thix}.

Table 5.4 HPC mixes' yield stresses and thixotropy parameters

	HPC ref	HPC nS1	HPC nS2	HPC nS3	HPC ref*	HPC SiC1	HPC SiC2	HPC SiC3
$\tau_{S,i}$ (Pa)	2 730	3 944	5 618	6 483	1545	1647	2007	1636
$\tau_{D,i}$ (Pa)	1 146	1 532	2 702	2 803	560	480	738	966
R_{thix} (Pa/s)	6.88	8	6.11	4.2	2.04	5.07	3.9	3.01
A_{thix} (Pa/s)	1.08	0.91	0.61	0.61	0.32	0.77	0.63	0.66

***** = The SiC investigations were performed at a different time than that of the nS investigations. Subsequently, this HPC reference mix exhibited dissimilar rheological characteristics than the exact HPC reference mix employed at the time of nS investigations.

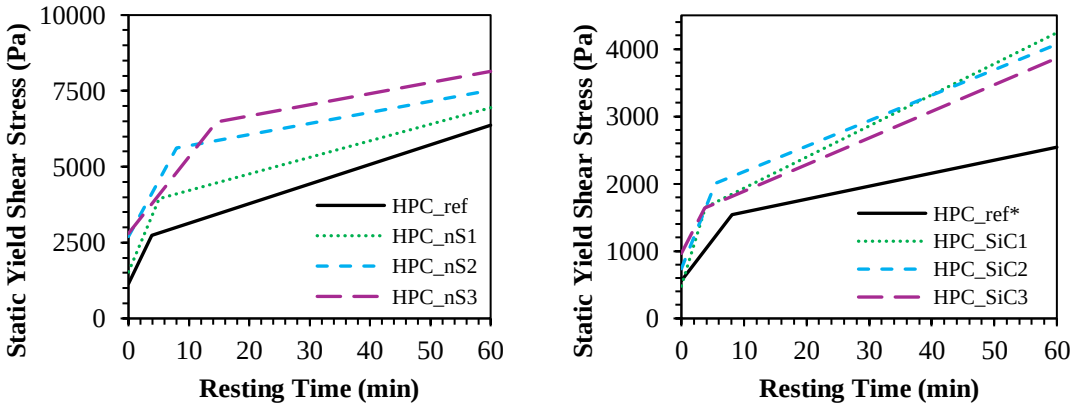

Fig. 5.3 Bi-linear static yield shear stress evolution curves for the nS and SiC HPC 3D printable mixes

5.4.1.2 Buildability performance

The circular hollow columns printed to assess the buildability performance of the HPC with nanoparticle inclusions are depicted in Fig. 5.4. The optimum nS addition for enhanced thixotropy and thus 3DCP constructability was found to be 1 %, based on the rheology results given in the previous section. For SiC, the optimum dosage was determined as 2 %, since not only high thixotropy is important for 3DCP, but also appropriate static yield stress. Therefore, HPC_nS1 and HPC_SiC2 were selected for the buildability validation prints and compared to their respective reference mixes, namely HPC_ref and HPC_ref*. Only these two nanoparticle mixes were considered due to the limited amount of particles available.

The HPC_ref mix attained a total build height of 540 mm (54 layers) before failure occurred, which is 13 layers less than that of the HPC_ref* mix (670 mm). Based on the bi-linear yield stress data, it was

expected that the HPC_ref mix would perform better than the HPC_ref* mix in the buildability test. The reason for this discrepancy is unknown. The HPC_nS1 mix attained a total build height of 590 mm, i.e. five filaments layers more than the HPC_ref mix. This result was expected based on the improved rheology properties enabled by the 1 % nS addition to the reference mix. The HPC_SiC2 attained a total build height of 970 mm, which is 300 mm or 30 filament layers more than the reference mix. This result was also expected based on the significant improvement that the 2 % SiC nanoparticle addition had on the rheology properties of the HPC_ref* mix. It is thus evident that improved rheology properties resulting from the optimum nanoparticle addition to concrete may significantly improve fresh state 3DCP constructability performance. In this research, SiC particles outperformed nS particles, but this may not always be the case. Likewise, the dosages employed in this research may not be the universal optimum for all 3D printable concrete mixes. However, with experimentation, slight nanoparticle addition may significantly improve 3DCP buildability performance, thereby reducing the likelihood of requiring chemical accelerators in 3D printing (which is detrimental towards obtaining adequate interlayer bond strength (Dressler *et al.*, 2020)).

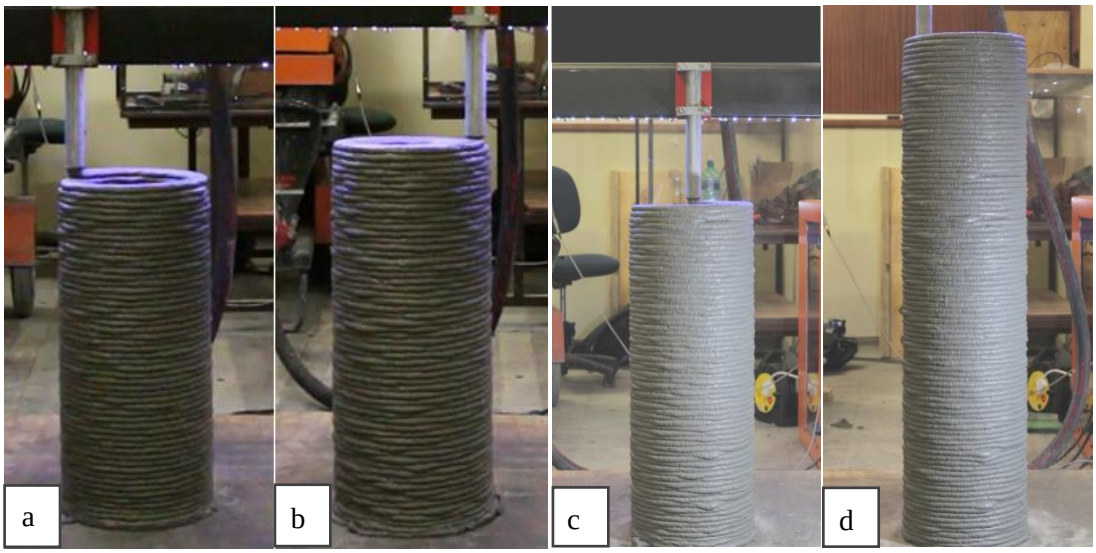

Fig. 5.4 Buildability performance quantification via printing a circular hollow column for a) the HPC_ref vs b) HPC_nS1, and c) the HPC_ref* vs d) HPC_SiC2

5.4.1.3 Compressive strength and Young's modulus

The compressive strength and Young's modulus of the respective HPC mixes are given in Table 5.5. It is evident that nS addition significantly improved the 1-day concrete age compressive strengths, with more than a 100 % increase obtained for 1 % nS addition. In contrast, SiC addition was found to reduce the 1-day compressive strengths, with 3 % SiC being the exception. Therefore, nS addition can be said to increase the early hydration rate of concrete. Furthermore, nS addition may be advantageous for early lifting and handling of large 3D printed concrete elements, thereby potentially improving turnaround time in factory environments. At 28-days concrete age, SiC addition generally performed better than

nS addition by increasing the average compressive strength of the reference HPC by 10 MPa to 80 MPa, for 1 to 3 % nanoparticle additions; a likely result of a densified microstructure and the mechanical capacity of the SiC nanoparticles. 1 % nS addition yielded the best overall improvement. However, at larger nS dosages only slight compressive strength improvements were observed. In the long term, i.e. 56-days concrete age, nS addition significantly reduced the reference HPC compressive strength by up to 20 MPa at 3 % dosage. Therefore, short term compressive strength improvements via nS addition may come at the expense of long-term losses. In contrast, all percentages of SiC additions improved the 56-day compressive strength of the HPC mix by up to 4 MPa. This result was expected due to the superior mechanical properties of SiC to that of nS.

Slight improvement in the 7-day Young's modulus was observed from nS addition and the effect thereon diminishing at 28-days, except for 3 % nS addition which yielded a 7.5 % improvement. SiC was found to be deleterious on the Young's modulus, yielding up to 6 GPa reduction at 7-days for 3 % dosage. At 28-days this impairment is minimized to only a 6 % decrease in Young's modulus. Generally, it can be concluded that nanoparticle addition may be advantageous to obtain improved mechanical properties for 3DCP elements. In this study, the 28-day concrete age mechanical properties were found, on average, to be improved by nanoparticle addition. However, the type and dosage of nanoparticle addition should be critically investigated since the discrepancies between short versus long-term strengths, and compressive versus Young's modulus benefits are significant.

Table 5.5 Compressive strengths and Youngs's moduli of all the HPC mixes for various concrete ages

	Testing Age	HPC ref	HPC nS1	HPC nS2	HPC nS3	HPC SiC1	HPC SiC2	HPC SiC3
Compressive Strength (MPa)	1	7.9	16.5	15.2	13.7	4	7.1	11.1
	7	55.6	60.4	59.8	63	56.1	55.3	57.2
	28	70.6	80.3	76	73.4	79.5	77.9	80
	56	80	72.2	77.2	61.1	83.8	80.2	83.4
Young's Modulus (GPa)	7	26.6	27.6	28.1	27.8	25.6	23.6	20.6
	28	30.7	30.5	30.3	33	29.2	30.6	28.9

5.4.1.4 Flexural and interlayer bond strength

The flexural and interlayer bond strengths of the HPC mixes are given in Table 5.6. Similar trends are observed as in the previous section. At 1-day concrete age, 1 % nS addition more than doubled the flexural strength of the reference mix, yielding a tremendous 3.1 MPa. This effect, however, diluted as the nS dosage increased. In contrast, SiC nanoparticles reduced the 1-day flexural strength of the HPC, with the exception of the 3 % dosage. At a 28-day concrete age, the results do not form a visible trend to capture and comment on the overall impact of nanoparticle addition thereon. However, it must be

mentioned that 2 % nS addition yielded the highest flexural strength of 9.2 MPa at 28-days. Similarly, at 56-days, nS addition does not show any particular advantage or disadvantage. SiC addition generally did improve flexural strength at 56-days concrete age, on average yielding more than 9 MPa for all dosages.

A 19 % S_R in IBS was observed for the reference HPC mix, reducing from 8.4 MPa for mold-cast specimen to 6.8 MPa for the 3D printed specimen in flexure. For 1 % nS addition, the S_R reduced to 13.6 %, i.e. from 8.1 MPa for the mold-cast specimen to 7 MPa for the 3D printed specimen in flexure. Significantly, for the 2 % SiC addition, the S_R reduced to only 6.6 %, i.e. from 7.6 MPa for the mold-cast specimen to 7.1 MPa for the 3D printed specimen in flexure. A clear trend is thus observed in this case where the disparity between intra and interlayer filament strength reduces. The authors theorize this phenomenon may be ascribed to the improved thixotropy, particularly R_{thix}, yielded by the nanoparticle additions. In this case, 1 % nS addition relatively improved R_{thix} by 16 % and 2 % SiC addition relatively improved R_{thix} by 91 %. Due to the improved R_{thix} and short pass times employed (12 s), it is theorized that stronger bonds will form between filament layers, thus constituting the base for pseudo-contact points between which hydration products can form and bind particles together chemically. However, complementary research is required to confirm this theorization.

Table 5.6 Flexural and interlayer bond strengths (IBS) of the HPC mixes for various concrete ages

	Testing Age	HPC ref	HPC nS1	HPC nS2	HPC nS3	HPC SiC1	HPC SiC2	HPC SiC3
Flexural Strength (MPa)	1	1.7	3.1	2.9	2	0.9	1.3	2.2
	7	7.3	7.3	7.3	6.8	6.9	6.9	6
	28	8.4	8.1	9.2	6.8	8	7.6	8.5
	56	8.7	8.4	7.9	7.7	9	9.2	9.3
IBS (MPa)	28	6.8	7	-	-	-	7.1	-

5.4.2 Lightweight 3D printable foamed concrete

5.4.2.1 Static and dynamic yield stresses & thixotropy

Unlike the HPC, the bi-linear static yield shear stress evolution curves could not be generated for the LWFC. Little to no stress recovery is noted for increasing resting time intervals. In fact, negative R_{thix} and A_{thix} values were obtained for the LWFCs, which is impossible for visibly thixotropy materials. In analyzing this unusual result, it was found that LWFC is highly adhesive or sticky and consequently stuck to the vane of the rheometer. Subsequently, a localized shear plane on the perimeter of the vane develops where the material is segregated from one another, resulting in no recovery after resting. Thus,

incorrect material behavior would be captured by the rheometer for consecutive measurements using the same concrete batch. After the first measurement, only rotational inertia of the adhered LWFC would contribute towards the measured rheology. For this reason, only one stress growth test is performed for each LWFC, from which the static and dynamic yield shear stresses are obtained. The results are indicated in Fig. 5.5 and the corresponding rheology parameters are given in Table 5.7.

From the results, it can be observed that the reference LWFC mix possesses significantly low yield stresses, which would result in poor 3DCP constructability. However, both the static and dynamic yield stress were improved for each percentage incorporation of nS. The static and dynamic yield stresses of the reference mix are 78 and 47 Pa, which increased to 224 and 106 Pa with 2 % nS addition and to 386 and 292 Pa for 3 % nS addition. Therefore, 3% nS addition improved $\tau_{S,i}$ by a factor of almost five, and $\tau_{D,i}$ by a factor of more than six. Although a tremendous improvement is noted, these rheology parameters would still be regarded as significantly less favorable for a normal weight concrete for 3D printing application. Nonetheless, a significant improvement in 3DCP constructability is expected, also considering the favorably reduced gravity load in buildability for LWFC. It is further evident in Fig. 5.5 that the difference between the static and dynamic yield stresses increases for each percentage increase in nS addition. This difference, denoting the degree of microstructural breakdown due to shearing, presents an indication of the degree of thixotropy of the material (in the absence of R_{thix}). Thus, it can be concluded that the LWFC's thixotropy also increased for every percentage increase in nS addition.

Since the rheology parameters of the LWFC_nS3 are still considered too low to achieve good buildability, together with the high total water content of the reference mix at 26 % by mass, an adjusted mix with 23 % total water content for improved consistency was prepared and tested, denoted LWFC_nS2_new* in Table 5.3 and Table 5.7 and Fig. 5.5. For this mix, significantly improved static and dynamic yield stresses of 1 170 and 650 Pa were obtained. A notable improvement in buildability is expected from this mix, which proves that a well-designed LWFC and only 2 % nS addition can yield rheology parameters appropriate for 3DCP.

Table 5.7 Static and dynamic yield stresses of the LWFC containing nS

	LWFC ref	LWFC nS2	LWFC nS3	LWFC nS2 new*
$\tau_{S,i}$ (Pa)	78	224	386	1 170
$\tau_{D,i}$ (Pa)	47	106	292	650

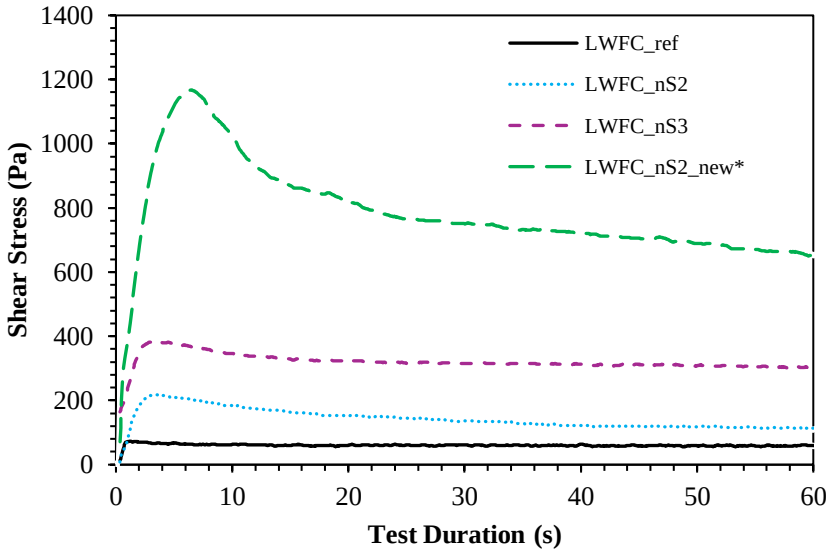

Fig. 5.5 Stress growth test results for the LWFC containing nS

5.4.2.2 Buildability performance and densities

The circular hollow column printed to assess the buildability performance of the LWFC with nanoparticle inclusion is depicted in Fig. 5.6. Only the LWFC_nS2_new* mix is shown here due to the less favorable rheology properties of the other LWFC mixes. Using the rheology properties of LWFC_nS2 and LWFC_nS3, as well as the print parameters depicted earlier, the maximum 3D printable filament layers for these mixes are predicted as three and six layers respectively, based on the buildability model by Kruger et al. (2019b). A total of four and six layers were attained in the buildability test for these respective mixes, but are not shown in this research. The measured wet densities of these two mixes are 1 435 and 1 446 kg/m^3, respectively (see Table 5.3). The LWFC_nS2_new* attained a total of 17 layers before the slow onset of plastic yielding, as seen in Fig. 5.6. Significant radial and axial deformation is observed thereafter, which can then already be regarded as a failed print aesthetically wise. Note that the irregularities shown in Fig. 5.6, visible in the 5^{th} and 8^{th} layers, are due to temporary stoppage of the nozzle that resulted in slight overextrusion at those positions. It should be mentioned that the LWFC_nS2_new* has a higher measured wet density than the other two mixes at 1 648 kg/m^3 (see Table 5.3). This measured wet density increased after extrusion to 1 720 kg/m^3 due to the high pumping pressures. Continued efforts are underway to optimize LFWC to secure foam stability while also achieving reasonable constructability for LWFC of densities in the range 700-1600 kg/m^3. In general, the LWFC_nS2_new* performed average in the buildability test and may be used for 3DCP applications where the pass time is significantly longer. It is clear that the addition of nS to the LWFC tremendously improved the constructability of LWFC for 3DCP application.

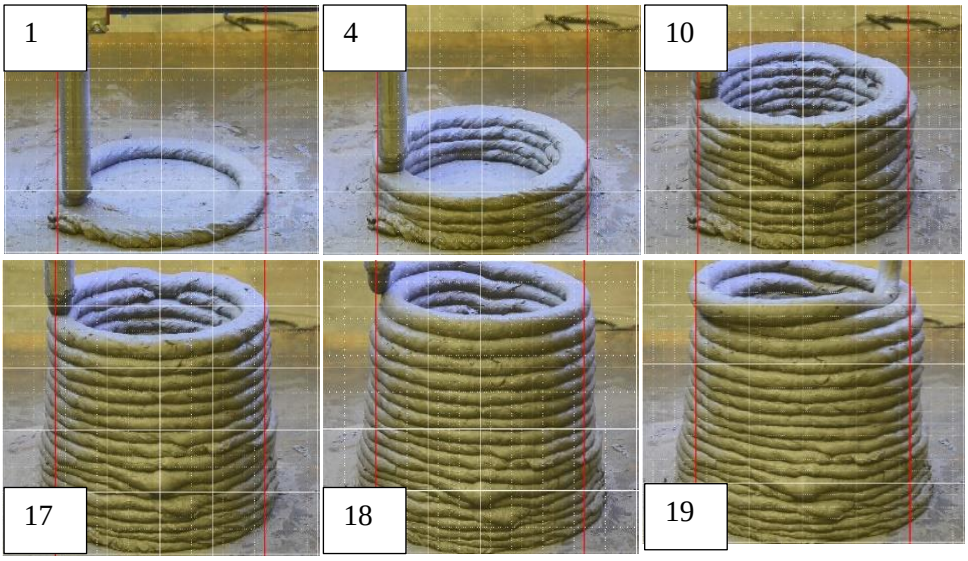

Fig. 5.6 Buildability performance of the LWFC_nS2_new* mix indicating the number of filament layers attained on the top-left corner of each image

5.4.2.3 Mechanical properties

The mechanical properties of the LWFC mixes are given in Table 5.8. Note that only the LWFC_nS2_new* mix is considered, which achieved the best buildability performance of all the LWFCs, and compared to the reference LWFC. The reference mix has a meager compressive strength of 4.9 MPa at 7 days concrete age, which more than doubles to 11.6 MPa at 28-days. In comparison, the mix containing nS has a 7-day compressive strength of 24.5 MPa, which is almost five times that of the reference mix at 7-days. 31.1 MPa compressive strength is reached at 28-days, of which the compressive strength difference now reduced to almost three times that of the reference mix. The reference LWFC has low stiffness, only 7.6 GPa at 7-days curing age. This value reduces to 7.1 GPa at 28-days, for which no explanation can be given. A similar trend is observed for the nS mix, where the Young's modulus remains relatively constant between 7- and 28-day concrete ages, however at almost double that of the reference mix at 13.8 GPa. Again, a similar trend is observed for the flexural strength. At 28-days, the flexural strength of the reference mix reduces by 0.1 MPa to 1.4 MPa flexural strength, compared to 1.5 MPa at 7-days. In contrast, the nS LWFC mix's flexural strength increases from 2.7 MPa at 7-days to 3.8 MPa at 28-days, more than double that of the reference mix. The flexural strength of 3D printed LWFC_nS2_new* samples were also determined in the O-I direction (Kruger & van Zijl, 2021). Unfortunately, due to the average buildability performance and accompanied excessive deformations after deposition of 15 layers, the IBS specimens could not be prepared for interlayer strength determination. Nonetheless, the 3D printed specimens' flexural strength reduced from that of the cast specimens by up to 35 %. Although not an indication of interlayer strength, it does indicate some negative impact imparted by the 3DCP constructability process on the mechanical properties of LWFC. This issue likely pertains to the stability of the foam under pumping pressure. Clearly, 2 % nS

addition significantly improved the mechanical performance of the LWFC, although the higher density of the nS mix compared to the reference mix also contributed to this result.

Table 5.8 Mechanical properties of the LWFC containing nS

	Testing Age	LWFC ref	LWFC nS2_new*	LWFC_nS2_new* 3DP O-I
Compressive Strength (MPa)	7	4.9	24.5	-
	14	10.6	27.6	-
	28	11.6	31.1	-
Young's Modulus (GPa)	7	7.6	13.7	-
	14	7.3	12.3	-
	28	7.1	13.8	-
Flexural Strength (MPa)	14	1.5	2.7	2.3
	28	1.4	3.8	2.4

5.5 Conclusions

This study investigated the use of nanotechnology in 3D printable concrete for improved constructability. This includes rheology and buildability characterisation tests, mechanical tests (Young's modulus and compressive strength) and flexural tests used to evaluate the interlayer bond strength. Based on the tests conducted and the results thereof the following conclusions can be drawn:

Rheology and buildability:

- Inclusion of nanoparticles leads to an increase in the static and dynamic yield stresses allowing for shorter pass times and thus higher constructability. A consistently higher number of deposited layers is achieved for concrete with nanoparticles than those without nanoparticles.
- The specific surface area and the dispersion of nanoparticles influence R_{thix} and A_{thix}. Nanomaterials with large SSA lead to a higher increase in R_{thix} compared to nanomaterials with small SSA.
- High dosages of nanomaterials lead to high static and dynamic yield stresses, rendering the concrete non-pumpable and not suitable for 3D printing.

Mechanical properties:

- For the compressive strength tests and Young's modulus, mixed results are achieved for nanomaterial inclusion. For nS addition, an increase in the early age compressive strength and Young's modulus is obtained, followed by a decrease at higher ages (> 28-days). No clear trend is observed for SiC addition. The data indicates that the compressive strength and Young's modulus is dependent on the concrete age and dosage of the nanomaterials.

Flexural and interlayer bond strengths:

- For the flexural test, mixed results are obtained for the inclusion of nanomaterials. The inclusion of nS led to a high early-age increase in flexural strength diminishing with increasing dosage. No clear trend is found for SiC incorporation.
- Inclusion of nanomaterials leads to an increase in interlayer bond strength. It can be concluded that concrete with higher R_{thix} values and lower A_{thix} values may have higher interlayer bond strength than those with lower R_{thix} values and higher A_{thix} values.

ACKNOWLEDGEMENTS

The financial support by The Concrete Institute (TCI), South Africa, is gratefully acknowledged.

5.6 References

ASTM International. 2002. ASTM C469-02 Standard test method for static modulus of elasticity and poisson's ratio of concrete in compression.

ASTM International. 2019. ASTM C168-19: Standard specification for coal fly ash and raw or calcined natural pozzolan for use in concrete.

Bos, F., Wolfs, R., Ahmed, Z. & Salet, T. 2016. Additive manufacturing of concrete in construction: potentials and challenges of 3D concrete printing. *Virtual and Physical Prototyping*. 11(3):209–225.

Dressler, I., Freund, N. & Lowke, D. 2020. The Effect of accelerator dosage on fresh concrete properties and on interlayer strength in shotcrete 3D printing. *Materials*. 13(2):374.

Dunn, T.P.A., van Zijl, G.P.A.G. & van Rooyen, A.S. 2018. Investigating a reinforced lightweight foamed concrete walling system for low-rise residential buildings in moderate seismic regions. *Journal of Building Engineering*. 20:663–670.

European Standard 196-1. 2016. Cement - determination of strength. *Building Materials 10 - Testing Methods*. 66–71.

García-Taengua, E., Sonebi, M., Hossain, K.M.A., Lachemi, M. & Khatib, J. 2015. Effects of the addition of nanosilica on the rheology, hydration and development of the compressive strength of cement mortars. *Composites Part B: Engineering*. 81:120–129.

Germann Instruments. n.d. *ICAR Rheometer* [Online], Available: http://germann.org/products-by-application/rheology-of-concrete/icar-rheometer. [2020, July 23].

Jones, M. & McCarthy, A. 2005. Preliminary views on the potential of foamed concrete as a structural material. *Magazine of Concrete Research*. 57:21–31.

Kearsley, E. & Mostert, D. 2005. Designing mix composition of foamed concrete with high fly ash contents. in *Use of Foamed Concrete in Construction* (Conference Proceedings). Thomas Telford Publishing. 29–36.

Kruger, J. & van Zijl, G. 2021. A compendious review on lack-of-fusion in digital concrete fabrication. *Additive Manufacturing*. 37:101654.

Kruger, J., Zeranka, S. & van Zijl, G.P.A.G. 2019a. An ab initio approach for thixotropy characterisation of nanoparticle-infused 3D printable concrete. *Construction & Building Materials*. 224:372–386.

Kruger, J., Zeranka, S. & van Zijl, G. 2019b. 3D concrete printing: A lower bound analytical model for buildability performance quantification. *Automation in Construction*. 106:102904.

Kruger, J., Cho, S., Zeranka, S., Barnardo Viljoen, C. & van Zijl, G. 2020. 3D concrete printer parameter optimisation for high rate digital construction avoiding plastic collapse. *Composites Part B Engineering*. 183:107660.

Le, T.T., Austin, S.A., Lim, S., Buswell, R.A., Law, R., Gibb, A.G.F. & Thorpe, T. 2012. Hardened properties of high-performance printing concrete. *Cement and Concrete Research*. 42(3):558–566.

Mahawish, A. 2017. Effect of adding silicon carbide and titanium carbide nanoparticles on the performance of the cement pastes. *Journal of Civil & Environmental Engineering*. 7:4.

Nanostructured & Amorphous Materials. n.d. *About Us*. [Online], Available: www.nanoamor.com/about_us [2020, July 22].

Panneerselvam, S. & Choi, S. 2014. Nanoinformatics: emerging databases and available tools. *International journal of molecular sciences*. 15(5):7158–7182.

Paul, S.C., van Rooyen, A.S., van Zijl, G.P.A.G. & Petrik, L.F. 2018. Properties of cement-based composites using nanoparticles: A comprehensive review. *Construction and Building Materials*. 189:1019–1034.

Roussel, N. 2006. A thixotropy model for fresh fluid concretes: Theory, validation and applications. *Cement and Concrete Research*. 36(10):1797–1806.

Said, A., Ayad, A. & Zeidan, M. 2018. Beneficial use of nano-silica in concrete : A review. *Trends in Civil Engineering and Material Science*. 1–3.

Senff, L., Labrincha, J.A., Ferreira, V.M., Hotza, D. & Repette, W.L. 2009. Effect of nano-silica on rheology and fresh properties of cement pastes and mortars. *Construction and Building Materials*. 23(7):2487–2491.

Suiker, A.S.J., Wolfs, R.J.M., Lucas, S.M. & Salet, T.A.M. 2020. Elastic buckling and plastic collapse during 3D concrete printing. *Cement and Concrete Research*. 135:106016.

de Villiers, J.P., van Zijl, G.P.A.G. & van Rooyen, A.S. 2017. Bond of deformed steel reinforcement in lightweight foamed concrete. *Structural Concrete*. 18(3):496–506.

Wolfs, R.J.M. & Suiker, A.S.J. 2019. Structural failure during extrusion-based 3D printing processes. *The International Journal of Advanced Manufacturing Technology*. 104(1):565–584.

Chapter 6

Research Summary and Conclusions

6.1 Research Summary and Contributions

Sustainability and energy efficiency of building materials demand continued research and development efforts. LWFC for both structural and non-structural applications as a highly energy-efficient building material with lightened weight is one of the outcomes from many efforts. There have been various attempts to engineer LWFC to have augmented features, such as ultra-lightweight foam concrete (< 300 kg/m^3) for greatly improved thermal insulative property (Wei *et al.*, 2013), improved mechanical strength (Krämer *et al.*, 2016), low cement content LWFC (Kearsley & Mostert, 2005) or foamed geopolymer concrete for sustainability (Dhasindrakrishna *et al.*, 2020). In this research, a further effort has been made to engineer LWFC to be 3D concrete printable, with the following activities in each chapter.

Chapter 2 describes the development of the 3D printer facility at Stellenbosch University and the systematic process of mastering the 3D concrete printing technique. 3D printable normal weight cementitious materials development is also presented, introducing thixotropy as an essential rheological property. The rheological characterisation was conducted with a rotary concrete rheometer, clearly demonstrating the altered shearing resistances ascribed to de-flocculation and re-flocculation phenomena by performing stress growth tests at various resting times. A reference 3D printable concrete material was developed, and from various mechanical characterisation tests on the hardened concrete material, it was classified as a high-performance concrete with 70.6 MPa compressive strength, 8.4 MPa flexural strength, and 30.8 GPa elastic modulus at 28 days. Furthermore, printing parameters were calibrated according to pump specifications and the fresh material's behaviour. As a final result, an about 800 mm high circular hollow column was successfully constructed by 3D concrete printing in a continuous digital construction process at a relatively high rate, within 30 minutes, without plastic collapse. This 3DPC facility and basic knowledge of 3D printable cementitious materials were essential for the research executed in this dissertation.

Chapter 3 presents an interdisciplinary foam stability background study and foam stability assessment for 3DP-LWFC under static and 80 kPa pressurised conditions, as well as 3D printing. Initially, the effect of the increased yield stress of the base mortar mixes for foam stability was investigated. A stiffer base mix was found to cause more foam breakdown, determined by recording the incorporated foam volumes to achieve the target densities for base mixes with different yield stresses. Thereafter, rheology modified 3DP-LWFC samples with a wide range in density were produced for foam stability assessment

under static and dynamic environments. Various wet-density correlation empirical models, as well as theoretical porosity models, were evaluated against the obtained results. Also, the void structure of 3DP-LWFC was investigated via X-ray computed tomography scanned images.

Chapter 4 performs comprehensive rheological characterisation of 3DP-LWFC over a wide density range, namely 700 – 1400 kg/m^3. Two types of test methods are presented, namely a controlled shear rate test for static and dynamic yield stress identification, and a flow curve test for plastic viscosity identification. Furthermore, a set of controlled shear rate tests enabled the calculation of thixotropic parameters R_{thix} and A_{thix}. Based on the rheological characterisation, a circular hollow column was printed until collapse as a buildability model validation of the model proposed by Kruger et al. (2019). This chapter also proposes a potential practical application of 3DP-LWFC by producing a modular buoyant façade element.

Chapter 5 assesses the effect of nanoparticle inclusion in cementitious material for 3D concrete printing application. The test procedures and results of mechanical and rheological assessments for both normal-weight 3D printable concrete and 3DP-LWFC were investigated. As a validation, buildability testing was conducted as per Kruger et al. (2019). It was clearly found that nanoparticle inclusion improved mechanical and rheological characteristics for both concrete.

In summary, this research has successfully developed a 3DP-LWFC mix design with various foam volume fractions without compromising foam stability through various material characterisation processes.

6.2 Conclusions

Detailed conclusions are already presented in Chapters 2 to 5. Here, conclusions are drawn on the achievement of the set aims and objectives of this dissertation.

1. *3D printable LWFC was developed in the density range of 700 – 1400 kg/m^3*
    a. Locally sourced material selection for appropriate LWFC mix design was completed to significantly enhance the yield stress and thixotropic behaviour for shape retention and buildability.
    b. A stable foam was produced from a natural protein-based foam agent, and the wide density range of LWFC was produced by varying the incorporated foam volume.
    c. A reasonable buildability was shown by printing several objects up to about 150-mm in height in continuous, relatively high-rate 3D printing at 60 mm/s nozzle speed.
    d. Nano silicon dioxide powder incorporation enhanced fresh and hardened state properties, and the compatibility was proven by characterising foam stability, rheology and mechanical test results.

e. Calcium sulfoaluminate (CSA) cement replacing 10% of the Portland cement mass successfully increased the thixotropic behaviour and foam stability by shortened setting time, supported by stability and rheology test data.

2. *Foam stability in the wide density range was achieved*
   - *a.* Under static conditions, i.e. only atmospheric pressure in the laboratory environment, all three tested densities in the range 700 – 1400 kg/m^3 showed density consistency, indicating foam stability in fresh and hardened states.
   - *b.* Under the constant pressure of 80 kPa for 15 minutes to replicate confining pipe pressure during material transport in a concrete pumping process, all three samples remained stable in the fresh state.
   - *c.* Under dynamic conditions – actual pumping in the 3D printer facility of Stellenbosch University – foam instability occurred in the higher density, 1400 kg/m^3, ascribed to low fluidity and low foam volume fraction. However, foam stability in lower densities, 700 and 1000 kg/m^3, was clearly shown and ascribed to higher fluidity and a cushioning effect of high foam volume fractions.
3. *Appropriate rheology for buildability and stability was proven*
   - a. A new base mix small slump table flow diameter range, 185 – 195mm, was proposed for better 3D printability, i.e. pumpability, buildability and shape retention, compared to the conventional range of 220 – 250 mm for stable LWFC production. Foam stability based on the new range was thoroughly studied and proven.
   - *b.* Nanoparticle inclusion increased yield stress and thixotropic properties significantly but caused concern about foam destabilisation due to greatly reduced fluidity through the high specific surface area. However, setting time reduction by CSA cement inclusion and water content adjustment achieved stable foamed concrete for the wide density range.
   - *c.* Rheo-mechanical properties of 3DP-LWFC were validated by 3D printing against buildability model prediction.
   - *d.* Rheologically modified 3DP-LWFC was shown to have elevated static and dynamic yield stresses and thixotropic rates R_{thix} and A_{thix}, which are crucial parameters for designing a 3D concrete printing object and material.
4. *Mechanical and microstructural characterisation*
   - a. The enhanced mechanical strength of 3DP-LWFC with a density of 1400 kg/m^3 by nanoparticle inclusion was confirmed by mechanical characterisation results (compressive strength – 31.1 MPa, flexural strength – 3.8 MPa and elastic modulus – 13.8 GPa at 28 days) compared to conventional LWFC (compressive strength – 11.6 MPa, flexural strength – 1.4 MPa and elastic modulus – 7.1 GPa at 28 days).

b. Void structures of the wide density range samples were analysed via X-ray computed tomography scanning images. Post-processed defect analysis results showed that porosity, the dominant pore size range and pore size distribution are relatively unaffected by 3D printing of higher density LWFC (1000 and 1400 kg/m^3).

c. Post-pumped samples showed decreased sphericity due to the confinement pressures except for the low density (700 kg/m^3) sample, which is an indication of high-quality foam. Also, higher smaller pore size contents were found in all post-pumped samples due to the same reason.

6.3 Recommendations for Future Research

This innovative 3D printable LWFC mix design development is at an early stage. Since this research has proved the potential of LWFC for additive manufacturing application, the following future researches are suggested:

- Though a 3DP-LWFC mix design development without compromising foam stability was successful, the buildability is limited to roughly 300 mm high object for continuous printing while sound shape retention is provided. Thus, further buildability improvement by rheological modification is inevitable for a versatile and practical implementation such as load-bearing walls and columns.
- As part of sustainable cementitious material development, higher cement replacement by SCMs may be explored within the context of 3DP-LWFC.
- For better thermal insulative property, lower density LWFC can be investigated for 3DCP application. Likewise, higher density 3DP-LWFC can also be investigated for enhanced mechanical characteristics. Along the line, high fibre content can be considered for improved ductility.
- Thermal insulative behaviour is a prominent property of LWFC. Thus, the thermal behaviour of 3D printed foamed concrete structure should be systematically investigated. Furthermore, the behaviour of 3DP-LWFC under the elevated temperature environment, i.e. fire performance, is required for safe building application.
- More case and feasibility studies for potential practical application should be conducted in aspects of economic and sustainability impacts.

6.4 References

Dhasindrakrishna, K., Pasupathy, K., Ramakrishnan, S. & Sanjayan, J. 2020. Effect of yield stress development on the foam-stability of aerated geopolymer concrete. *Cement and Concrete Research*. 138:106233.

Kearsley, E. & Mostert, D. 2005. Designing mix composition of foamed concrete with high fly ash contents. in *Use of Foamed Concrete in Construction* (Conference Proceedings). Thomas Telford Publishing. 29–36.

Krämer, C., Dang, Z. & Trettin, R. 2016. UHPC foam concretes on the basis of three-phase-foams. *Proceedings of Hipermat 2016 - 4th International Symposium on Ultra-High Performance Concrete and High Performance Construction Materials Kassel*. Mar 2016:1–7.

Kruger, J., Zeranka, S. & van Zijl, G. 2019a. 3D concrete printing: A lower bound analytical model for buildability performance quantification. *Automation in Construction*. 106:102904.

Kruger, J., Zeranka, S. & van Zijl, G.P.A.G. 2019b. An ab initio approach for thixotropy characterisation of nanoparticle-infused 3D printable concrete. *Construction & Building Materials*. 224:372–386.

Wei, S., Yiqiang, C., Yunsheng, Z. & Jones, M.R. 2013. Characterization and simulation of microstructure and thermal properties of foamed concrete. *Construction and Building Materials*. 47:1278–1291.

Addendum A – Article Declarations

Declaration by the candidate:

With regard to Chapter 2, the nature and scope of my contribution were as follows:

Nature of contribution	Extent of contribution (%)
Conducting experimental work, formal analysis, validation, investigation, data curation, writing – original draft	85

The following co-authors have contributed to Chapter 2:

Name	E-mail address	Nature of contribution	Extent of contribution (%)
Dr Jacques Kruger	pjkruger@sun.ac.za	Experimental work, data curation, investigation, writing – review & editing	5
Dr Stephan Zeranka	szeranka88@gmail.com	Supervision, writing – review & editing	5
Prof Gideon van Zijl	gvanzijl@sun.ac.za	Supervision, writing – review & editing, project administration, funding acquisition	5

Signature of candidate:

Date: 23/02/2021

Declaration by co-authors:

The undersigned hereby confirm that

1. the declaration above accurately reflects the nature and extent of the contributions of the candidate and the co-authors to Chapter 2,
2. no other authors contributed to Chapter 2 besides those specified above, and
3. potential conflicts of interest have been revealed to all interested parties and that the necessary arrangements have been made to use the material in Chapter 2 of this dissertation.

Signature	Institutional affiliation	Date
	Stellenbosch University	23/02/2021
	Stellenbosch University	25/02/2021
	Stellenbosch University	25/02/2021

Declaration by the candidate:

With regard to Chapter 3, the nature and scope of my contribution were as follows:

Nature of contribution	Extent of contribution (%)
Conceptualisation, methodology, conducting experimental work, formal analysis, validation, investigation, data curation, writing – original draft	85

The following co-authors have contributed to Chapter 3:

Name	E-mail address	Nature of contribution	Extent of contribution (%)
Dr Algurnon van Rooyen	asvr@sun.ac.za	Supervision, writing – review & editing	5
Prof Elsabe Kearsley	elsabe.kearsley@up.ac.za	Data curation, writing – review & editing	5
Prof Gideon van Zijl	gvanzijl@sun.ac.za	Supervision, writing – review & editing, project administration, funding acquisition	5

Signature of candidate:

Date: 23/02/2021

Declaration by co-authors:

The undersigned hereby confirm that

1. the declaration above accurately reflects the nature and extent of the contributions of the candidate and the co-authors to Chapter 3,
2. no other authors contributed to Chapter 3 besides those specified above, and
3. potential conflicts of interest have been revealed to all interested parties and that the necessary arrangements have been made to use the material in Chapter 3 of this dissertation.

Signature	Institutional affiliation	Date
	Stellenbosch University	25/02/2021
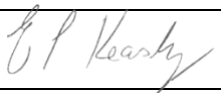	Pretoria University	24/02/2021
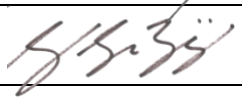	Stellenbosch University	25/02/2021

Declaration by the candidate:

With regard to Chapter 4, the nature and scope of my contribution were as follows:

Nature of contribution	Extent of contribution (%)
Conceptualisation, methodology, conducting experimental work, formal analysis, validation, investigation, data curation, writing – original draft	85

The following co-authors have contributed to Chapter 4:

Name	E-mail address	Nature of contribution	Extent of contribution (%)
Dr Jacques Kruger	pjkruger@sun.ac.za	Conceptualisation, writing – review & editing	5
Dr Algurnon van Rooyen	asvr@sun.ac.za	Supervision, writing – review & editing	5
Prof Gideon van Zijl	gvanzijl@sun.ac.za	Supervision, writing – review & editing, project administration, funding acquisition	5

Signature of candidate:

Date: 23/02/2021

Declaration by co-authors:

The undersigned hereby confirm that

1. the declaration above accurately reflects the nature and extent of the contributions of the candidate and the co-authors to Chapter 4,
2. no other authors contributed to Chapter 4 besides those specified above, and
3. potential conflicts of interest have been revealed to all interested parties and that the necessary arrangements have been made to use the material in Chapter 4 of this dissertation.

Signature	Institutional affiliation	Date
	Stellenbosch University	23/02/2021
	Stellenbosch University	25/02/2021
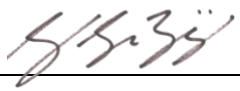	Stellenbosch University	25/02/2021

Declaration by the candidate:

With regard to Chapter 5, the nature and scope of my contribution were as follows:

Nature of contribution	Extent of contribution (%)
Conducting experimental work, formal analysis, data curation, writing – original draft	40

The following co-authors have contributed to Chapter 5:

Name	E-mail address	Nature of contribution	Extent of contribution (%)
Dr Jacques Kruger	pjkruger@sun.ac.za	Writing – original draft, Data collection, investigation, formal analysis	45
Mr Marchant van den Heever	mvdheever@sun.ac.za	Conducting experimental work, data curation, writing – review & editing	7
Mr Frederick Bester	fabester@sun.ac.za	Writing – review & editing	2.5
Dr Algurnon van Rooyen	asvr@sun.ac.za	Writing – review & editing	2.5
Prof Gideon van Zijl	gvanzijl@sun.ac.za	Supervision, writing – review & editing, project administration, funding acquisition	3

Signature of candidate:

Date: 23/02/2021

Declaration by co-authors:

The undersigned hereby confirm that

1. the declaration above accurately reflects the nature and extent of the contributions of the candidate and the co-authors to Chapter 5,
2. no other authors contributed to Chapter 5 besides those specified above, and
3. potential conflicts of interest have been revealed to all interested parties and that the necessary arrangements have been made to use the material in Chapter 5 of this dissertation.

Signature	Institutional affiliation	Date
	Stellenbosch University	23/02/2021
	Stellenbosch University	24/02/2021

	Stellenbosch University	23/02/2021
	Stellenbosch University	25/02/2021
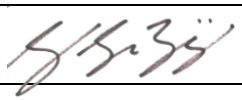	Stellenbosch University	25/02/2021

Addendum B – Copyright Permission

Elsevier:

Table of Author's Rights

	Preprint version (with a few exceptions- see below *)	Accepted Author Manuscript	Published Journal Articles
Use for classroom teaching by author or author's institution and presentation at a meeting or conference and distributing copies to attendees	Yes	Yes	Yes
Use for internal training by author's company	Yes	Yes	Yes
Distribution to colleagues for their research use	Yes	Yes	Yes
Use in a subsequent compilation of the author's works	Yes	Yes	Yes
Inclusion in a thesis or dissertation	Yes	Yes	Yes
Reuse of portions or extracts from the article in other works	Yes	Yes with full acknowledgement of final article	Yes with full acknowledgement of final article
Preparation of derivative works (other than for commercial purposes)	Yes	Yes with full acknowledgement of final article	Yes with full acknowledgement of final article
Preprint servers	Yes	Yes with the specific written permission of Elsevier	No
Voluntary posting on open web sites operated by author or author's institution for scholarly purposes	Yes (author may later add an appropriate bibliographic citation, indicating subsequent publication by Elsevier and journal title)	Yes, with appropriate bibliographic citation and a link to the article once published	Only with the specific written permission of Elsevier
Mandated deposit or deposit in or posting to subject-oriented or centralized repositories	Yes under specific agreement between Elsevier and the repository	Yes under specific agreement between Elsevier and the repository**	Yes under specific agreement between Elsevier and the repository
Use or posting for commercial gain or to substitute for services provided directly by journal	Only with the specific written permission of Elsevier	Only with the specific written permission of Elsevier	Only with the specific written permission of Elsevier

** Voluntary posting of Accepted Author Manuscripts in the arXiv subject repository is permitted.